RTI

RESEARCH TRIANGLE INSTITUTE

ADA043251

Final Report

TRACE GAS FIELD INSTRUMENTATION VAN AND
EXPLOSIVE DETECTION RESEARCH

March 1977

Contract DAAG53-76-C-0028

P. A. Lawless

for

Mine Detection Division
U. S. Army Mobility Research
and Development Command
Fort Belvoir
Virginia 22060

DDC

RECEIVED

AUG 16 1977

A

304 400

RESEARCH TRIANGLE PARK, NORTH CAROLINA 27709

TABLE OF CONTENTS

i

TABLE OF CONTENTS (Continued)

ii

LIST OF FIGURES

LIST OF FIGURES (Continued)

iv

LIST OF FIGURES (Continued)

LIST OF TABLES

1.0 INTRODUCTION

The Plasma Chromatograph^{TM} (PC) is an analytical instrument that is nearly ideally suited for explosives vapor detection. It is sensitive, rugged, has a moderate selectivity, operates at atmospheric pressure, and, in the negative mode, responds to relatively few substances except the nitrated compounds used as the basis for explosives. An earlier research contract on a comparative evaluation of trace gas technology (U. S. Army MERDC Contract No. DAAK02-73-C-0128) identified the Plasma Chromatograph as a very promising detector for TNT and DNT, which might be characteristically emitted from concealed explosives.

The scope of the present contract (USAMERADCOM No. DAAG53-76-C-0028) was to quantify the sensitivity of the Plasma Chromatograph to explosive materials and to investigate and put into practice ways of improving its sensitivity and selectivity. A thorough understanding of the processes of production of identifiable ions and the way in which the instrument responds to them is necessary before it can be developed into a practical explosives detector. The sensitivity of the Plasma Chromatograph was analyzed and quantified in terms of the ionization efficiency for a given material and the detectability of an ion once produced. Ionization efficiency depends upon the type and relative speeds of reactions occurring in the vicinity of the radioactive source region of the Plasma Chromatograph, whereas detectability is a function of transmission losses and instrument noise.

This report is broken into six major sections. The first describes the general physical and electrical operation of the Plasma Chromatograph

1

to provide the background on which subsequent sections are based. The next section describes the physical and operating characteristics of a dilution flask used to measure ionization efficiencies, and the following section reports the measurements actually made. The next section is devoted to signal processing techniques, some of which are conceptual and some of which were put into practice. Following this a description is given of a vapor calibration source built during the course of the project in order to provide a steady-state input of test vapor at very low concentrations. A summary and recommendation section concludes this report.

The primary projects of the research conducted under this contract were the measured sensitivity of the basic Plasma Chromatograph and the projected sensitivities of advanced forms of signal processing for the explosive materials TNT and DNT. These results are presented in the concluding section of this report.

2.0 THE BETA/VII PLASMA CHROMATOGRAPH

The plasma chromatograph (PC) is an ion mobility spectrometer. Analysis is achieved by ionizing sample molecules and then gating a narrow pulse of ions into a drift region, where the individual species undergo collisions with neutral gas molecules in the presence of an electric field and separate because of the different drift velocities which result. The signal current due to collected ions at the end of the drift region can be displayed versus drift time to provide a mobility spectrum for the ions formed from the sample.

The operation of the plasma chromatograph can be described in five basic sections: the ion reaction region, the drift region, the detection electronics, the control electronics, and the temperature control section. Successful operation of the instrument requires a supply of clean, dry gas, which is provided by standard gas handling equipment integrally incorporated in to the instrument. A description of each of the five basic sections and the principles of operation follow.

2.1 The Ion Reaction Region

The ion reaction region is one part of a tubular chamber called the SIFAD^{TM}, an acronym standing for "Separate Ion Formation and Drift." The other part of the SIFAD is the drift region, which will be discussed in Section 2.2. The ion reaction region is a small cylindrical volume into which the sample vapor is introduced and where it is ionized.

Physically, the ion reaction region is part of the entire drift tube assembly, which consists of 14 cylindrical rings separated by tiny sapphire spheres and held in compression by three long rods

3

under tension. The rings form the walls of the ion and drift regions and are maintained at different electrical potentials by an internal and an external voltage divider, establishing a voltage grading (drift field) across the entire assembly. Figure 2.1 shows the construction of the ion reaction region. The rings are also separated by Teflon spacers to seal the drift tube volume and force all the gas to flow down the length of the column. The rings actually overlap slightly without touching in order to make the electric field more uniform and prevent the ions from depositing on insulating surfaces where they would distort the field locally.

The sample vapors are introduced into the ion reaction region through a hole in a plate (the repeller) at one end of the ring stack. A multi-holed diffuser spreads the vapor stream into the reaction volume. The repeller and diffuser are maintained at the highest potential in the instrument (in absolute value) and serve to establish a uniform field and to neutralize ions which are created with the undesired polarity.

The inner surface of the first ring next to the repeller has a radioactive foil, Ni^{63} in platinum or gold, lining the inner surface. The strength of the source is 11.3 millicuries. Ni^{63} is a β-emitter, producing electrons with energies up to 60 keV. The diameter of the ring is chosen so that the energetic electrons lose most of their energy by ionizing collisions before crossing the ring. In this design the ring inner diameter is 1.41 cm.

4
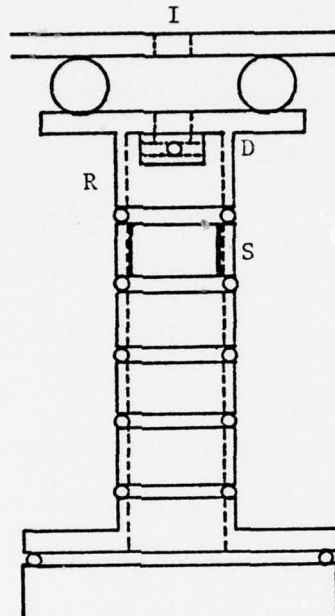
Figure 2.1. Reaction region of the PC. The inlet is designated I; the inlet tube seats in the diffuser D; the repeller ring is designated R; and the radioactive source is at S. (Actual size)

The ions of the proper polarity are separated from those of the opposite sign by the electric field. This separation reduces ion losses due to recombination. The ions, driven primarily by the electric field, and neutral gas molecules flowing in the gas stream travel the length of the reaction region, which is 6.0 cm, before the mobility analysis begins.

Using nitrogen gas as a carrier, the predominant positive ions formed are $H^+(H_2O)_n$ and the predominant negative ions formed are free electrons (References 1 and 2). These are the reactant ions that are the primary ionizers for the sample molecules. Normally, the sample density is so low that direct ionization by the 60 keV electrons from the foil is quite low.

The reactant ion currents from the reaction region are about $+5.9 \cdot 10^{-10}$A at an applied potential of +3000 V and 200°C and $-7.5 \cdot 10^{-10}$A at an applied potential of -3000 V and 200°C for nitrogen carrier gas. The free electron current is higher than the positive ion current presumably because the electron mobility is so high that fewer are lost through recombination and diffusion effects.

There are two interesting considerations to take into account in the reaction region. The first is that, despite the action of the diffuser, the flow at the outlet of the region is probably laminar. This is important because laminar flow gives a zero gas velocity at the walls of the tube and no turbulent mixing. The second point is that sample ions of the undesired polarity, which may greatly outnumber those of the desired polarity, travel to the repeller, which is at a lower potential for them, where they are neutralized. Being neutal, they may then be swept through

6

the reaction region again, unless reactions at the repeller surface either capture or ionize them. In this way, all of the molecules that are introduced actually flow out of the reaction region either as neutrals or as ions of the desired polarity.

2.2. Drift Region

The last ring of the reaction region makes a transition to the larger rings of the drift region. The drift region is composed of 8 rings, each 1 cm. long and with an inner diameter of 4.25 cm. The purpose of the larger diameter is to reduce the losses of ions by transverse diffusion to the walls during the mobility analysis. With the exception of the larger diameter, the construction of the drift region is the same as the reaction region.

The first ring of the drift region is split into two shorter rings with a slight gap between them. In this gap is a grid composed of parallel, tautly stretched fine tungsten wires, a Bradbury-Nielsen shutter (Reference 3). The wires are $5 \cdot 10^{-3}$ cm in diameter and are spaced $6.35 \cdot 10^{-2}$ cm apart, giving an optical transmission of 92.6 percent. Alternate wires are connected electrically, and a potential is applied between the two sets of wires. This produces a transverse electric field which is strong enough to prevent all but a small percentage of ions from penetrating the grid. If the transverse field is removed for a short period of time, then a pulse of ions is passed through into the drift tube. The potentials applied to the wires are above and below the potential applied to the ring, so that the average potential is just that of the ring and the uniformity of the drift field is maintained.

7

A counter flow of nitrogen gas, the "drift" gas, sweeps all the neutralized molecules out of the drift region and into the exhaust port together with the neutral molecules which have passed through the reaction region.

The whole drift region is 8 cm long, ending at the ion collector plate. However, a second grid is located at a distance 6 cm from the first grid. Its mechanical construction and electrical operation are identical to those of the first grid, but it serves another function. If it is held open at all times, the ion pulses are passed to the ion collector and can be processed by a fast electrometer. If, on the other hand, the second grid remains closed most of the time, opening only at a time delayed from the first grid opening, then only ions that have arrived at the second grid as it opens will pass on through. This is known as the two-grid mode of operation and has the advantage that a slower responding electrometer with a lower noise figure may be used.

There is a third grid, called the aperture grid, located directly in front of the ion collector plate. It is electro-etched in tungsten sheet and has an optical transmission of 80 percent over its diameter of 3.18 cm. It is spaced approximately $2.5 \cdot 10^{-2}$ cm in front of the ion collector. The purpose of the aperture grid is twofold: First, it serves as an electrostatic screen to shield the sensitive electrometer from the voltage transient on the first and second grids, which would be otherwise capacitively coupled to the collector, and second, it shields the collector from the displacement current of the ions as they move across the space between the second grid and the collector.

8

In this way, the output of the electrometer is determined only by the shape of the ion peak as it passes between the aperture grid and the collector plate.

The collector plate itself is a stainless steel plate 4.8 cm in diameter. The plate is isolated by six sapphire balls and is shielded by a grounded ring. The measured capacitance of the collector to the ground is 60 picofarads. Most of this capacitance can be attributed, by calculation, to the aperture grid.

A diagram of the entire SIFAD is shown in Figure 2.2, drawn to actual size.

The overall transmission factor of the three grids is taken to be the product of their individual optical transmissivities, a value of 67.7 percent. This is the maximum transmissivity possible. Since the ions in the PC follow electric field lines rather than the optical line of sight, it should be expected that the actual transmission is less than this and a calculation of the ionic transmissivity is presented, in Appendix 4 giving a value of 43.9 percent. Although the ionic transmissivity is a lower limit and represents a better estimate than the optical figure, the optical figure was used extensively throughout this work until the ionic transmissivity was calculated.

The ion leakage of the grids when closed was determined by pulsing the first grid as usual and measuring the amplitude of the collector current, first with the second grid open and then with the second grid closed. Where nitrogen was the carrier gas and the reactant ions were free electrons, the leakage of the second grid was 2.5 percent. Other reactant ions, both positive and negative, showed no measurable leakage.
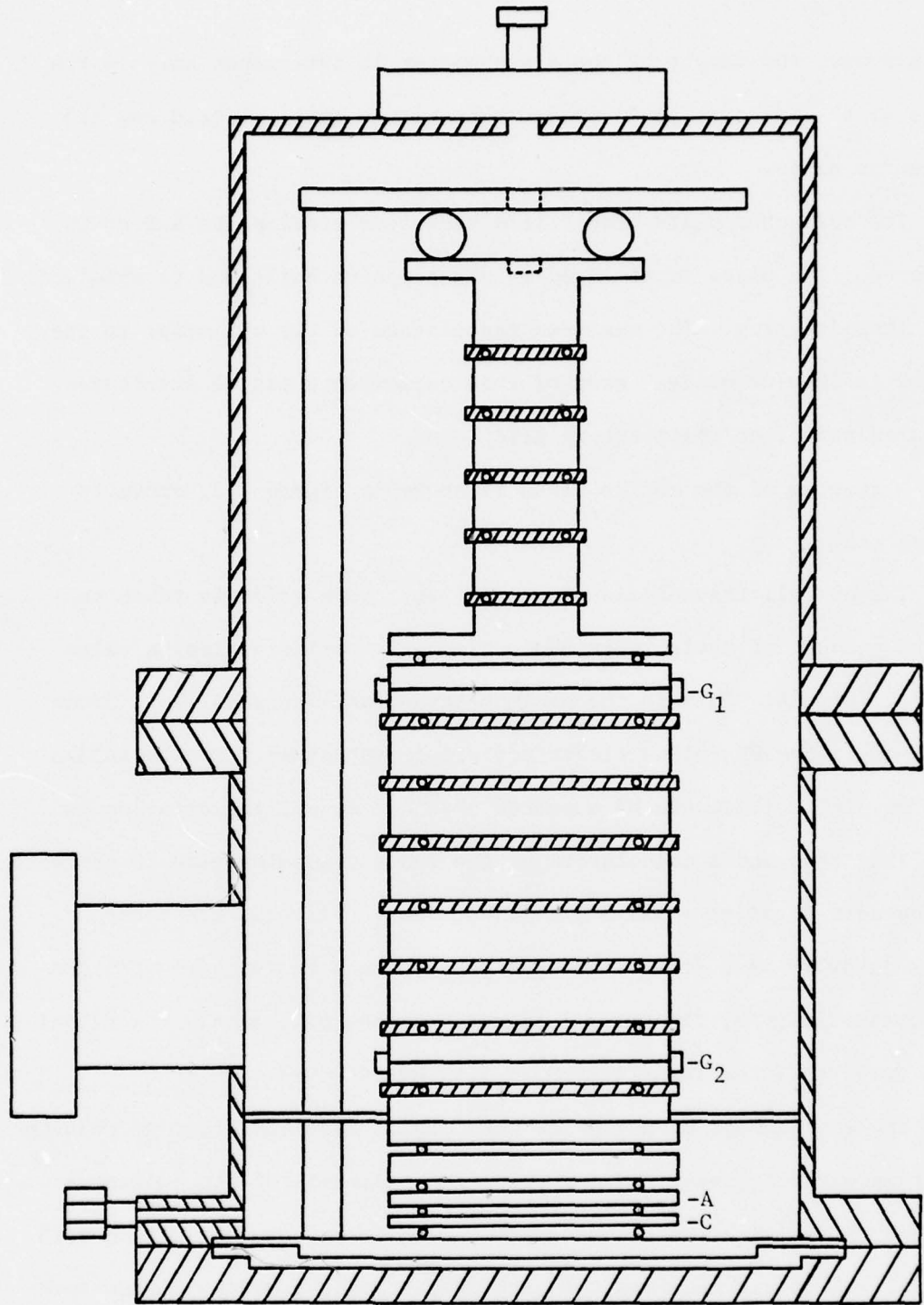
Figure 2.2. SIFAD Tube. Location of the grids, G_1, G_2, and A are shown, along with the collector, C. (Actual size).

10

This difference is attributable to the higher mobility of the electrons compared to other ions. This implies that operation in the two-grid mode with nitrogen carrier will produce an electrometer signal that is the sum of the ion signal of interest and a substantial electron leakage current, which will have to be taken into account in some cases.

The aperture grid is unsupported over its active area, and it flexes like a drumhead. The motion of the grid induces spurious currents in the collector plate. These are especially apparent in the one-grid mode using an oscilloscope monitor. External vibrations of the instrument housing, loud sounds, and even the induced vibrations from large flow rates of drift gas show up readily. This vibration presents a serious impediment to sensitive detection of vapors in a mechanically severe environment, and it was suspected that even thermal agitation of the grid could present a significant noise to the electrometer. A calculation of the amplitude of motion was performed along the following lines.

Drumhead solutions of the wave equation involve Bessel functions. The fundamental mode of vibration, with the whole diaphragm moving in the same phase, has a frequency given by:

$$f = \frac{2.405 \ c}{2\pi \ R} \ , \tag{2.1}$$

where f is the frequency, c is the velocity of sound in the diaphragm, and R is the radius. By shock-exciting the diaphragm many times, a lowest observed frequency was found at about 3600 Hz. This was assumed to be the fundamental frequency.

11

The velocity of sound in the drumhead is given by:

$$c^2 = \frac{T}{\mu} \, , \qquad\qquad (2.2)$$

where T is the tension in the diaphragm and μ is the mass per unit area. The value of T is unknown, and, moreover, may not be isotropic, but it was assumed so for the purpose of the calculation. The mass per unit area was calculated by dividing the volume times the density of the grid by its area, with the density taken as 20 percent of pure tungsten because of the etched holes in the grid. The thickness of the grid was assumed to be $2.54 \cdot 10^{-3}$ cm, after a conversation with the manufacturer. The value calculated for μ was $9.8 \cdot 10^{-2}$ kg/sec^2.

According to the equipartition-of-energy theorem (Ref. 23), the average potential energy of an oscillator mode is $1/2\ k_B\ T_{abs}$, where k_B is Boltzmann's constant and T_{abs} is the absolute temperature of the oscillator; this energy is $3.26 \cdot 10^{-21}$ joule at 200°C.

The potential energy stored in a diaphragm in its fundamental mode is given by:

$$E = \int_o^A \int_o^R Ta J_o(r) dr da \, , \qquad\qquad (2.3)$$

where a is the displacement of the diaphragm at its center, A is the maximum displacement of the diaphragm (at $r = 0$), and R is the radius. $J_o(r)$ is the Bessel function, and the variable r is scaled so that the first zero of $J_o(r)$ falls at radius R.

$$E = T \frac{A^2}{2} \int_o^R J_o(r) dr = .735\ TA^2 \, . \qquad\qquad (2.4)$$

12

This gives, for the root mean square amplitude,

$$A = 1.42 \cdot 10^{-12} m .$$

This amplitude is small, a fraction of an atomic radius; but it is significant as will be seen in Section 2.3. From its derivation, the temperature dependence of A is $(T_{abs})^{1/2}$. Further discussion of the thermal agitation of the aperture grid will be deferred to the following section.

The ions are admitted to the drift region as a narrow, rectangular (in time) pulse. As they drift under the influence of the electric field, the original pulse separates into individual pulses composed of the separate ionic species. In general, the separation between peaks, in time, grows in proportion to the drift time; the resolution of peaks can be increased by reducing the strength of the electric field. However, the original rectangular pulse spreads under the influence of diffusion and space charge effects while it is drifting. The rectangular shape becomes Gaussian, for narrow gate widths, and the spreading effect grows approximately in proportion to the square root of the drift time. Lateral diffusion, transverse to the drift direction, causes ions in the pulse to be neutralized on the walls of the drift tube or to exceed the active collecting area of the aperture grid. The lateral diffusion losses also increase with the drift time.

2.3 Detection Electronics

The detection electronics consist of a preamplifier and two post amplifiers, which condition the ion signal for output to a recorder or signal averager. A block diagram of the detection electronics is shown in Figure 2.3.

13
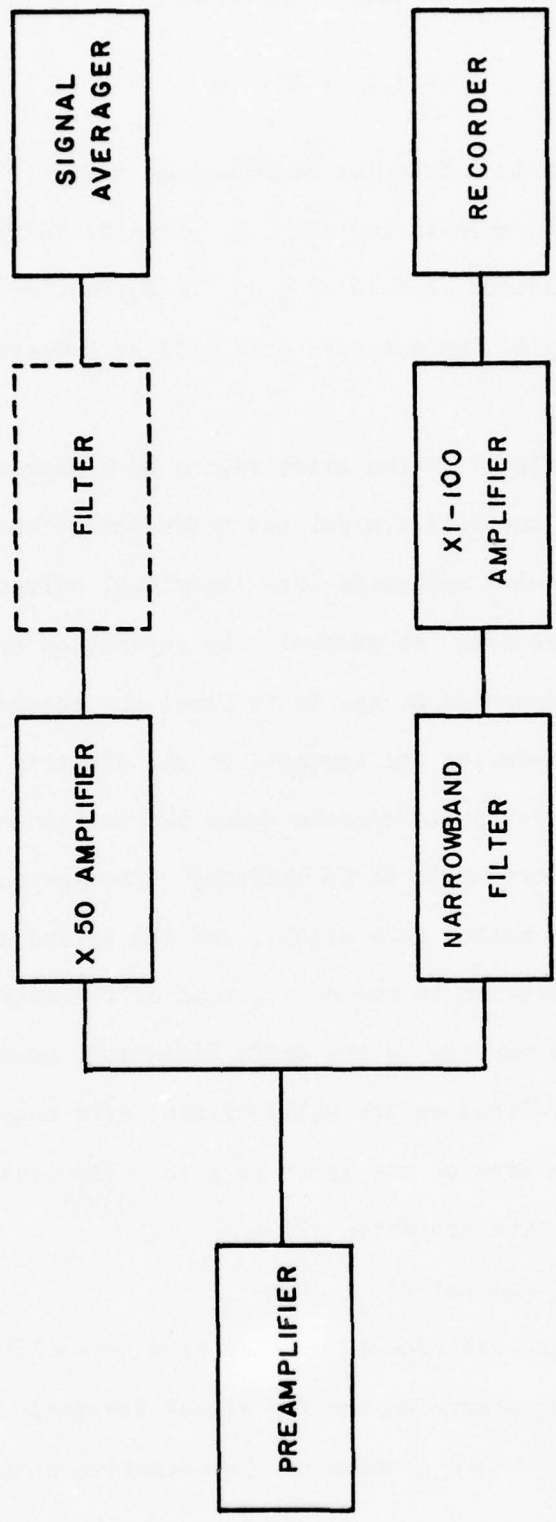
Figure 2.3. Block diagram of detection electronics.

14

The collector plate is connected to an electrometer preamplifier by a short, rigid coaxial line with sapphire insulators. Because the signal currents expected are so small, the preamplifier is the most critical part of the signal detection chain.

2.3.1 Preamplifier

The preamplifier is adaptable to use with either the one-grid mode or the two-grid mode of operation. In the one-grid mode, a fast response is necessary to prevent a loss of resolution in the ion peaks and to provide accurate arrival time information for measuring mobilities. In the two grid mode, a much slower response time is not only possible but also desirable in order to reduce the noise contributed by the preamplifier itself, and thus obtain lower levels of detectability for particular ions.

The heart of the preamplifier is an electrometer operational amplifier, a Burr-Brown 3421K. It has a very high input impedance, a very low bias current, and a low noise voltage and current. A detailed noise analysis of this and other preamplifiers is provided in Appendix 1, but the general guideline for current amplifiers is to decrease amplifier noise by increasing the input resistance. In the Beta/VII PC, the resistor used in the one-grid mode is 10^8 ohms, while that used in the two-grid mode is 10^{11} ohms. A simplified schematic of the preamplifier appears in Figure 2.4.

The feedback resistors determine the current-to-voltage conversion ratio, as well as the preamplifier noise, and have a major role in determining the frequency response. The effective input resistance of

15
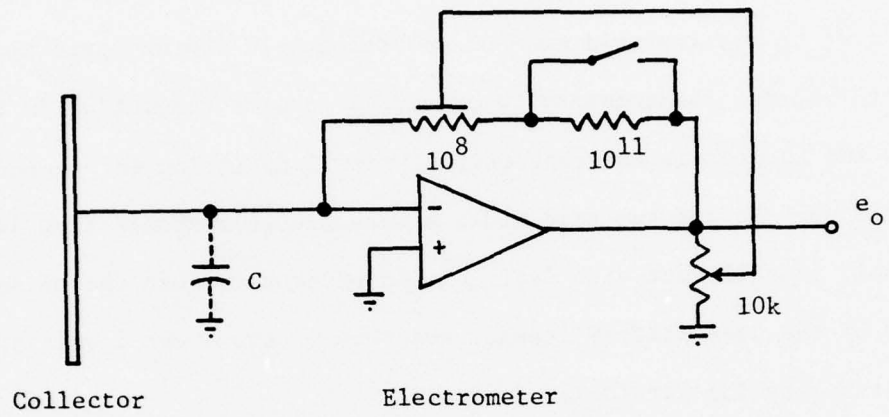
Figure 2.4.   Schematic diagram of preamplifier.

16

the current-to-voltage converter is given by the feedback resistance divided by the gain of the amplifier plus one, where the gain is frequency dependent:

$$R_{in} = \frac{R_f}{1 + A(\omega)} \cdot \qquad (2.5)$$

This input resistance, in parallel with the capacitance to ground of the collector plate, limits the frequency response of the converter. It also creates a potential instability in the amplifier which may result in oscillations. To prevent this, a distributed capacitance in the form of a tubular shield around the 10^8 ohm resistor is driven with a fraction of the output voltage, resulting in a capacitive feedback that can be adjusted to compensate the input capacitance. The compensation reduces the frequency response while stabilizing the amplifier. The frequency response is inversely proportional to the feedback resistance.

A resistor of $2.1 \cdot 10^9$ ohms was connected to the input terminal of the electrometer and driven with a variable frequency generator to measure the frequency response of the preamplifier. The frequency responses for the 10^8 ohm and 10^{11} ohm resistor are shown in Figure 2.5. The peaks at high frequencies are attributed to the effects of the distributed feedback capacitance and the input capacitance. The half-power bandwidths are approximately 50 kHz for the 10^8 ohm feedback resistor and 0.5 Hz for the 10^{11} ohm resistor.

2.3.2 Noise Measurement

The noise characteristics of the electrometer depend upon the bandwidth chosen for the measurement. Although noise voltages and currents are best measured with a true RMS voltmeter or ammeter, a

17
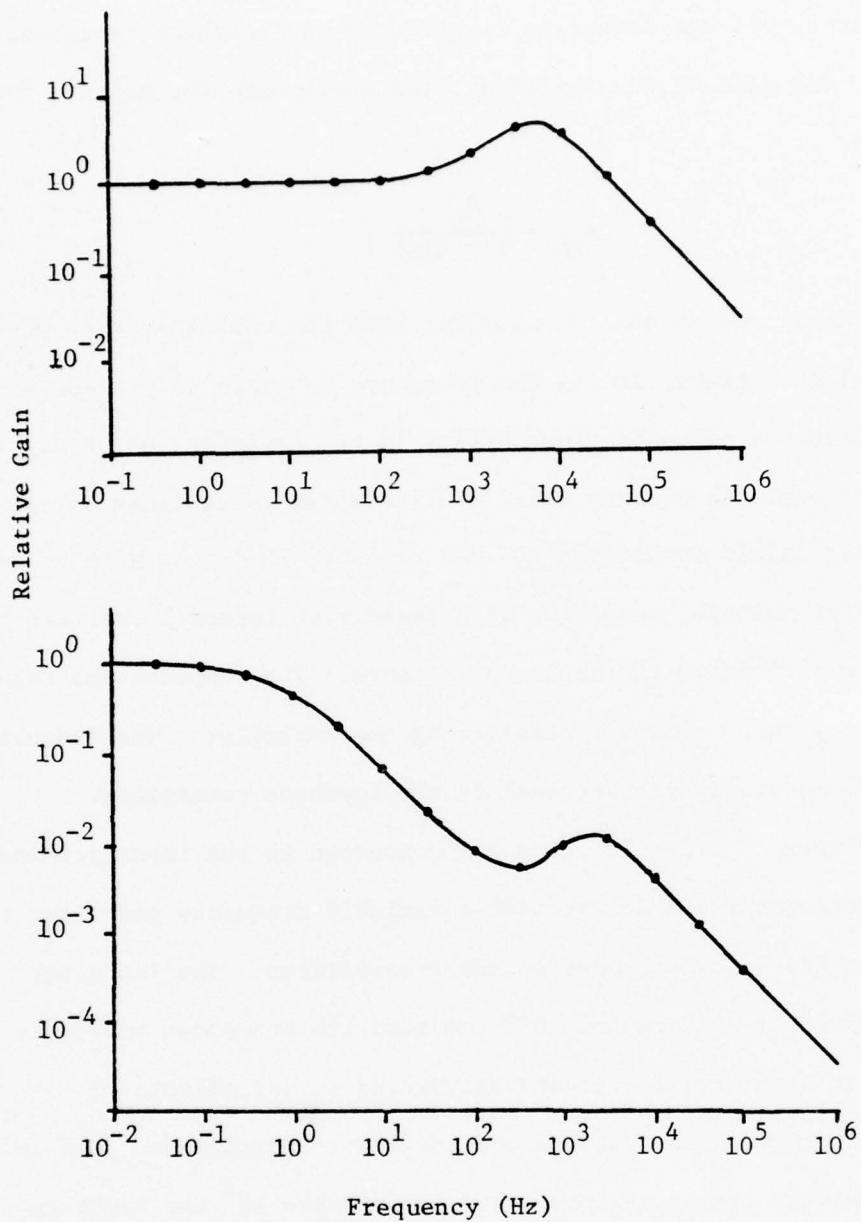
Figure 2.5. Frequency response curves for the preamplifier. Feedback resistor 10^8 ohms (upper curve) and 10^{11} ohms (lower curve).

18

reasonable approach is to measure the tangential noise at the 99 percent level and calculate the RMS value. That is, an upper and a lower level are determined which includes 99 percent of all the random noise peaks; the RMS noise level is then one-fifth of the difference between the upper and lower levels. For most applications, the 99-percent levels are set only approximately, but the error introduced is not especially critical. All noise levels reported here are calculated by the tangential method. Further, all noise levels are referred to the input of the electrometer by dividing the output noise voltage by the gain of the electrometer.

The RMS noise referred to the input as measured for the one-grid mode on an oscilloscope is approximately $6.7 \cdot 10^{-12}$ A. The bandwidth of the oscilloscope used greatly exceeded that of the preamplifier, so that this value is the maximum noise output from the preamplifier. Filters and other noise reduction schemes may be used to reduce this value.

2.3.3 Signal Averaging

The principal noise reduction technique used with the one-grid mode is that of signal averaging. In signal averaging, multiple repetitions of a signal are summed and stored. Time-coherent signals, especially the signal components, add linearly, while non-coherent signals, such as noise, add in quadrature. The result is that the signal amplitude grows in proportion to the number of sweeps, while the noise grows only as the square root of that number. Thus, the signal-to-noise ratio improves directly as the square root of the number of repetitions summed.

19

The main limitation of the technique is that the time involved in accummulating the repetitions increases directly with the number of sweeps used.

The Nicolet 1072 signal averager used in this research has wide ranging capabilitites for averaging. The specific parameters that were important in the measurements to be described are the channel capacity, channel dwell time, and prefilter time constant. The channel capacity is 1024 channels, which can be subdivided in halves or quarters. The channel dwell time used was 20 microseconds per channel; it could be increased to 10 seconds per channel in a 2-4-10 sequence. The prefilter time constant used was 20 microseconds; it could be increased to 100 milliseconds a 2-4-10 sequence.

With this choice of operating parameters, the sweep of all 1024 channels would take 20.48 milliseconds, a convenient value matching the sweep capabilities of the Beta/VII. The Nicolet 1072 was triggered by a pulse coincident with the Gate 1 opening pulse, and would record the subsequent arrivals of the ion bunches. The prefilter was normally set at a value equal to the channel dwell time to provide discrimination against aliasing by higher frequency components of noise and signals.

The prefilter is a single-pole RC filter. With a time constant of 20 microseconds, its half-power bandwidth is about 8 kHz. The noise-effective bandwidth, which is equal to 1/4 RC for a single pole filter, is 12.5 kHz. Thus, the prefilter restricts the bandwidth of the measurement even before averaging begins. The RMS noise of the electrometer, measured with the Nicolet 1072, is $3.4 \cdot 10^{-12}$A, somewhat, lower than the oscilloscope measured value. The prefilter also reduces the high frequency peak in the electrometer response somewhat, producing a more uniform response.

2.3.4 Drift Velocity Measurement

Since the channel identification capability of the Nicolet 1072 provides a direct way to measure the arrival time of the ion bunch, and thus determine its mobility, a brief discussion of the arrival time measurement is in order. The ion bunch is introduced to the drift region as a rectangular pulse with a duration equal to the gate width, t_g. The peak spreads by diffusion and space charge effects as it travels to the collector (Reference 4), but the characteristic velocity is assumed to be that of the center of the peak. Thus the transit time is the time between the center of the Gate 1 pulse and the arrival of the center of the peak, and

$$v_d = \frac{8.0}{t_a - t_g/2} , \qquad (2.6)$$

where v_d is the drift velocity in centimeters per second, t_a the measured arrival time of the peak, and t_g the gate width.

The arrival time is commonly taken as the channel number of the peak times the channel dwell time. This estimate of the arrival time neglects the effects of triggering the Nicolet and of the prefilter. Because the Nicolet is clocked by an internal oscillator on negative transitions of the clock pulse, a sweep can be initiated only when synchronized with a clock pulse. The arrival of a trigger pulse at the input terminals of the Nicolet will occur, on the average, halfway between clock pulses; that is, the beginning of the sweep will be delayed by one-half clock period. The delay of the signal introduced by the prefilter is equal to the time constant of the filter. These effects are in opposite directions. For a filter time constant and channel dwell time each of 20 microseconds, the total delay introduced would be 10 microseconds.

21

Measurements to determine whether or not these effects were indeed valid were performed. The actual time constant of the prefilter was calculated as 27 microseconds from its measured frequency response. Then rectangular pulses were used as both trigger and signal. The time difference between the two pulses could be varied and could be measured directly. By comparing the measured delay between the two pulses with the computed delay (channel number x dwell time per channel), the intrinsic delay of the filter and triggering circuit could be measured. When the pulse arrival time was measured at 90 percent of pulse height, a more convenient value than 63 percent, the delay was 58 microseconds. The calculated delay for the same 90 percent rise time was 52 microseconds, in good agreement with the measured value. Thus, we conclude that the true drift velocity is best approximated by the formula:

$$v_d = \frac{8.0}{t_a + \frac{1}{2} t_{dw} - t_g/2 - TC} \, , \qquad (2.7)$$

where t_{dw} is the channel dwell time and TC is the actual prefilter time constant.

2.3.5 Effective Bandwidth

Since the signal averaging technique can take a considerable time if the number of sweeps averaged is large, it is useful to define an effective bandwidth for the averaging process. If N sweeps require $N\tau$ seconds to be accummulated, where τ is the duration of one sweep, then the effective bandwidth would be

$$BW_{eff} = \frac{1}{2N\tau} \sec^{-1} \, . \qquad (2.8)$$

Frequencies or amplitudes that change faster than the effective bandwidth will be attenuated. The factor of two comes from the

22

Nyquist sampling theorem, requiring a signal to be sampled at twice the rate of its highest frequency of interest to achieve no loss of information. The purpose of defining this effective bandwidth is to facilitate comparison of noise levels for different modes of PC operation.

In the two-grid mode of operation, the preamplifier feeds an amplifier-filter for further processing. The amplifier has switch-selectable DC gains from one to one hundred, and the filter, a four-pole low-pass type, has switch-selectable time constants from 10 milliseconds to 10 seconds. The combination allows selection of appropriate full-scale gain to handle the signals expected and sufficient filtering tc remove noise from the signal.

The intrinsic noise of the preamplifier establishes a lower limit on the detectability of signals. Measurements were made of the preamplifier noise with no voltage applied to the drift tube in order to ensure that only the amplifier noise was measured. Various filter time constants were used to obtain frequency dependent noise values. All semiconductors exhibit a phenomenon known as "1/F" noise, a noise spectral characteristic in which the noise power per unit bandwidth increases as the frequency of measurement decreases. The result of this characteristic is that the noise amplitude remains constant no matter how long the filter time constant is made. There is an optimum filter frequency below which the response time becomes degraded without benefit of improving signal-to-noise ratio.

Measurements confirm this expectation. The noise measured using the 10^{11} ohm resistor is essentially constant for filter time constants less than 100 milliseconds. A similar result holds for the 10^8 ohm

23

feedback resistor, even though in practice it is not used in the two-grid mode of operation.

The noise-effective bandwidth of a single pole filter has been given as $1/4\tau$, where τ is the time constant and is equal to RC. This bandwidth is about fifty percent larger than the standard half-power bandwidth calculated from τ because the high frequency components of noise, even though attenuated, still contribute to the total noise. For a four-pole filter, the attenuation of high frequencies is so severe that the noise-effective bandwidth is nearly equal to the half-power bandwidth. Specifically, for four isolated RC sections in series,

$$BW_{eff} = \frac{5}{64RC} \tag{2.9}$$

where BW_{eff} is the noise-effective bandwidth. This was used to calculate the bandwidths used. Since the noise power per unit bandwidth varies as $1/F$, the noise current per (unit bandwidth)$^{1/2}$ should vary as $1/F^{1/2}$. This is plotted in Figure 2.6. Also plotted are the noise currents produced by the feedback resistors as a function of bandwidth, calculated from:

$$I_{NR} = \left(\frac{4k_B T}{R} \, BW_{eff} \right)^{1/2}, \tag{2.10}$$

where T is the absolute temperature and I_{NR} is the RMS noise current due to resistance. It is seen that the excess electrometer noise tends toward a value which can be interpreted as entirely due to the resistor noise.

Published specifications for the Burr-Brown 3421 amplifier show a noise current contribution from the bias current of the amplifier of

24
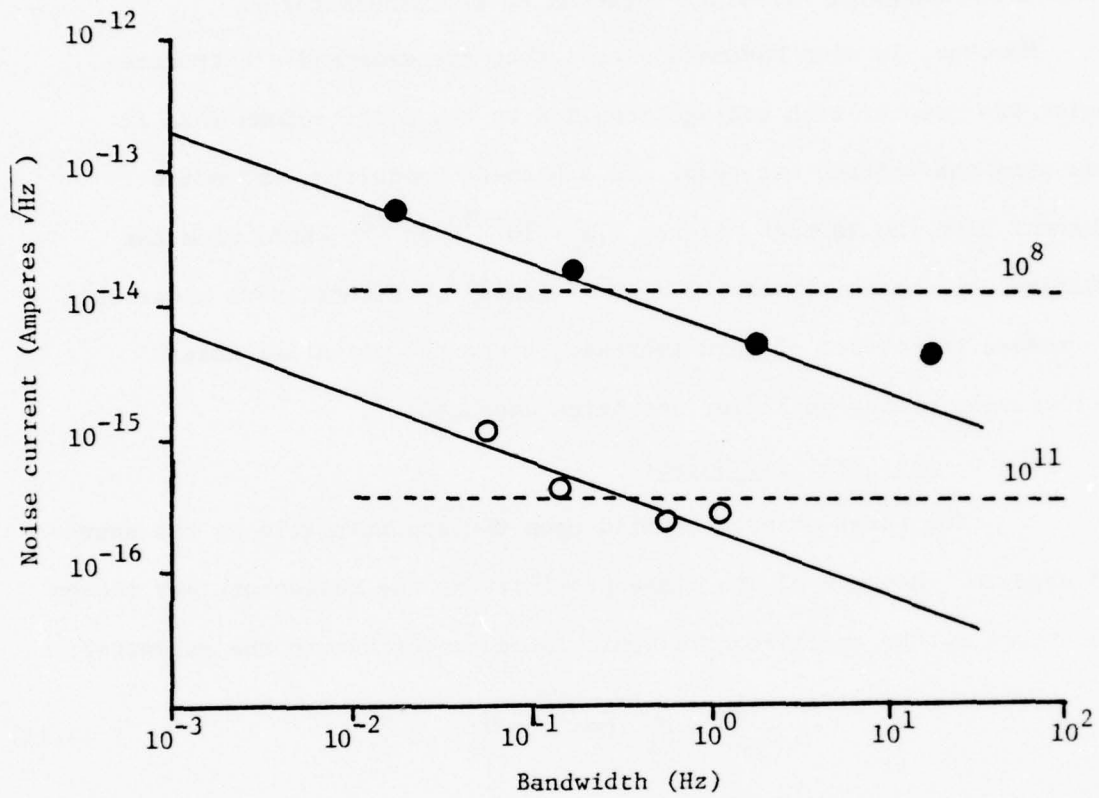
Figure 2.6. Preamplifier noise current. Solid lines represent 1/F power law. Dashed lines are the resistor noise currents for each value resistor.

25

approximately $9 \cdot 10^{-14}$ A/Hz$^{1/2}$ for bandwidths below 10 Hz. Since the measured noise is almost an order of magnitude less, the manufacturer was consulted. The amplifier apparently is an exceptional unit, but within the range of variation expected by the manufacturer.

However, it soon became apparent that the measured electrometer noise was greater with voltage supplied to the drift column than it was when the voltage was zero. In a 0.25-Hz bandwidth, the noise current with the voltage off was $2.1 \cdot 10^{-15}$ A/Hz$^{1/2}$; while with the voltage on, the noise was $1.2 \cdot 10^{-14}$ A/Hz$^{1/2}$. Efforts were undertaken to assess the causes of this increase, since the potential noise performance of the amplifier was being degraded.

2.3.6 Aperture Grid Noise

The first efforts settled upon the aperture grid as the source of trouble. Because of its close proximity to the collector, any change in charge on the aperture grid would induce a current in the collector:

$$I = \frac{dQ}{dt} = \frac{d}{dt} (CV) = C \frac{dv}{dt} + V \frac{dC}{dt} , \qquad (2.11)$$

where I is the current induced, Q is the charge on the aperture grid, C is the capacitance of the grid with respect to the collector, and V is the voltage on the grid. Any change in either voltage or capacitance would appear as a current in the collector.

The steady state voltage for the aperture grid is supplied from the same divider chain that establishes the voltage gradient along the drift column. The aperture grid voltage is 0.7 percent of the total high voltage applied. Because the resistors in the divider chain are highly stressed by both voltage and temperature, they may contribute

26

noise to the aperture grid. The grid is AC bypassed through a 2.0-microfarad capacitor. Simple tests showed that increasing the capacitor to about 50 microfarads reduced the noise in the electrometer to half its prior value, $1 \cdot 10^{-15}$ $A/Hz^{1/2}$. Further increases in capacitance produced no benefit. This value is still considerably larger than that obtained with the voltage off.

With the 50 microfarad capacitor in place, the noise bandwidth of the aperture grid circuit is 0.025 Hz. If voltage changes occur randomly within the resistor chain, how much change would be required to explain the measured noise? Using Equation 2.11 with C held constant, the value of dV/dt calculated is $1.8 \cdot 10^{-5}$ volt/sec. This is quite a stringent specification for any power supply; for the high voltage supply of the PC, the limit is increased by the divider ratio to about $2.5 \cdot 10^{-3}$ volt/sec. The specifications for the high voltage supply in the Beta/VII appear to remove it as the source of noise, but substandard performance or excessive line voltage variations could contribute to the noise problem. The fact that further increases in capacitance on the aperture terminal did not reduce the noise would also tend to mitigate against the power supply as the source.

In Section 2.2, a calculation was made of the thermal motion of the aperture grid. To continue the calculation, the effects of that motion on collector current noise will be evaluated. In a capacitor with a spacing d between plates, the change in capacitance due to a small fluctuation in spacing Δd is given by:

$$\Delta C = -C_o \frac{\Delta d}{d} , \qquad (2.12)$$

where C_o is the capacitance at rest. If the fluctuations are in a normal mode of vibration of the capacitor plates, then the change will take place

27

in a time roughly equal to one-sixth the period of the mode. The current
induced in the collector plate will then be

$$I_n \simeq V2\pi \frac{\Delta C}{T} = VC_o \frac{\Delta d}{d} 2\pi f , \qquad\qquad (2.13)$$

where T is the mode period and f is the frequency of the mode. If we
assume Δd is the RMS displacement of the plate, then the noise current
calculated is $2.7 \cdot 10^{-15}$ $A/Hz^{1/2}$. The electrometer does not respond to
the high frequency ringing of the diaphragm, but to the fluctuations
in the motion that fall within its bandwidth.

The calculation is crude, glossing over averages that could be
calculated, ignoring higher modes which have been observed. Nonetheless,
the noise current calculated was sufficiently close to the measured value
to stimulate an investigation of the temperature and voltage dependence
of the current.

Measurements of the total noise current were made with the high
voltage on and off at the operating temperature of 200°C and at a value
near room temperature, 24°C. The noise measured at room temperature
with the voltage on was indeed lower. However, it was noted that the
noise with the voltage off was also lower. Subtracting the intrinsic
electrometer noise from the total noise (in quadrature), a value of
excess noise for each temperature was obtained. The ratio of the
excess noise at 200°C to that at 24°C was about 1.8, while the ratio of
absolute temperatures was about 1.6. This is out of line with the
prediction that the amplitude of thermal agitation should be proportional
to the square root of the absolute temperature, but then, too, the amount
of temperature change was not very large in consideration of the crudeness
of the noise measurement.

28

The voltage dependence was measured by turning the high voltage off and connecting a power supply to the aperture grid terminal. Tests were run to see that the power supply itself was not the source of noise being measured. With voltage of either polarity on the grid, the excess noise was present from a threshold voltage of 1 volt to 40 volts. Below 1 volt, the noise measured was just that of the electrometer, but over the range of voltage, there was only a slight increase in the excess noise. This is not expected from Equation 2.13, but it could be interpreted as caused by the buildup of a surface charge on the collector due to a monolayer of insulating material.

In conclusion, while the evidence does not allow a definitive statement about the noise due to the aperture grid, the grid does produce noise in response to mechanical shocks, the noise does exhibit a temperature dependence, and simple calculations give reasonably close predictions of the measured noise. Therefore, thermal agitation of the aperture grid is a likely cause of the excess noise of the PC in the two grid mode.

2.3.7 Comparison of One-Grid and Two-Grid Noise

Based upon the measured noise levels of the one-grid and two-grid modes, the two-grid mode appears to have a superior advantage for detection of signals. To examine this advantage quantitatively, we need to compare the two noise levels at comparable bandwidths, making use of the effective bandwidth defined for the signal averager, Equation 2.8. Let us choose the bandwidth to be 0.25 Hz. Then, from Equation 2.8 and assuming a 25-millisecond sweep duration, the number of sweeps required is 80, and the time required to accummulate them is 2 seconds.

The signal-to-noise improvement factor for 80 sweeps is 8.9, resulting
in an equivalent broadband noise after averaging of $3.8 \cdot 10^{-13}$A. In
the two-grid mode, the noise level is much lower, 10^{-15}A, but the
equivalent signal level is much lower. The reason for this is that
the signal of interest comes through the second grid as a short duration
pulse, but it is averaged over the entire length of the sweep cycle
until it is repeated. In the one-grid mode, an ion peak always stands
the same height above the noise, no matter what, the repetition rate.
This reduction in average current is called the duty factor limit, and
the duty factor itself is defined as the ratio of the Gate 1 pulse width
to the repetition period of the Gate 1 pulse. The Gate 2 width can also
affect the duty factor, but in this work the Gate 2 width was always set
to accept all the ions admitted by the first grid; a more restrictive
Gate 2 width would further reduce the duty factor. In this research,
the duty factor was nearly always $8 \cdot 10^{-3}$. To obtain a noise level
for two-grid operation equivalent to that for one-grid operation, the
noise should be divided by the duty factor. This gives an equivalent
noise for the two-grid mode of $1.3 \cdot 10^{-13}$A. (This value is obtained
with the 50-microfarad capacitor on the aperture grid terminal.)

Thus, the two-grid mode of operation has a signal-to-noise advantage
of about a factor of 3, which could be overcome in the one-grid mode by
further averaging. In typical laboratory use, the number of sweeps
averaged was often as large as 8192 when the signal of interest was very
small. This would produce an equivalent noise level of $3.7 \cdot 10^{-14}$A,
or approximately three times lower than the two-grid mode offers.

The equivalent noise performance of the two-grid mode cannot be
improved by further averaging because of the 1/F spectral character of
its noise, but it is a sensitive function of the duty cycle, and potential

30

improvements can be made there. The extra information about all the ions provided in the one-grid mode must be weighed against the extra time required to obtain the same signal-to-noise ratio as in the two-grid mode.

2.4 Control Electronics

The control section of the Beta/VII plasma chromatograph consists of the circuitry for opening the grids and for supplying the proper operating voltages to the drift tube. The circuits are interrelated because the shutter grids must operate at, or close to, the potentials characteristic of their position in the drift column.

The voltage gradient along the column is established by two parallel voltage dividers. One set is mounted in the SIFAD and consists of 2.0-megohm resistors spot-welded between the rings of the drift column. The other set consists of 150.0-kilohm resistors which are mounted in the PC controller. The two dividers are electrically connected together at the high voltage end, at the zero voltage end, and at the Grid 1 and Grid 2 reference points. These connections are accessible at the back of the controller.

The actual voltages on the shutter grid wires are derived from the current flowing down the controller divider. Each circuit is maintained at the average potential of its particular reference. The shutters are opened (grid wires brought to the same potential) by a current pulse from the controller circuits which is transferred by means of an optical coupler. In this way, the grid circuits can be maintained at high voltages while the controller circuits are maintained at much lower operating voltages.

The PC controller can operate as a repetitive pulser or can accept an external trigger pulse to initiate the sequences for opening the two grids. The trigger input circuitry is adjustable for accepting pulses

31

of either polarity, of variable levels, and for triggering on the rising or falling edges. The circuit incorporates a Schmidt trigger, allowing even sine waves to be used to initiate the sequence. A relatively minor modification to the controller allows the external signal to hold the first grid open as long as the signal is above the input threshold. This is detailed in Appendix 3.

Upon receipt of a trigger signal, a monostable multivibrator produces a pulse for Gate 1, which is fed through the optical coupler. The same pulse is available on the front panel for other timing and triggering purposes; it is used to begin the sweep on the Nicolet 1072 signal averager, for instance. The duration of the Gate 1 pulse is switch-selectable from 50 microseconds to 1 millisecond.

The trigger signal also begins the generation of a linear ramp voltage, which begins at zero volts and ends at -5 volts. The rate at which the voltage changes is set by a front panel switch: The ramp duration can be varied from 10 microseconds to 1 second in a 1-2-5 sequence. For this work the duration chosen was always 20 milliseconds. A voltage comparator monitors the ramp signal continuously, and when the ramp level reaches its comparison level, the Gate 2 pulse is generated. By varying the comparison level between 0 and -5 volts, any percentage of the ramp duration can be selected as the delay time between the pulse on Grid 1 and the pulse on Grid 2. The comparison level is set by a front panel control. Although there is circuitry in the controller for slowly scanning the comparison level over its range, this feature was not used in this work.

32

The pulse for Grid 2 is continuously variable in width from 10 microseconds to 100 milliseconds, but in practice was usually 0.5 to 1.0 millisecond in duration.

Two front panel switches allow either grid to function normally or to be held open continuously. For instance, for one grid operation using the signal averager, the second grid is left continuously open. Or, the first grid can be held open continuously, allowing the second grid to serve the function of the first grid, with a 2 centimeter drift distance.

A measurement of the actual grid voltage during a pulse was made to see how much spread in the ion pulse might be introduced. The second grid operates at about 14 percent of the applied high voltage potential, so it was possible to use an AC-coupled oscilloscope to view the grid potentials without exceeding the DC rating of the blocking capacitor in the scope. The measured opening time of the grid, using the standard rise time points, was 0.8 microsecond at a high voltage potential of 2000 volts. At 1000 volts, it was slightly longer, about 1.2 microseconds. The closing time for the grid was 27 microseconds for either voltage. This asymmetry for opening and closing is to be expected from the circuit used and is mainly attributed to the cable and grid wire capacitances. The long closing time is a significant fraction of the gate widths used, and some attempts were made to shorten it. It was found that simple modifications would not be sufficient to decrease the closing time, but that it should be possible to reduce the closing time by optimizing the grid circuit for a particular value of high voltage. No modifications were actually made because they would have restricted the utility of the instrument.

33

These voltages are measured for the grid wires, but do not necessarily represent the true rise and fall times of the ion pulse, since ion transmission is probably a non linear function of grid voltage. Measurement of the ion transmission as a function of voltage would have to be done in a DC mode, since the response time of the electrometer, even in the one-grid mode, is too slow to avoid distorting the rise and fall times in the actual ion pulse. Such a measurement for both hydrated ions and free electrons is shown in Figure 2.7, plotting the current at the collector as a function of the maximum voltage applied between wires. For this measurement Grid 1 was held open, Grid 2 was not pulsed, and the voltage across the grid wires of Grid 2 was measured.

Using as a definition for the ion pulse rise and fall times the time spent between 10 percent and 90 percent of the final value, the calculated rise and fall times for hydrated ions is 0.63 microsecond and 17.0 microseconds respectively. For the free electrons, the rise and fall times are 0.66 microsecond and 17.8 microseconds, with the electrons never being completely cut off. This indicates an improvement in the ion pulse shape, but the fall time is still large for some investigations.

2.5 Temperature Measurement and Control

The PC is usually operated at elevated temperatures in order to reduce contamination of the instrument by vapor species which readily condense. In particular, TNT exhibits a very low vapor pressure and a strong tendency to adsorb to metal surfaces. For this reason, the operating temperature of the PC was set at 200°C.

The temperature is established by custom-fitted heating mantles around the SIFAD. There are three mantles: one covering the inlet structure, one for the body of the SIFAD, and one for the back flange of the SIFAD.

34
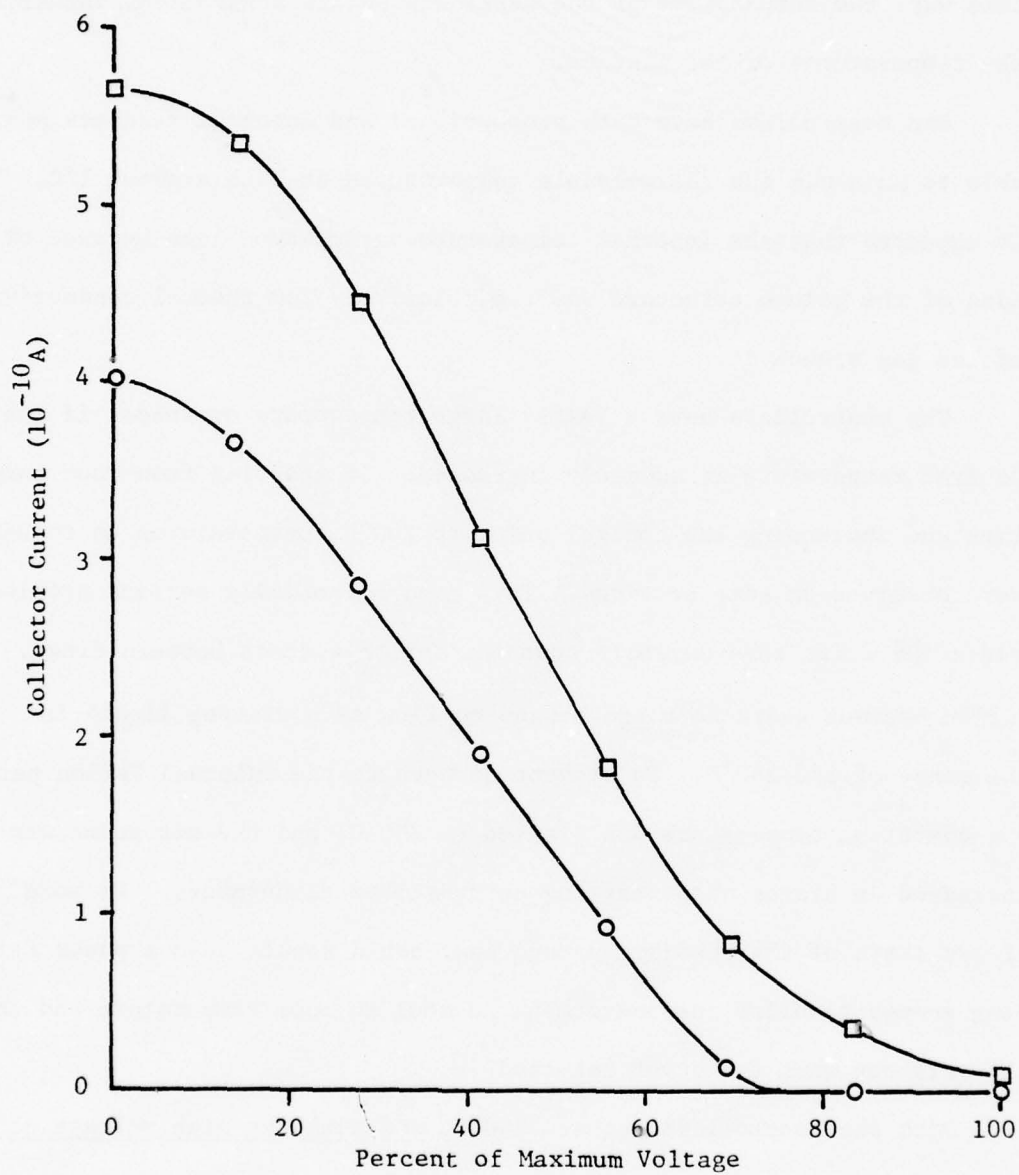
Figure 2.7. Grid transmission current as a function of voltage between wires. Squares are for electrons, circles for hydrated ions.

The mantles are connected to electronic controllers, which measure the temperature in each section by thermocouples bolted to the SIFAD. In this way, the temperature of the metal chamber is controlled, rather than the temperatures of the mantles.

The controllers have both proportional and integral feedback and are able to maintain the thermocouple temperatures to within about 1°C. It is expected that the internal temperature varies even less because of the mass of the column structure and the relatively low thermal conductivity of the gas around it.

The controllers have a fairly large temperature overshoot if the desired temperature is suddenly increased. In starting from room temperature and increasing the control point to 200°C, temperatures up to 240°C were observed on some sections. This is a potentially serious problem, since the drift tube assembly contains Teflon spacers between rings. Teflon becomes quite soft and begins to flow as a viscous liquid in the range of 240-260°C. To prevent damages to the internal Teflon parts, the operating temperature was limited to 200°C, and the set point was increased in stages when starting up from room temperature. We were always aware of the possible damage that could result from a power failure long enough to allow the instrument to cool to room temperature and then to overshoot when the power returned.

With the controllers set at 200°C, and with the high voltage off, a thermocouple probe was inserted into the instrument, both through the inlet port and through the outlet port. Through the inlet, the thermocouple measured a temperature in the vicinity of the diffuser in the reaction region of precisely 200°C. When inserted through the outlet,

36

the thermocouple was placed in contact with the ring structure of the drift region, where the temperature measured was 191.5°C. It was felt that the lower temperature in the drift region was due to the relatively large area devoted to electrical feed through connectors in the outer shell. There is no heat supplied in that region.

These temperature inhomogeneities were not thought serious and were ignored. The reaction region is at the nominal 200°C, so that reaction rates are being measured at that temperature. In the drift region, there would be a small correction necessary when calculating the reduced mobility of an ion.

3.0 DILUTION FLASK EXPERIMENTS

The dilution flask is a mixing volume into which pure carrier gas flows and into which a known quantity of vapor sample is injected. If instantaneous mixing occurs at all times, then the concentration of molecules leaving the flask is given by

$$N = N_o \exp \left(- \frac{\dot{F}}{V_f} t \right), \tag{3.1}$$

where N_o is the initial concentration of sample vapor, $\dot{F}$ is the volume flow rate of the carrier gas, and V_f is the volume of the flask. The use of the experimental dilution flask for calibration has been described in the literature (References 5-8). It is possible, in theory, to make a sensitivity and linearity measurement for a detector over the entire range from saturation to the limit of detectability with one injection. In practice, sources of error need to be accounted for.

3.1 Physical Characteristics

The flask is cylindrical, 7 centimeters in diameter and about 15 centimeters tall. The bottom and top of the cylinder are nearly flat.

The flask is constructed of Pyrex glass, and a Pyrex stirring fan is located along the central axis of the cylinder. The stirring fan consists of a shaft with six paddle blades distributed along its length in pairs and with a glass-enclosed magnetic rod near its base to provide motive power. The lower shaft end rests in a dimple in the bottom of the cylinder, and the upper end turns in a loosely fitting glass sleeve. The effective diameter of the fan blades is about one-half the flask diameter. The most important parameter describing a dilution flask, its

38

volume, was determined to be 469 cm^3 by filling the flask with water and pouring into a graduated cylinder.

The gas inlet to the flask is at the top of the cylinder and extends about a centimeter into the flask itself. The inlet arm also contains a small diameter hole for inserting a syringe for injections. Depending on the depth of insertion, the sample can be injected wholly in the carrier gas stream, or it can be injected into the major part of the volume. The outlet from the flask is from the side wall of the cylinder at a point near the bottom. The rotation of the stirrer forces the mixed gases toward the outlet port.

The whole flask is enclosed in a small oven designed to sit on a stirring hot plate. The inlet and outlet tubes (6 mm Pyrex) pass through the back wall of the oven for external connections. The height of the outlet tube is such that it can feed the PC inlet directly. The syringe injections are made through a small access hole in the top of the oven. When the syringe is not in place, the hole in the inlet arm is plugged with a small, tapered Teflon rod, similar in size to the syringe.

The temperature of the flask was measured with a thermocouple inserted into the oven through another small access hole. Because of limitations in the hot plate, the maximum temperature ever reached was 195°C, with operation at 190°C more usual. Some data were run with the oven and PC at 160°C; the temperature stability was very reasonable at the lower temperature.

The rotation of the stirrer was not very smooth, and higher speeds generated unacceptable noise levels in the plasma chromatograph because of its sensitivity to vibration. Consequently, most of the data were run using

39

the minimum speed of 60 RPM. Comparison of dilution data taken with speeds ranging from 0 to 200 RPM showed no significant differences, except in the first minute after injection. With the stirrer off, there was evidence that initially a higher than average concentration of vapor was passing into the PC without being properly diluted. At longer times, the dilution rate was the same as that obtained by operating the stirrer. The same phenomenon was noted when very high volume flow rates were being used.

The rotation of the stirrer was accompanied by considerable wear in the lower bearing. A quantity of ground glass accummulated in the bottom of the flask over a period of weeks. This was removed several times during the research, with the concern that the presence of the large surface area of the powder would cause increased adsorption of *vapor.* Measurements before and after the powder was removed did not substantiate this concern.

The Beta/VII plasma chromatograph was supplied with a quartz inlet tube (6 mm o.d.) which was long enough to reach the diffuser in the reaction region while protruding nearly to the end of the inlet heating mantle. This tube was connected to the outlet of the dilution flask by a short section of heat-shrinkable Teflon tubing (Pope Scientific). This provided a gas-tight seal of inert material. The Teflon showed a slight tendency to flow at 200°C over a period of months, but no detectable leaks developed. A space of about 4 mm was left between the ends of the Pyrex and quartz tubes to allow a small degree of flexibility between the flask and the PC.

The inlet connection between the flask and the carrier gas supply was originally made with Teflon (TFE) tubing at room temperature. Operating experience with chlorobenzene led us to suspect that back diffusion was occurring and that the Teflon was adsorbing sample molecules strongly. Ultimately the connecting line was made of stainless steel tubing, with a short section of flexible stainless bellows tubing right at the flask inlet. The connection to the pyrex tubing of the flask was made with a Swagelock connector with Teflon inserts. The inlet supply line was wrapped with a heater tape from the gas valve on the PC all the way to the flask oven and was heated to 200°C normally (lower, at the lower operating temperatures). These precautions eliminated any adsorption attributable to the inlet line and minimized the temperature discontinuity between the line and the flask.

Following the last cleaning of ground glass from the flask, the flask and quartz inlet tube were treated with a five-percent solution of dimethyldichlorosilane in toluene. The purpose of this treatment was to saturate all the chemisorption sites on the glass surface with strongly bound molecules. The glass surface was suspected of being the source of a steady background ion current corresponding to a chloride ion. The treatment appeared to be successful in causing a great reduction in the background ion current.

3.2 Operation of the Dilution Flask

When the dilution flask is at an operating temperature of 200°C, its volume is larger than at room temperature due to the thermal expansion of the Pyrex. Using the published expansion coefficients, this effect was calculated to increase the flask volume from 469 cm^3 to 470 cm^3.

41

In addition to the dilution flask volume, the other operating parameter essential to calculating the ideal dilution rate is the volume flow rate of the carrier gas. All flow controllers and flowmeters were operated and were calibrated at room temperature. When the flowing gas is heated in the inlet line, it tends to expand, resulting in a higher volume flow into the flask. Assuming that the pressure in the line remains unchanged as the gas expands, the increased flow rate is proportional to the increased absolute temperature according to the ideal gas law. (A check of the volumetric expansion using the VanderWaals' constants for nitrogen revealed that negligible error was introduced by using the ideal gas law.)

In practice, it was found that the pressure in the PC did increase slightly above atmospheric. This could be observed by using an air carrier in the negative ion mode. With the flask tightly closed, the characteristic spectrum of air was obtained; but with the syringe hole open to the atmosphere, the nitrogen drift gas flushed the air out of the reaction region, even though the normal exit was also at atmospheric pressure.

In an attempt to maintain the pressure in the flask at near atmospheric, a suction pump was connected to the outlet of the PC. The pressure in the suction line was measured with a simple manometer that was open to the atmosphere on one side. The working fluid in the manometer was a silicone oil, whose low density provided a sensitive measure of pressure difference. By adjusting the speed of the suction pump, the flask and PC could be operated above or below atmospheric pressure.

When operating the flask below atmospheric pressure, as evidenced by removing the syringe-hole stopper and seeing the spectrum of lab air

42

appear, a pressure head of 5 to 6 centimeters of oil equivalent pressure could be sustained by the closed flask before any outside air could penetrate the system. This was an operational measure of the tightness of the system. During a dilution run, the manometer pressure was maintained at about 1 centimeter less than atmospheric. This pressure was not low enough to draw laboratory air into the flask while injecting a sample, but did maintain the flask pressure much closer to atmospheric that would have been achieved otherwise. The near-normal pressure in the flask reduced the amount of backflushing and sample loss that were experienced.

Use of a septum over the syringe hole was considered and finally rejected because of the unknown adsorption characteristics of the septum material for TNT vapor. Instead the Teflon stopper, described earlier, was used to close the hole between injections, and the syringe needles were sheated with a small diameter Teflon tubing, which was tapered to fit tightly in the hole. Thus the flask was open to atmospheric pressure for only two or three seconds while the needle was inserted or removed. While the hole was open, the signal level in the PC dropped considerably, but this drop probably represented a loss of flow through the reaction region rather than a loss of material through the hole. In any case the loss was negligible fraction of the total number of ions collected.

3.3. Determination of Ionization Efficiency

The goal of the dilution flask experiments was to determine the ionization efficiency of the PC. As soon as it became operational, measurements of the signal from a chlorobenzene injection were made. It became apparent that the logarithmic decrement of the signal current

43

was slightly different from the logarithmic decrement calculated for the volume dilution in the flask. The implication of this was that any attempt to define an instanteous efficiency as the ratio of ions produced per second (the signal current) to the number of molecules flowing through the reaction region per second would not be successful because the ratio changed constantly with time.

Based on the reasoning that the volumetric dilution rate might not be well known, so that instantaneous flow rates would be in error, it was decided to use the total number of ions collected to determine the ionization efficiency. The definition of ionization efficiency would then be the total number of ions collected divided by the number of molecules introduced.

Measurement of the total number of ions produced was done two ways. The first involved using the signal averager in the one-grid mode to measure the signal current at discrete points in time. The current generally exhibited an exponential decay, although at short times after the injection, deviations sometimes occurred. The integral of the current was then computed using simple numerical techniques; the exponential behavior made the integration relatively easy. The other method was to use the two grid mode, with an automatic zeroing circuit (Section 5.1); the signal was recorded continuously on the signal averager (at 4 seconds per channel), and the digital integration capability of the averager was used. The results from both methods agreed when compared. The two-grid method had the advantages of a continuous record for complete recording and considerable convenience, since it could operated unattended for the hour or more typically required for dilution down to the noise level.

44

The two grid method had the additional advantage of including accurately the initial response of the PC when the signal increased from zero to its maximum value over a period of several seconds to a few minutes. As shown in Reference 8, this buildup is due to a finite response time in the instrument (in this case the mixing volume of the reaction region), but by integrating over the entire dilution, there is no net effect on the number of ions collected.

Once the integral was obtained, the number of ions produced in the reaction region was calculated by dividing the number collected by the grid transmission factor and by the duty cycle of the ion pulse. This number was then divided by the number of molecules injected to determine the ionization efficiency.

3.4 Sample Preparation

Samples of the materials tested were injected as liquid solutions and as gaseous solutions. Chlorobenzene, o-dichlorobenzene, and o- and m-mononitrotoluene are liquids at room temperature and were handled in microliter syringes on a volumetric basis. Trinitro-toluene(2,4,6), dinitrotoluene(2,4), and p-mononitrotoluene are solids at room temperature and were dispensed by weight.

Because of the expected sensitivity of the PC, the solutions covered a concentration range from 10^{-3} molar to 10^{-8} molar for the substance of interest. The most concentrated solution was prepared first, and lower concentrations (in the ratio of ten to one per step) were obtained by serial dilutions.

The two solvents used in this work were methanol and benzene (Fisher Pesticide Grade), with benzene being used most often. The solutions

45

were made and stored in glass bottles with Teflon liners in the caps. Before use, the bottles were soaked in a cleaning solution of hydrogen peroxide, ammonium hydroxide, and distilled, deionized water in the ratios 1:1:8. This was followed by rinses of distilled water, acetone (Fisher Electronic Grade), and pesticide grade benzene. Some data were taken using solutions stored in bottles cleaned in this fashion, but when nitrogen carrier gas was used, a background ion peak (Cl^- or $(H_2O)OH^-$ appeared that was proportional to the amount of solvent injected. Since this could have arisen from the water or acetone rinses, a second bottle preparation procedure was used. The bottles were re-rinsed thoroughly with the benzene and then baked in an oven at least fifteen hours at 160°C. The pipettes used in making the solutions were also baked. Solutions in bottles cleaned in this way showed no background ion.

Considerable care was taken to avoid cross-contamination of the solutions. Repeated rinsing of the transferring syringes and pipettes with solvent was performed before handling a solution of different concentration. In addition, it was the practice to work with the most dilute solutions first and to ascend the concentration scale in order. This minimized the effect that any transfer of contaminants would have had.

Chlorobenzene and dichlorobenzene have vapor pressures at room temperature high enough to allow preparation of a gas phase sample. This was done for both, using the following procedures. An Ehrlenmeyer flask was fitted with a stem allowing flow through the flask, with two stopcocks in the arms. The flask also had a sidearm with a silicone rubber septum.

46

The flask was flushed continuously for almost an hour with dry nitrogen at a flow rate of about 400-500 cm^3 per minute. The valves were closed, isolating the flask, and a known quantity of chloro- or dichlorobenzene, on the order of one microliter, was then injected through the septum. A magnetic stirring bar in the flask allowed thorough mixing in a short time. With a flask volume of 551 cm^3 the amount of vapor was well below saturation, assuring complete vaporization of the sample.

Various amounts of sample, 0.1 to 5.0 cm^3 by volume, were then withdrawn through the septum in a gas tight syringe, and injected into the dilution flask. An inventory of the amounts withdrawn was maintained because of the fixed quantity available. Over a period of a week, there seemed to be little loss of sample from the flask, as determined by the ionization efficiency. Only in one case was the inventory in the flask low, an order of magnitude less than that calculated after a period of two or three months. Although there was probably some adsorption on the walls, it did not seem to be a problem in usual operation; the source of the major loss in this one case is not known.

3.5 Reduced Electric Field

The plasma chromatograph differs from the standard pulse mode operation of an electron capture detector in that the electric field is continuously applied. In a gas such as nitrogen, where there are no low energy molecular states available, the electrons can gain an energy much larger than thermal energy. The result is that the response of an electron capturing compound in the PC will differ from the response in an electron capture detector because of the lower concentration of thermal electrons in the PC.

47

The electric field can be reduced in the reaction region by changing the applied high voltage. However, in the present design this changes the field in the drift region as well, due to the fixed voltage divider network. If both grids are held open, the total current can be measured as a function of the applied electric field. The current is not a simple function of voltage, because the velocity of the electrons is also affected by the applied field. Recombination effects will reduce the current if the electrons are not separated from the positive ions by a strong field, and the onset of these effects can occur rapidly as a function of field.

A plot of the electron current as measured on the PC, the electron velocity (taken from Reference 9) and the electron velocity measured on the PC are shown in Figure 3.1. As can be seen, the current is not even monotonic. No quantitative explanations can be given for the curve, but there is a correlation between the sharp rise in current at $6 \cdot 10^{-2}$ volts/cm-Torr and the near zero slope of the velocity curve, indicative of a highly dissipative process at that field strength. The current was measured with the 10^8 and 10^{11} ohm resistors, with both grids continuously open, as a function of electric field. The electron velocity was measured by the difference in arrival times for the electron peak using each grid as the gating grid. In this way, the rise time of the preamplifier was eliminated and the short transit times of the electrons determined.

The change of mobility with changing electric field is inconvenient, both with respect to identification of peaks and to losses due to various sources which can occur in the drift region. It is desirable to maintain

48
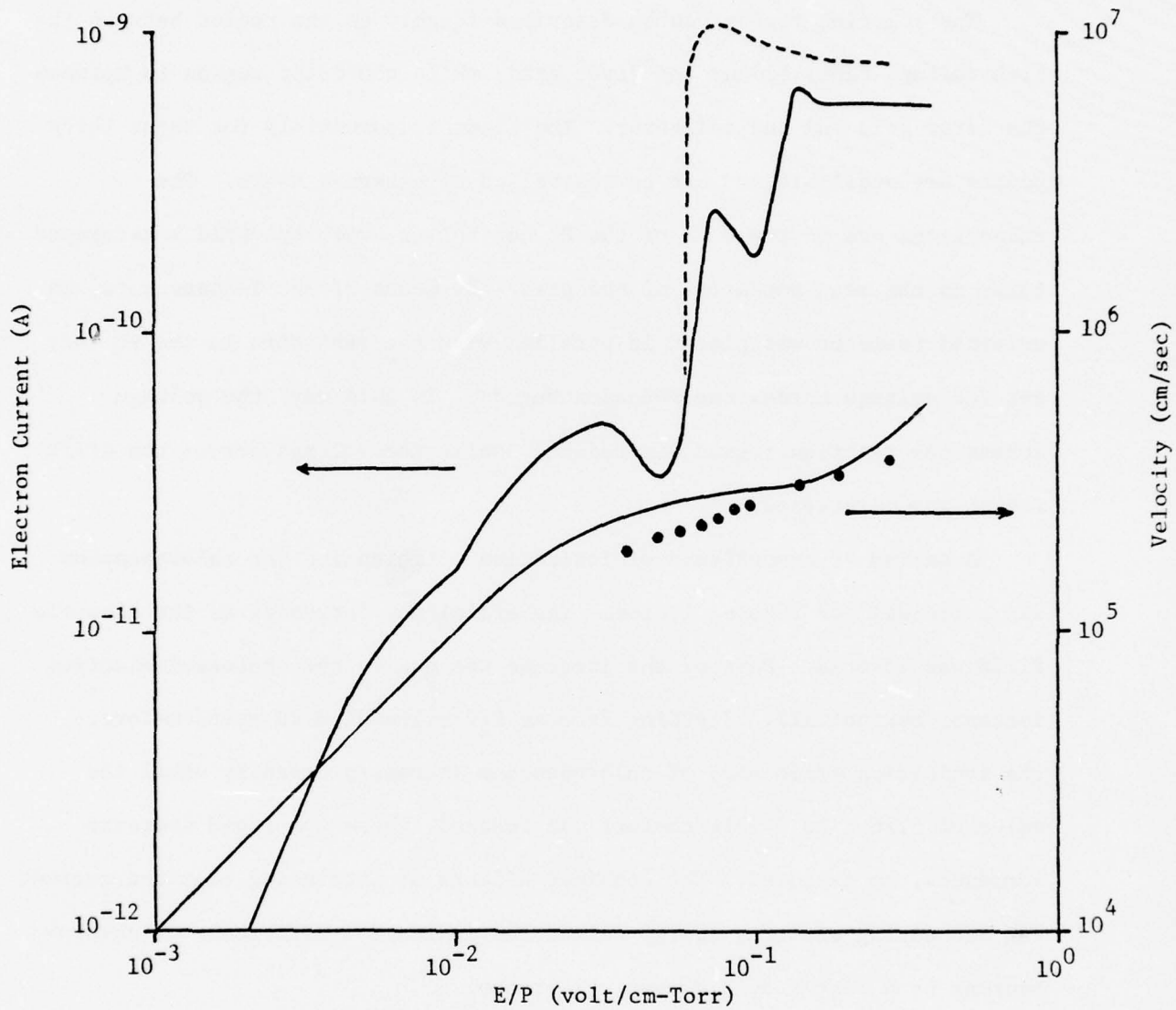
Figure 3.1. Electron current and velocity in nitrogen as a function of electric field. Dashed line is the current of a second Beta/VII instrument. Velocity curve is taken from Reference 9.

49

the drift field at its normal value while varying the field in the reaction region. This was fairly easy to accomplish to a first approximation.

The reaction region can be described roughly as the region between the high voltage repeller and the first grid, while the drift region is between the first grid and the collector. The electric potentials for these three points are available and can be controlled by external means. The connections are on the back of the PC controller, with the Grid 1 Reference taken as the mean potential of the grid. By means of BNC T-connectors, an external resistor was placed in parallel with the resistors in the PC that set the voltage across the reaction region. In this way, the voltage across the reaction region was reduced, while the voltage across the drift region was maintained.

A series of comparisons of ionization efficiencies for chlorobenzene was performed for reduced fields. The efficiency increased as the electric field was lowered. Part of the increase was due to the increased electron current, but not all. Starting from an E/P value of 0.28 volt/cm-Torr, the ionization efficiency of chlorobenzene increased steadily until the value of $5.26 \cdot 10^{-2}$ volt/cm-Torr was reached, where the rapid decrease commenced, as expected. The combined effects of increasing electron current and decreasing electron energy raised the ionization efficiency of chloro- benzene by a factor of 2.7 over this range.

The technique was not actively pursued, because the external resistor upset the action of the grid to some extent, allowing a higher leakage current. Until access to the internal dividers could be obtained directly, the technique was not further developed.

50

4.0 IONIZATION EFFICIENCIES

In this section, the measured ionization efficiencies (IE) for TNT, DNT, the MNT's, and chloro- and dichlorobenzene are presented and discussed. Many more experimental data were obtained than are included in the following subsections, but only the most reliable data are presented here. Corrections for flow rate, which are fairly small, are included in the following tables. The derivation and experimental verification of the correction are presented in Section 4.6.

The integrated ionization efficiency is defined by the ratio of ions generated to the number of molecules injected into the flask:

$$IE = n/N . \qquad\qquad (4.1)$$

The number of ions is equal to the total charge generated divided by the electron charge, since all the ions are assumed to be singly charged. The charge generated is equal to the integral of the collector current with correction factors applied to account for the differences between the collector current and the current in the reaction region. Specifically,

$$Q = \frac{1}{\alpha_1 \, \alpha_2 \, \alpha_3} \int_o^\infty I_c \; dt \qquad\qquad (4.2)$$

where I_c is the collector current. The three correction factors are discussed below. The first factor, α_1, is equal to the duty factor and applies only in the two grid mode where the signal current pulse is averaged over the full cycle between repetitions. For all the work reported here, $\alpha_1 = 8 \cdot 10^{-3}$. The second factor, α_2, is the grid transmission factor, which is 0.677 for

51

the optical transmission, or 0.439 for ionic transmission (as calculated in Appendix 4). The optical transmission factor was used extensively throughout this work. The ionic transmission factor is considered more realistic for describing the transmission losses, but it entails more uncertainties because little is known about the actual configuration of the aperture grid. Ionization efficiencies will be calculated both ways, and so long as the consistent factor is used for a given ionization efficiency, no problems will arise.

The last factor, α_3, represents the loss due to the second gate pulse being too narrow to pass the whole ion pulse through. It applies only to two-grid operation, and, in most circumstances in this work, it was just one.

The integrated ionization efficiency is, therefore,

$$IE = \frac{\int I_c \, dt}{\alpha_1 \, \alpha_2 \, \alpha_3 \, eN} \quad . \tag{4.3}$$

The nitrotoluenes exhibit at least two distinctive negative ion mobilities, depending on the ion molecule reactions that form them. In the presence of free electrons, they capture an electron to form a molecular anion. In the presence of other molecular ions, the nitrotoluenes can lose a proton to form a proton-abstracted ion. There is a difference in mass between the two types of ions of one a.m.u., but there are also apparently structure differences between the two since a one a.m.u. difference in mass is not sufficient to account for the observed mobility differences. The mobility of an ion, μ, is defined as the ratio of its drift velocity to the electric field:

$$\mu = \frac{v_d}{E} \quad . \tag{4.4}$$

52

The reduced mobility is defined as the measured mobility, calculated for standard STP conditions:

$$\mu_o = \mu \cdot \frac{P}{760} \cdot \frac{273}{T} , \qquad (4.5)$$

where the visits for P and T are Torr and kelvins. Although the reduced mobility does not represent an actual measurement at STP conditions, it does provide a convenient identification for ions without reference to the specific conditions of measurement.

For the nitrotoluenes, where the mass of the ions responsible for particular mobility peaks have been identified, the proton-abstracted anion has a higher reduced mobility than the molecular anion.

4.1 Trinitrotoluene

Trinitrotoluene exhibits three ion peaks at elevated temperatures with reduced mobilities of 1.59, 1.54, and 1.49 cm^2/volt-sec. The proton-abstracted anion has been identified as the 1.54 ion, and the molecular anion has the 1.49 mobility. The third peak may be a nitro-abstracted anion, but confirming plasma chromatograph-mass spectrometer evidence is lacking. The mobility spectra for TNT are shown in Figure 4.1.

In obtaining the IE's for each type of ion, the proton-abstracted ion had a much larger efficiency than the molecular ion. As a result, it was difficult to obtain the molecular anion alone in nitrogen carrier gas, even though there was an abundance of free electrons. Trace quantities of other molecular ions provided a source of ionization for the proton-abstracted ion. Consequently, the gate delay and width of the second grid had to be set very carefully to obtain only the molecular ion. There was some overlap of the ion peaks due to the characteristic spreading.

53
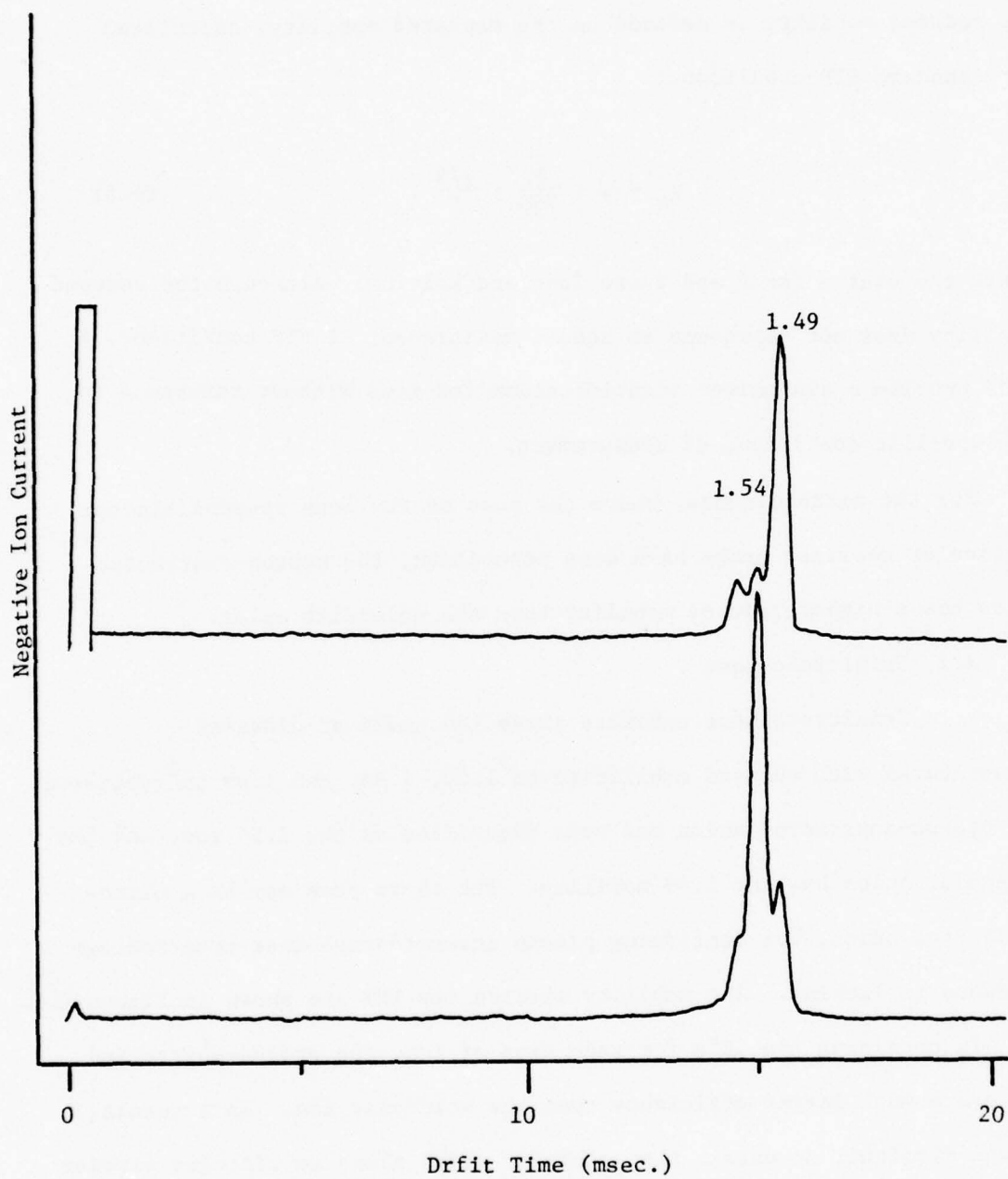
Figure 4.1. Mobility Spectrum of TNT. Upper trace is in nitrogen, lower trace is in air.

54

The two were separated by the standard technique of dropping a line to the baseline at the minimum between the peaks, assigning the whole area on either side of the line to the corresponding peak. There were no difficulties in measuring IE for the proton-abstracted anion, since there were no free electrons available for capture with the air carrier gas.

In Section 4.6, the results of measurements at various flow rates will be presented. As a result of these measurements, two kinds of corrections can or need to be applied to the TNT ionization efficiencies. The first is for convenience: reducing all the data to a common flow rate. Although nominally the flow rate was 50 cm^3/min at room temperature, there were accidental and deliberate deviations from that value. Since both theory and measurement indicate that the integrated ionization efficiency varies inversely with the flow rate, the correction to the standard 50 cm^3/min is straightforward. The second correction is an empirical one, applied only to the electron-capture data; it is a correction, dependent on flow rate, for an apparent loss of injected sample. Both corrections will be discussed in detail in Section 4.6. The ionization efficiencies presented in Table 4.1 and in Figure 4.2 are the fully corrected values.

Some of the features of the data presented here deserve comment. First, the lower ionization efficiency for the electron capture process is due more to the nature of the reactant ions than to the reaction itself. The concentration of free electrons is much lower than the concentration of other ions producing the same total current because the electron drift velocity is about two thousand times higher.

55
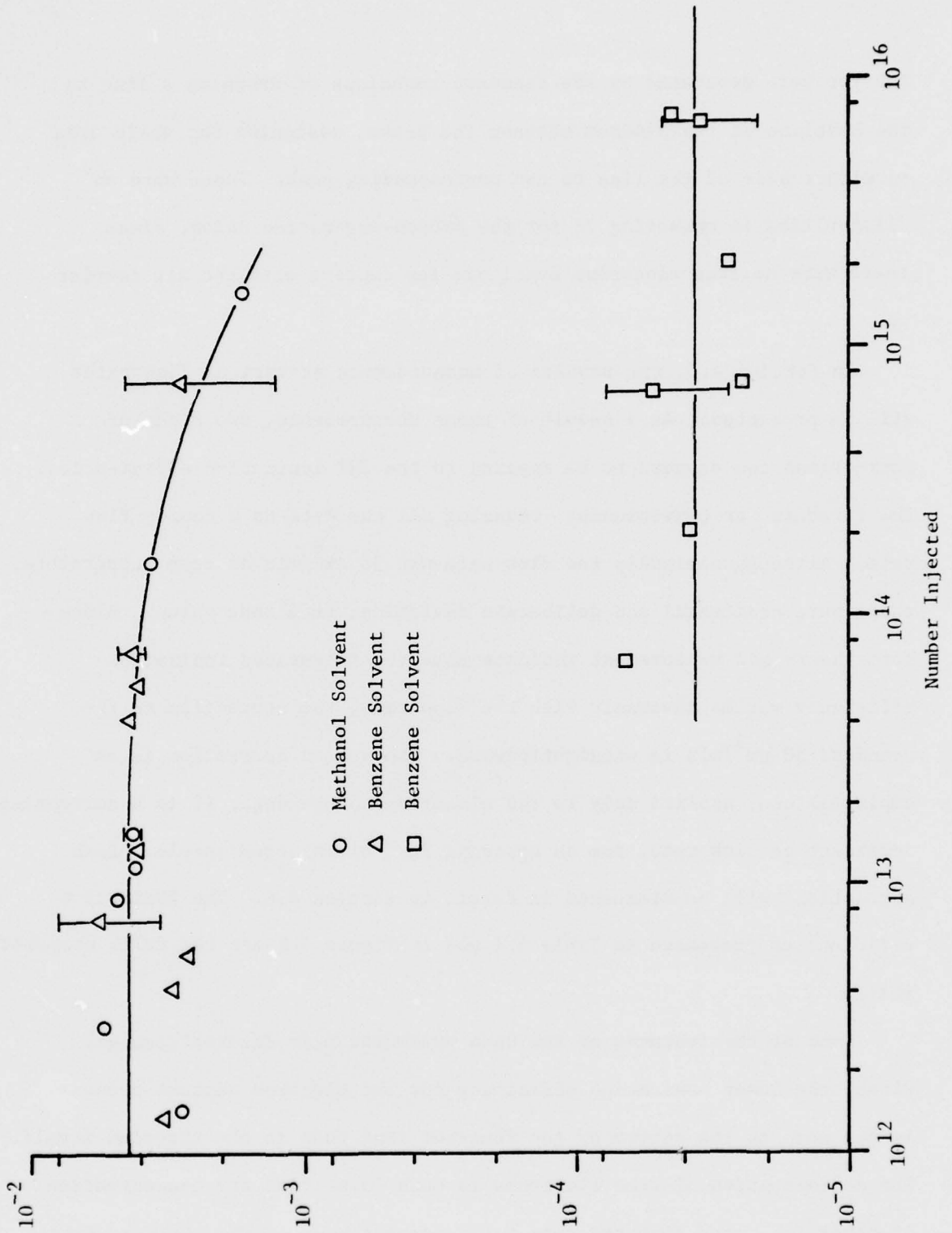
Figure 4.2. Ionization efficiency for TNT. Upper curve is in air, proton-abstracted ion; lower curve is in nitrogen, electron-capture ion.

Table 4.1 <u>TNT</u>

Proton-abstracted (Air Carrier) 200°C

N_{TNT}	$\dot{F}$ (cm^3/min @ 20°C)	Runs Averaged	n	n_T (Flow Corrected)	IE (Optical)
Benzene Solvent					
1.37E12	49	1	4.61E9	4.52E9	3.30E-3
4.11E12	49	1	1.29E10	1.26E10	3.08E-3
5.47E12	51	1	1.45E10	1.48E10	2.70E-3
7.29E12	58.6	8	3.49E10	4.13($\pm$1.65)E10	5.67($\pm$2.26)E-3
1.37E12	58	1	4.81E10	5.58E10	4.07E-3
4.11E13	58	1	1.56E11	1.81E11	4.40E-3
5.47E13	58	1	1.94E11	2.25E11	4.11E-3
7.29E13	57.6	5	2.61E11	3.14($\pm$.36)E11	4.31($\pm$.49)E-3
7.29E14	55	2	1.87E12	2.10($\pm$1.19)E12	2.88($\pm$1.63)E-3
Methanol Solvent					
1.49E12	50.5	1	4.26E9	4.30E9	2.89E-3
2.98E12	50.5	1	1.63E10	1.65E10	5.52E-3
8.94E12	50	1	4.42E10	4.42E10	4.94E-3
1.19E13	49	1	5.11E10	5.01E10	4.21E-3
1.59E13	51	2	6.70E10	6.84($\pm$.44)E10	4.30($\pm$.28)E-3
1.59E14	50	1	5.85E11	5.85E11	3.68E-3
1.59E15	50	1	2.68E12	2.68E12	1.69E-3

$$IE_{avg} = 4.25E-3$$

Table 4.1   (Continued)

Electron-captured (Nitrogen Carrier) 200°C

		Benzene Solvent				
6.78E13	52		1	2.08E9	4.43E9	6.53E-5
2.03E14	50		1	3.68E9	7.70E9	3.79E-5
6.78E14	50		2	1.67E10	3.49($\pm$1.65)E10	5.15($\pm$2.43)E-5
7.29E14	50		1	8.51E9	1.78E10	2.44E-5
2.03E15	50		1	2.64E10	5.52E10	2.72E-5
6.78E15	55.3		3	1.03E11	2.31($\pm$.86)E11	3.41($\pm$1.27)E-5
7.29E15	50		1	1.53E11	3.20E11	4.39E-5

$$IE_{avg} = 3.65E-5$$

58

Second, the range of sample sizes that produce a linear response is more than two decades. At the lowest sample sizes, the signal-to-noise problem produces greater and greater uncertainties in the calculation of ionization efficiency, while the largest injections saturate the reactant ion current for part of the dilution run. The saturation is "soft" in the sense that further increases in sample size produce more and more ions, but the IE decreases roughly as $\ln N/N$. Saturation was observed in the proton abstraction measurements, but not in the electron capture measurements because of the high concentration of sample molecules that would have been required.

Third, there is no significant difference between the use of benzene and methanol as a solvent in proton abstraction and no significant trends due to the amount of benzene solvent injected in the electron capture measurements. The amounts of solvent injected in the proton abstraction measurements were 10.7 microliters per run, for both benzene and methanol. In the electron capture measurements, the amount of benzene injected ranged from 10.7 microliters down to 0.1 microliter without exhibiting a significant variation.

Fourth, the average ionization efficiency for each process, indicated by the horizontal line drawn through the points, was calculated by dividing the total number of ions collected for all runs not showing saturation effects by the total number of molecules injected for all those runs. This weights the ionization efficiency toward the high concentration runs and avoids the relatively large variations that occur when the signal is close to the noise level in the low concentration runs. Other weighting schemes could be used, but this one is easy to use and gives the greatest weight to the most reliable runs.

59

4.2 Dinitrotoluene

Dinitrotoluene also exhibits a proton-abstracted anion and a molecular anion, with reduced mobilities of 1.67 and 1.61 cm^2/volt/sec, respectively. The proton-abstracted ion appears in the presence of oxygen ions, chloride ions, or even high concentrations of DNT itself.

The difference in ionization efficiencies for the two types of ion is so large that it proved impossible to obtain the molecular anion by itself, even in a very clean system. Again, careful setting of the second gate pulse allowed the two peaks to be measured separately. The mobility spectra for DNT are shown in Figure 4.3.

Corrections similar to those applied to the TNT data have been applied to the DNT ionization efficiencies. Only a correction to a standard flow rate of 50 cm^3/min was applied to the proton-abstraction data while the additional correction for loss of samples was applied to the electron capture data. The corrections are justified in Section 4.6. The data are presented in Tables 4.2 and Figure 4.4.

The proton abstraction data cover a range from just inside the linear response region to well into the saturated response of the PC. This behavior can be described in terms similar to those used in the linearization of electron capture detectors (Reference 10). For the electron capture detector,

$$\frac{I_b - I_e}{I_e} = kN, \tag{4.6}$$

where I_b is the standing current in the absence of sample, I_e is the current measured with the sample present, N is the number of sample molecules in the detector, and k is a constant. In the PC, the standing

60
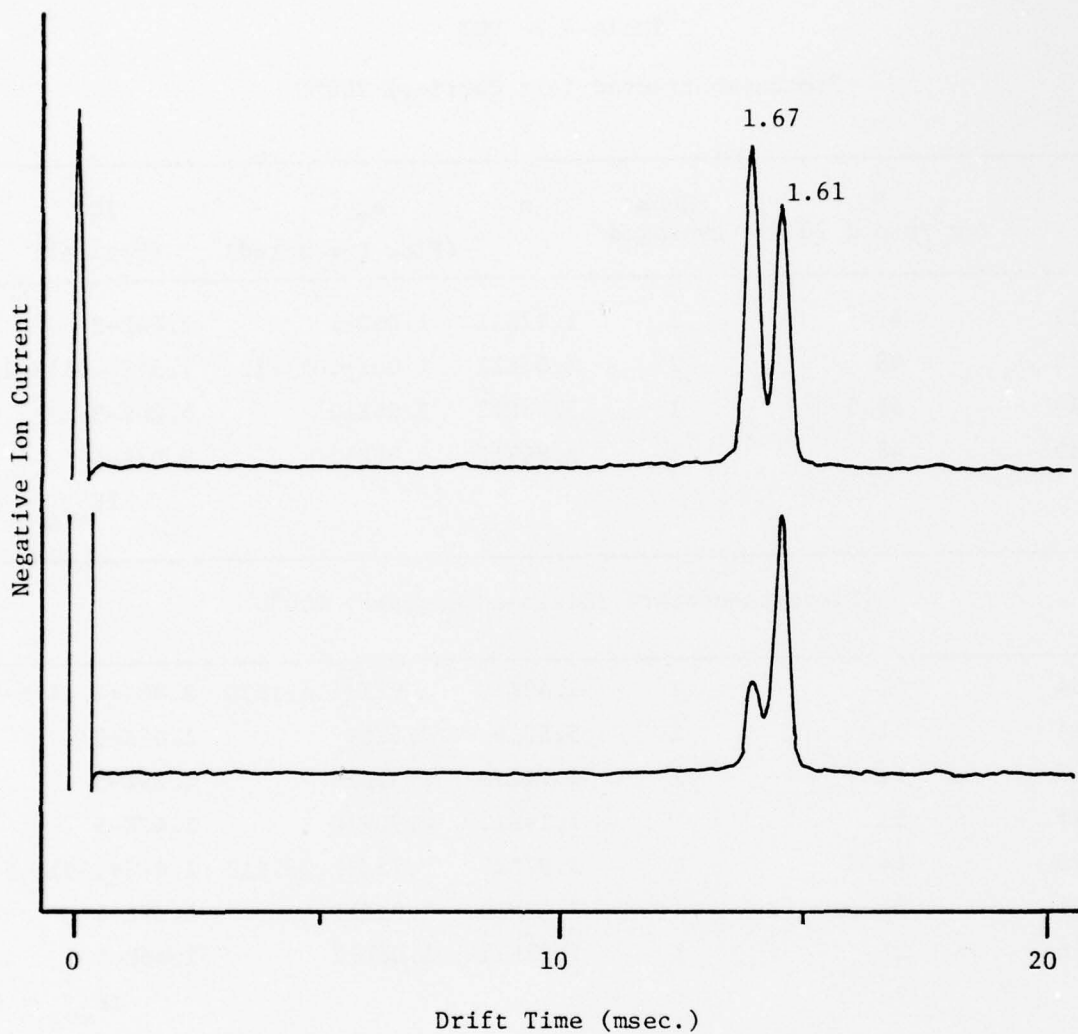
Figure 4.3.   Mobility Spectrum of DNT.   Upper curve is for a high
concentration of DNT in nitrogen; lower curve is for
a low concentration of DNT in nitrogen.

61

Table 4.2 <u>DNT</u>

Proton-abstracted (Air Carrier) 200°C

N_{DNT}	$\overset{\bullet}{F}$ (cm^3/min @ 20°C)	Runs Averaged	n	n_T (Flow Corrected)	IE (Optical)
7.29E12	47	1	1.12E11	1.05E11	1.44E-2
7.29E13	48	2	1.05E12	1.00($\pm$.01)E12	1.37($\pm$.01)E-2
7.29E14	48.5	1	3.76E12	3.65E12	5.00E-3
7.29E15	48	1	6.86E12	6.59E12	9.03E-4
					IE_{avg} = 1.38E-2

Electron-capture (Nitrogen Carrier) 200°C

N_{DNT}	$\overset{\bullet}{F}$ (cm^3/min @ 20°C)	Runs Averaged	n	n_T (Flow Corrected)	IE (Optical)
6.78E14	51	2	1.40E10	1.92($\pm$1.45)E10	2.80($\pm$2.14)E-5
7.29E14	51	1	5.53E9	7.52E9	1.03E-5
1.81E15	51	1	1.71E10	2.33E10	1.29E-5
2.03E15	51		2.19E10	2.98E10	1.47E-5
6.78E15	64.5	2	5.97E10	9.75($\pm$2.03)E10	1.44($\pm$.30)E-5
7.29E15	51	1	7.42E10	1.01E11	1.39E-5
7.29E16	51	1	7.78E11	1.06E12	1.46E-5
					IE_{avg} = 1.46E-5

62
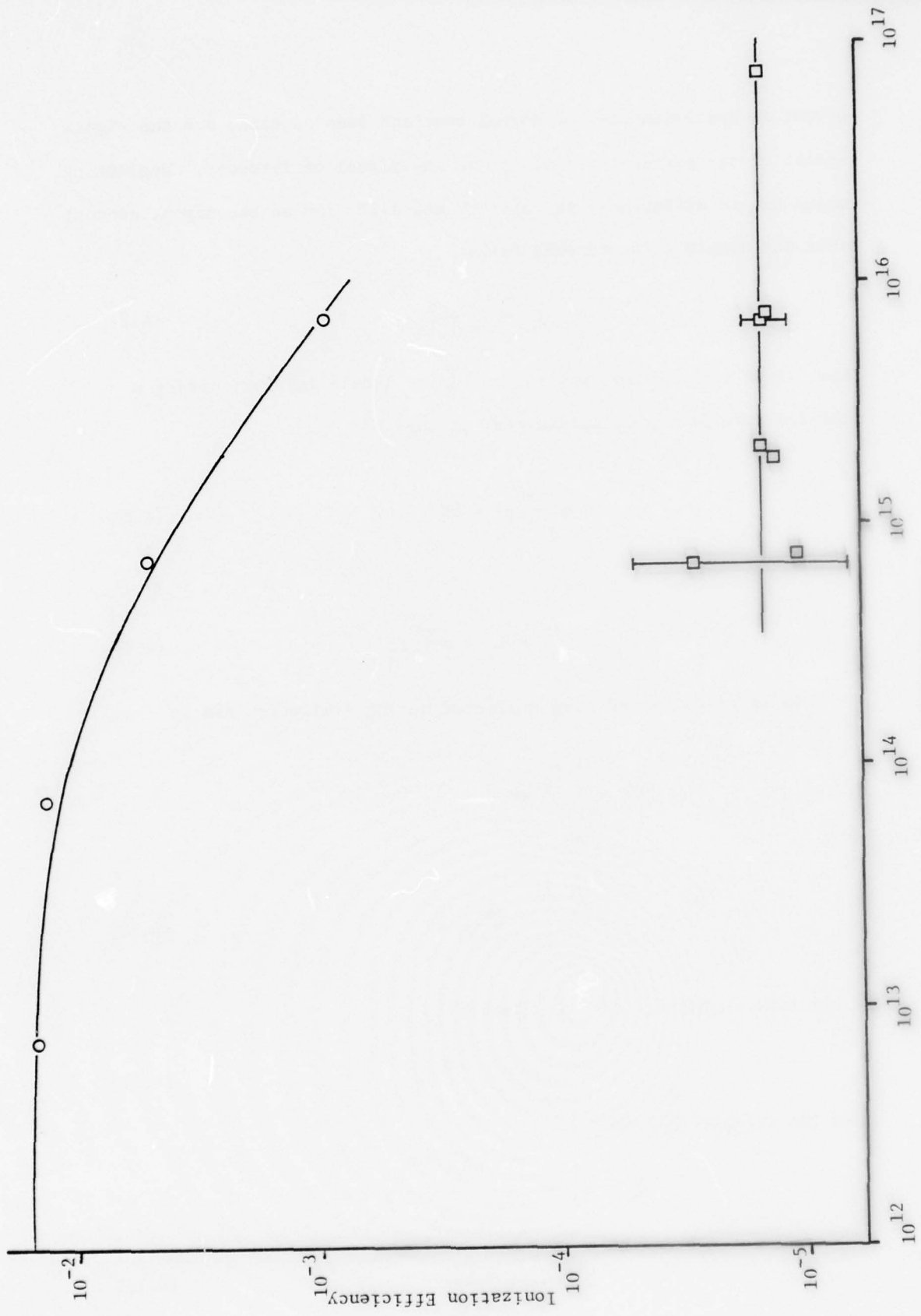
Figure 4.4. Ionization efficiency for DNT. Upper curve is in air, proton-abstracted ion; lower curve is in nitrogen, electron-capture ion.

63

current is approximately the normal reactant ions current, and the signal current of the particular ion, I_S, is the signal of interest. Neglecting losses due to differences in velocity and diffusion as the signal current rises the reactant ion current falls:

$$I_b = I_e + I_s \ .$$ (4.7)

Then, since the reactant ion current is of little interest during a dilution run, it can be eliminated, giving:

$$\frac{I_s}{I_b - I_s} = kN \ .$$ (4.8)

Or, solving for I_s,

$$I_s = I_b \cdot \frac{kN}{1 + kN} \ .$$ (4.9)

The total number of ions collected during a dilution run is

$$Q/e = \int_0^\infty \frac{I_s}{e} \, dt$$

$$= \frac{I_b}{e} \int_0^\infty \frac{kN}{1 + kN} \, dt \ .$$ (4.10)

If the time dependence of N is given by

$$N = N_o \, e^{-\alpha t} \ ,$$ (4.11)

then the integral becomes

$$Q_e = I_b/e \int_0^\infty \frac{kN_o e^{-\alpha t}}{1 + kN_o e^{-\alpha t}} \, dt$$

$$= \frac{I_b}{\alpha e} \ln (1 + kN_o) \ .$$ (4.12)

64

The constant k can be evaluated at values of $kN_o \ll 1$, where the response of the PC is linear:

$$Q/e = IE_o N_o \simeq \frac{I_b}{\alpha e} kN_o \qquad (4.13)$$

or

$$k = \frac{IE_o}{I_b/\alpha e} \qquad (4.14)$$

where IE_o is the limiting ionization efficiency as $N_o \to o$.

The quantity $I_b/\alpha e$ is the number of ions that would be collected if the signal current started at I_b and experienced an exponential decay with constant α; it depends upon flow rate and is given the name N_b. Then, the final expression for ionization efficiency as a function of N_o is:

$$IE(N_o) = \frac{N_b}{N_o} \ell n \left(1 + IE_o \frac{N_o}{N_b}\right) . \qquad (4.15)$$

This describes the limiting case as $N_o \to o$, and as N_o becomes much larger than N_b, describes the falling off of IE as $\ell n\, N_o/N_o$, which was mentioned earlier.

The dotted line in Figure 4.4 was calculated from Equation 4.13 using the following values:

$$IE_o = 1.50\ E\text{-}2$$
$$N_b = 1.60\ E12$$
$$I_b = 7.2\ E\text{-}10A$$
$$\dot{F} = 50\ cm^3/min$$

The fit is by no means perfect, but then the model does not allow for the presence of large numbers of sample molecules having an effect on

65

the ionization efficiency. Furthermore, although Equation 4.13 predicts a $1/\dot{F}$ dependence in the linear region of response, at saturation levels, the flow rate dependence is modified. The values shown have only been corrected for the $1/\dot{F}$ part of the dependence.

4.3 Mononitrotoluenes

The three isomers of MNT would be expected to exhibit the same proton-abstraction and electron-capturing properties that the higher nitrotoluenes do. In this work, double peaks were obtained for all three isomers in nitrogen carrier gas, suggesting that the same processes occur. However, PC-MS data only support the presence of the electron-capture peak in nitrogen, with a reduced mobility of 1.74 cm^2/volt-sec/for all three isomers. Where the MNT's are measured with zero-air carrier, extensive fragmentation of the molecules results, and no attempt was made to measure the ionization efficiencies. The spectra for selected isomers and conditions are shown in Figure 4.5.

There was no indication that a loss of sample occurred with the MNT's, and only a correction for the $1/\dot{F}$ dependence is made in the following table. A member of different amounts of solvent, ranging from 0.1 microliter to 10.6 microliters, were used in the m-MNT data. There was a slight trend toward higher IE when the amount of solvent was reduced. The effect could be within the experimental scatter, however, and time limitations prevented further measurements to ascertain the effect.

The ionization efficiencies for o-, m-, and p-MNT are presented in Table 4.3 and in Figure 4.6. At the highest concentrations, saturation effects should be slightly evident, but the scatter in the data obscures

66
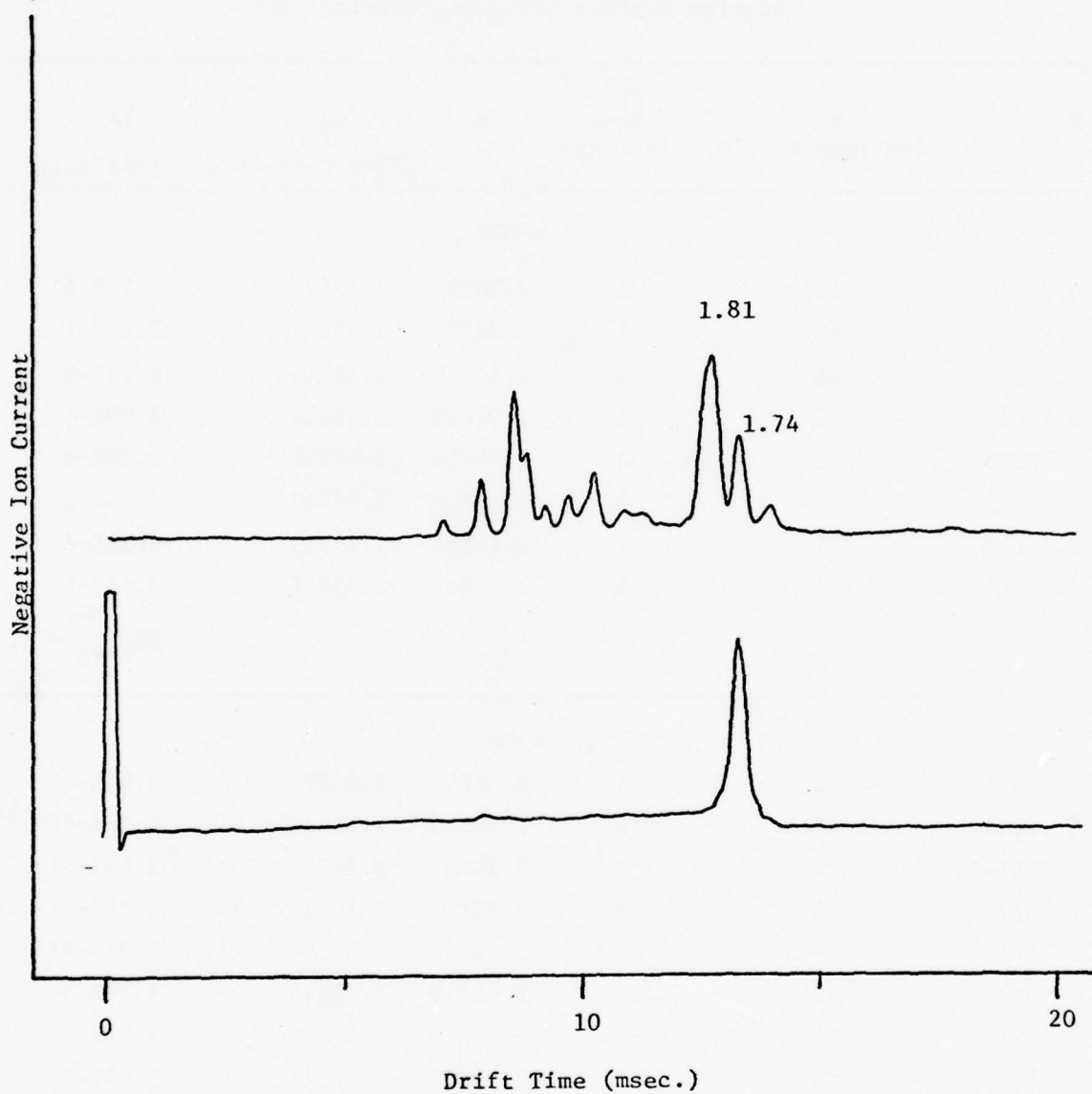
Figure 4.5. Mobility Spectra of MNT. Upper case is p-MNT in air; lower curve is o-MNT in nitrogen.

Table 4.3 MNT

Electron-capture (Nitrogen carrier) 200°C

N_{MNT}	$\dot{F}$ (cm^3/min @ 20°C)	Runs Averaged	n	n_T (Flow Corrected)	IE (Optical)
			o-MNT		
6.78E14	51	1	2.76E9	2.82E9	4.15E-6
7.79E14	51	1	2.34E9	2.39E9	3.27E-6
2.03E15	51	1	1.10E10	1.12E10	5.53E-6
2.74E15	51	1	1.07E10	1.09E10	3.98E-6
6.78E15	51	1	3.59E10	3.66E10	5.40E-6
7.29E15	51	1	2.69E10	2.74E10	3.76E-6
2.74E16	51	1	1.13E11	1.15E11	4.21E-6
7.29E16	51	1	2.75E11	2.81E11	3.85E-6
					IE_{0avg} = 4.31E-6
			m-MNT		
2.74E14	51	1	2.58E9	2.63E9	9.60E-6
6.78E14	49.5	4	1.09E10	1.07E10($\pm$.43)	1.58E-6($\pm$.63)
7.29E14	51	2	8.28E9	8.44E9($\pm$.30)	1.16E-5($\pm$.04)
1.36E15	48	2	2.25E10	2.16E10($\pm$.40)	1.59E-5($\pm$.29)
2.74E15	49.5	2	3.44E10	3.39E10($\pm$.14)	1.24E-5($\pm$.05)
6.78E15	48	1	9.02E10	8.66E10	1.28E-5
7.29E15	51	1	7.74E10	7.89E10	1.08E-5
2.74E16	48	1	3.01E11	2.89E11	1.05E-5
7.29E16	48	1	7.30E11	7.01E11	9.61E-6
					IE_{0avg} = 1.20E-5

Table 4.3 (Continued)

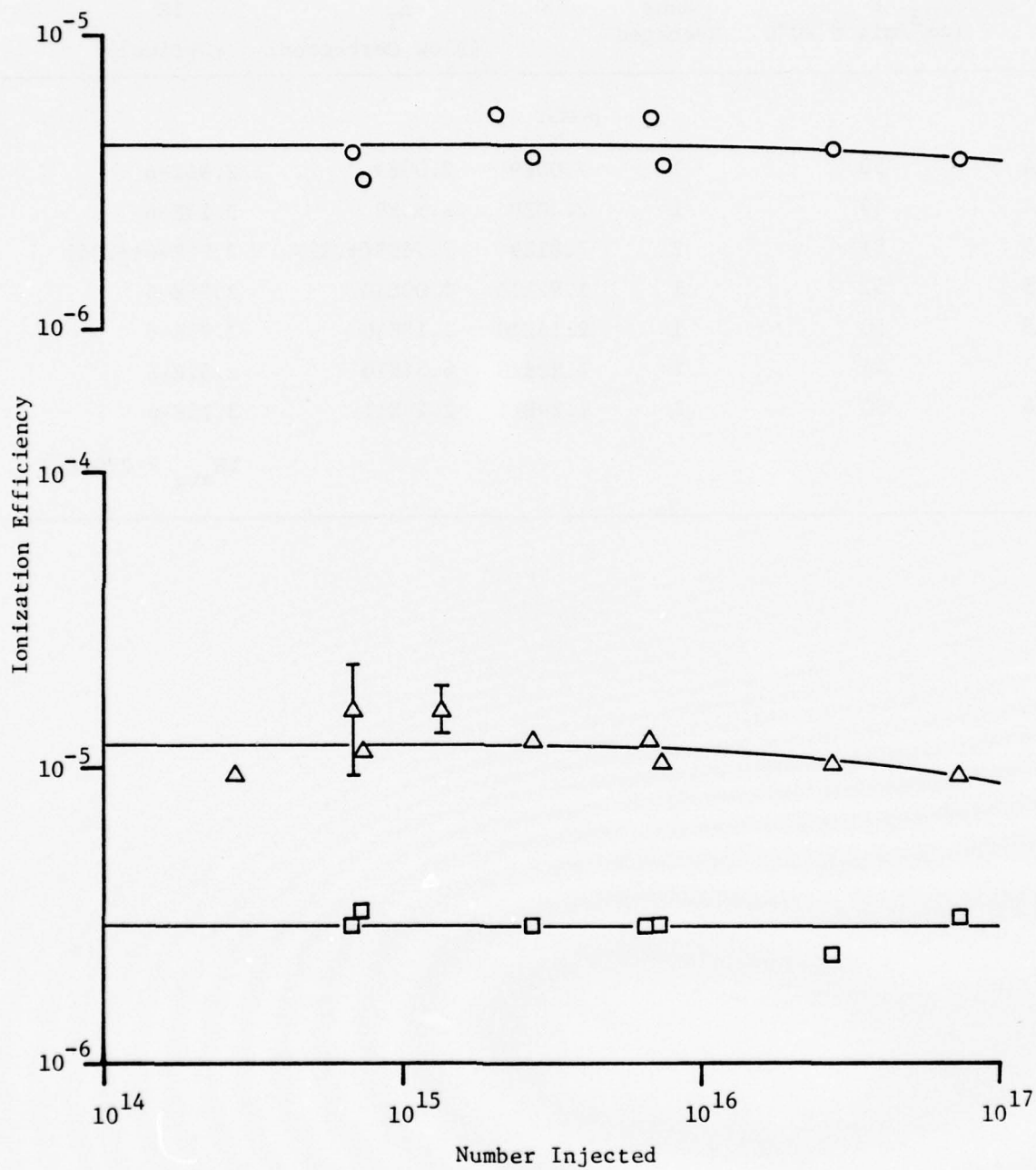| N_{MNT}	$\dot{F}$ (cm^3/min @ 20°C)	Runs Averaged	n	n_T (Flow Corrected)	IE (Optical)
			p-MNT		
6.78E14	50	1	2.00E9	2.00E9	2.96E-6
7.29E14	49	1	2.40E9	2.35E9	3.23E-6
2.74E15	51	2	7.81E9	7.96E9($\pm$.12)	2.92E-6($\pm$.04)
6.78E15	52	1	1.92E10	2.00E10	2.95E-6
7.29E15	50	1	2.15E10	2.15E10	2.95E-6
2.74E16	44	1	7.22E10	6.35E10	2.32E-6
7.29E16	50	1	2.29E11	2.29E11	3.15E-6
					IE_{avg} = 2.92E-6

69

Figure 4.6. Ionization Efficiency for MNT in nitrogen. Circles are o-MNT; triangles are m-MNT; and squares are p-MNT.

70

them to some extent. Values of IE_o in Equation 4.13 were calculated for o-MNT and m-MNT, assuming $N_b = 1.60 \cdot 10^{12}$. These values are in Table 4.3 and seem somewhat more representative of the data than simple averages do. There was not enough indication of saturation for the p-MNT data to make such a calculation necessary.

4.4 Chlorobenzene

The negative ionization mobility spectrum of chlorobenzene is the Cl^- ion with reduced mobility of 2.94 cm^2/volt-second. The molecule is notoriously adsorptive, and a great number of experimental difficulties encountered in measuring its ionization efficiency were blamed on this property.

When early dilution runs were made with chlorobenzene, the number of ions collected each time was nearly independent of the concentration injected, for a fixed amount of solvent. However, the number collected was in *proportion to the amount of solvent* in each injection. This points to three possibilities: the solvent was contaminated with a chloride ion, the solvent was displacing adsorbed molecules from the walls of the flask, or the solvent had a dominant effect on the ionization of the chloro-benzene. The first explanation is considered unlikely because of the care taken to prevent contamination, the guaranteed purity of the benzene (Fisher Pesticide Grade), and because with a very clean dilution flask, the solvent by itself produced no chloride ions. The other two explanations may be equally likely. Chlorobenzene exhibits an ion resonance at electron energies of 0.86 eV, in which an energetic electron is thermalized. (Reference 11). Whether the chlorobenzene dissociates at this energy, or whether the thermalized electron is captured, leading to dissociation, is unclear. In either case, the benzene molecule, which has a resonance

71

at 1.4 eV, would increase the number of thermal electrons available for ionizing the chlorobenzene. On the other hand, the scrubbing hypothesis would be equally satisfactory for explaining the observed results.

The intrinsic ionization efficiency of the chlorobenzene molecule was obtained by introducing large enough quantities to override the effects of the background ion. Fortunately, there was a region of sample sizes in which the background was negligible, but for which the saturation of the instrument was not reached. This allowed the ionization efficiency to be determined in spite of the background current.

Because of the background, there is no reliable way to calculate ionization efficiencies for those runs where the background was greater than the signal. Therefore only the number of ions generated in each run is tabulated in Table 4.4. Both gas-phase samples and liquid phase samples were used and are tabulated separately. The number of solvent molecules is an important parameter in the background ion current and is included with each run. The correction for the $1/\dot{F}$ dependence is included in the total ions generated for each run. There was no evidence of loss of material for the chlorobenzene data; therefore, no correction for this is applied.

Equation 4.13 can be changed to give the number of ions collected, and a background ion current accounted for in the following equation:

$$N_i = N_n \, \ln \left(1 + IE_o \frac{N_o}{N_b}\right) + N_S \,, \qquad (4.16)$$

where N_i is the number of ions generated and N_S is the number of background ions for the run, dependent on the amount of solvent. The equation can

72

Table 4.4 Chlorobenzene

Benzene Solvent (Nitrogen Carrier) 200°C

$N_{C\ell}$	Amount Solvent (microliter)	$\dot{F}$ (cm^3/min)	Runs Averaged	n	n_T (Flow Corrected)
1.12E12	16.4	61	4	6.53E10	7.97E10($\pm$.70)
1.12E14	16.4	98.7	1	6.42E10	1.27E11
8.10E11	10.6	47	1	6.16E10	5.84E10
8.10E12	10.6	47	1	7.17E10	6.80E10
3.95E13	10.6	47	1	7.87E10	7.46E10
8.10E13	10.6	47	2	7.73E10	7.33E10($\pm$.19)
8.47E13	10.6	48	1	7.98E10	7.66E10
7.80E13	10.6	61	1	8.42E10	1.03E11
1.52E14	10.6	47	1	5.77E10	5.47E10
2.43E14	10.6	49	1	5.37E10	5.26E10
7.29E14	10.6	49	1	6.55E10	6.42E10
2.43E15	10.6	48	1	6.62E10	6.41E10
7.29E15	10.6	49	1	8.87E10	8.76E10
7.29E16	10.6	51	1	5.63E11	5.74E11
2.05E17	10.6	50	1	1.70E12	1.70E12
7.29E17	10.6	50	1	3.52E12	3.52E12
8.48E13	3.6	54	1	1.83E10	1.99E10
2.54E14	3.6	49	1	2.24E10	2.20E10
8.48E14	3.6	48	1	2.47E10	2.39E10
3.96E13	1.6	48	1	9.49E9	9.11E9
1.19E14	1.6	49	1	9.58E9	9.39E9
3.96E14	1.6	48	1	1.25E10	1.21E10
1.19E15	1.6	48	2	2.03E10	1.97E10($\pm$.25)
Gas Phase (Nitrogen Carrier)					
1.07E15		51	1	1.85E10	1.89E10
3.02E15		51	1	4.03E10	4.11E10
1.07E16		51	3	1.30E11	1.32E11($\pm$.11)
3.19E16		51	1	3.20E11	3.26E11
5.26E16		50.5	2	4.36E11	4.40E11

Table 4.4 Chlorobenzene (Continued)

$N_{C\ell}$	Amount Solvent (microliter)	$\dot{F}$ (cm^3/min)	Runs Averaged	n	n_T (Flow Corrected)
Gas Phase (Nitrogen Carrier) (Continued)					
1.07 E17		51	1	1.20E12	1.22E12
2.08E17		50	1	1.42E12	1.42E12
2.63E17		51	1	2.17	2.21E12
2.78E18		51	1	6.09E12	6.21E12

be inverted easily to solve for IE_o, given the number of ions collected and the number injected for each run. The IE_o for each data point was calculated for several values of N_b and N_S, and the most self-consistent set of values was averaged. This set of values, with no claim that it is the "best" set, is presented in Table 4.5 and the data and fitted curves are in Figure 4.7.

Table 4.5   Fitted Values for Chlorobenzene

$$IE_o \text{ (avg)} = 1.17 \ (\pm.40) \ E\text{-}5$$

$$N_b = 2 \ E12$$

$$I_b = 7.83 \ E\text{-}10 \ A.$$

$$N_S \ (1.64 \ \mu\ell) = 8.51 \ E10$$

$$N_S \ (10.6 \ \mu\ell) = 5.50 \ E10$$

$$N_S \ (3.6 \ \mu\ell) = 1.87 \ E10$$

$$N_S \ (1.6 \ \mu\ell) = 8.30 \ E9$$

$$N_S \ (\text{gas phase}) = 0.0$$

The data is fitted reasonably well, with the most serious deviations being in the background region. Since the measurements were taken over a period of several months, it is not unusual to find variations in the background current taking place. At the lowest concentrations, the gas phase data deviate from the expected straight line corresponding to IE_o. This indicates that the chlorobenzene itself affects the background level somewhat and that some constant greater than zero should have been used for the background. Since no measurements of the background were made during the course of the gas phase runs, a zero value for the background was the best estimate that could be made.

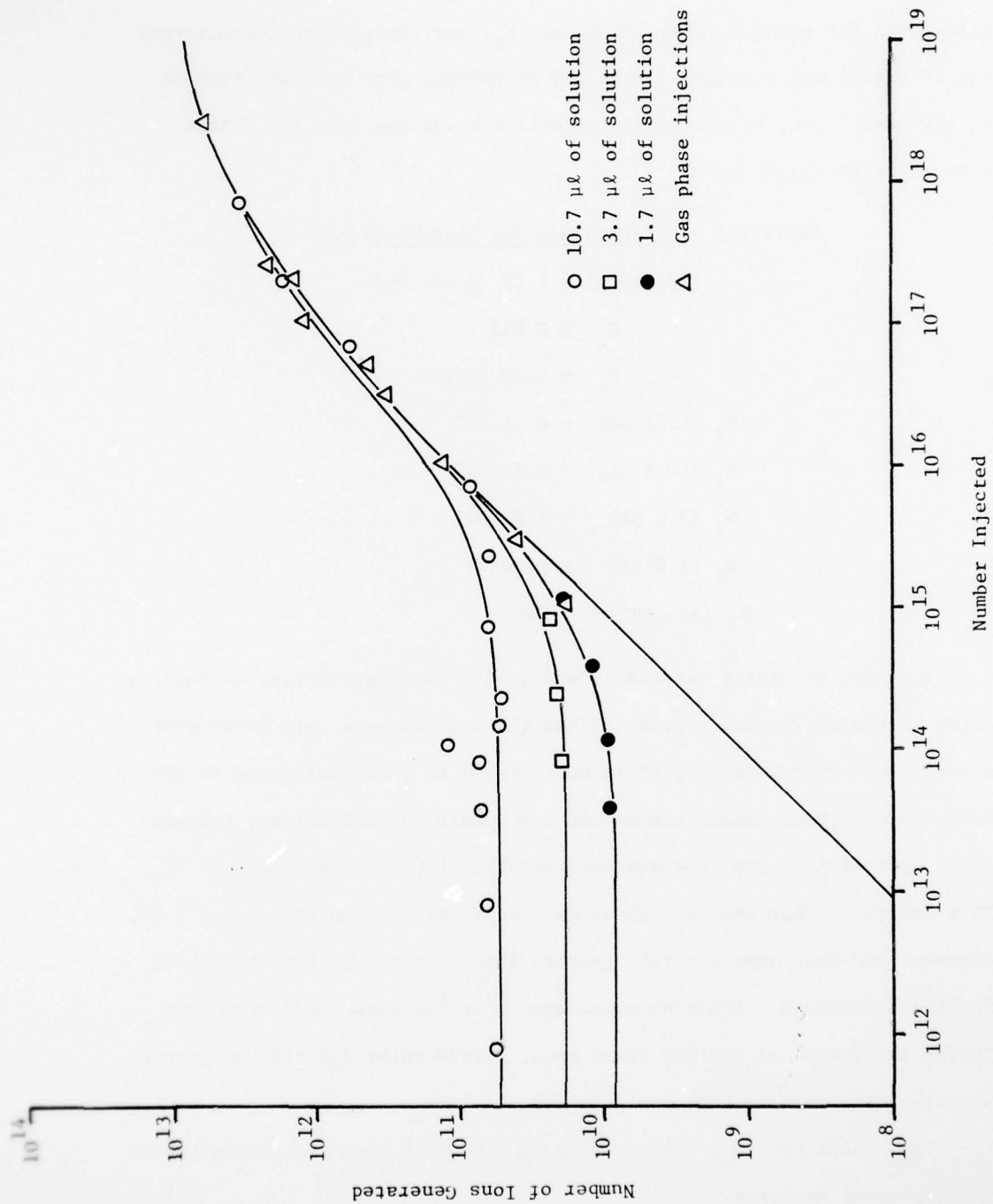This value for IE_o, $1.17 \cdot 10^{-5}$, is the value used for chlorobenzene in subsequent analyses.

Figure 4.7.   Ionization of Chlorobenzene.

○ 10.7 μℓ of solution
□ 3.7 μℓ of solution
● 1.7 μℓ of solution
△ Gas phase injections

Number Injected

Number of Ions Generated

76

4.5 Dichlorobenzene

Measurements were begun on o-dichlorobenzene with the intention of verifying the effects of electron energy spectrum first encountered with chlorobenzene. Dichlorobenzene has a resonance at 0.4 eV, considerably lower than chlorobenzene (Reference 11). Because of this, there should be a greater number of electrons available in the appropriate energy range to ionize the dichlorobenzene.

For a given amount of dichlorobenzene, a greater number of ions was indeed collected than for the same amount of chlorobenzene. However, the situation was complicated by the presence of the chlorobenzene background. Since both compounds produced only Cl^- ions, there was no way to distinguish the source of the ions. Moreover, dichlorobenzene could possibly scrub chlorobenzene from the walls more effectively than benzene, or could thermalize electrons more effectively than benzene, with the net result being that only chlorobenzene-derived ions were collected. There was no way to distinguish between possible sources.

Adding benzene solvent to the problem increased the difficulty of sorting out the various effects. Consequently, gas phase measurements were attempted at high concentrations in an effort to swamp out the background. Unfortunately, there was no clear demarcation between the background region and the saturation region. The data are presented in Table 4.6 for gas phase data and for two very low concentration benzene solutions in which the concentration of dichlorobenzene was so low that we believe solvent effects were the main source of background. By subtracting the ions produced by benzene alone from the ions produced by benzene and dichlorobenzene together, we

77

have a measure of the background due to the dichlorobenzene at low
concentrations.

The $1/\dot{F}$ correction for flow dependence has been included in the
total ions collected.

Table 4.6

o-Dichlorobenzene (Nitrogen Carrier) 200°C

N_{Cl}	$\dot{F}$ (cm^3/min @ 20°C)	Runs Averaged	n	n_T (Flow Corrected)
2.19E11	48	2	1.80E11	1.73E11($\pm$.05)
6.56	48	2	1.99E11	1.91E11($\pm$.11)
1.55E12	48	1	1.82E11	1.75E11
8.62E12	48	1	1.48E11	1.42E11
4.31E13	48	1	1.87E11	1.80E11
4.31E14	48	1	4.48E11	4.30E11
9.68E14	48	1	7.92E11	7.60E11
2.91E15	48	1	1.24E12	1.19E12
9.69E15	48	1	2.36E12	2.27E12

The data were fitted in a fashion similar to chlorobenzene. The fit
and data points are presented in Figure 4.8. The fit is not good, but
adequate. The five lowest concentration points were used to determine
the background ion count and the five highest concentrations determined
IE_o. The values derived are presented in Table 4.7, and are probably close
to the best that can be determined. The increased ionization efficiency of
o-dichlorobenzene in the PC over chlorobenzene is verified based upon this
fit. The ratio of IE_o for dichlorobenzene to IE_o for chlorobenzene is
about 47, which is in agreement with the ratio of electron capture rates
for the two compounds, which is 52 (Reference 12). This agreement supports
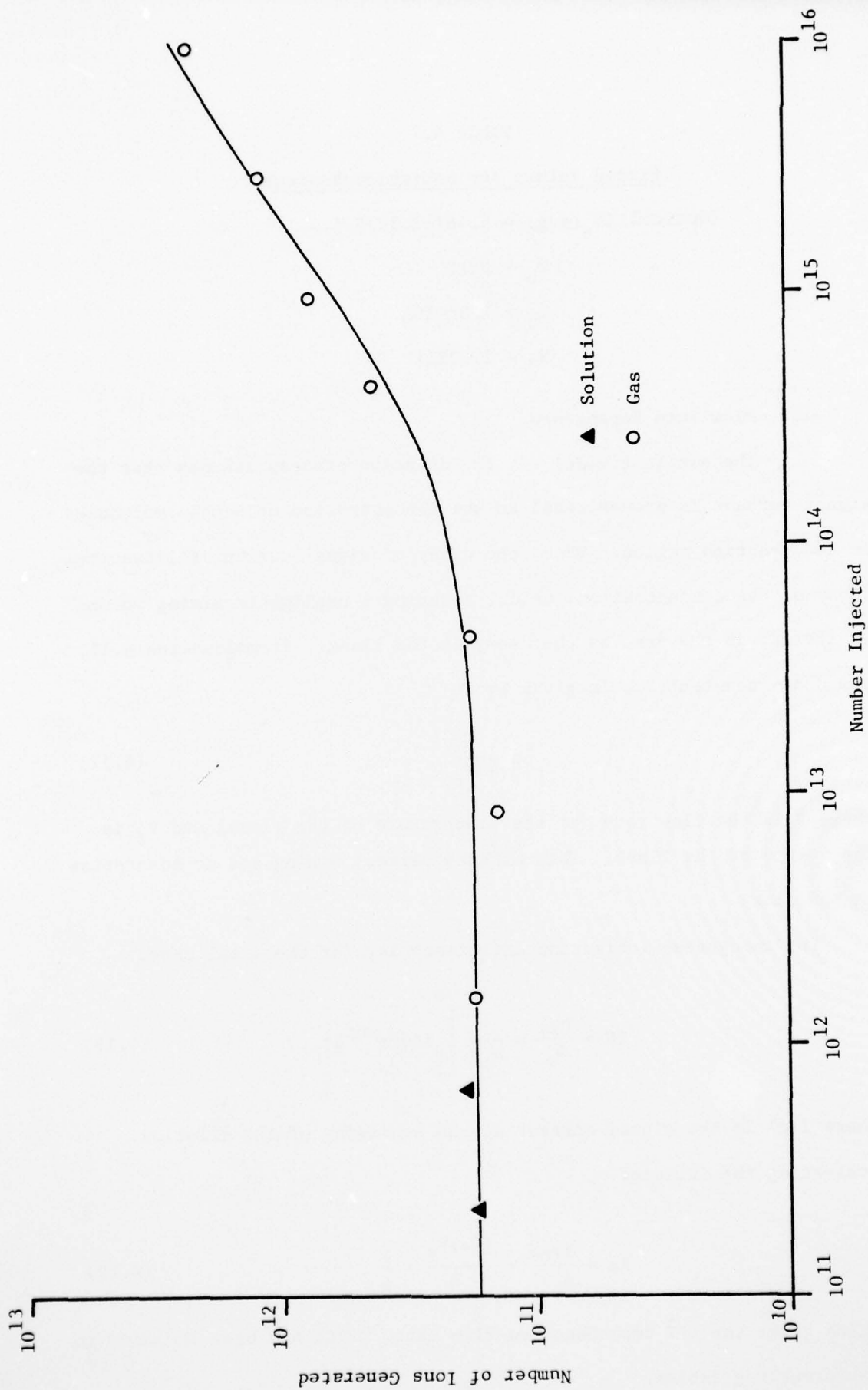the measurements and fitting procedure.

Figure 4.8. Ionization of o-dichlorobenzene.

79

Table 4.7

Fitted Values for o-Dichlorobenzene

(Optical) $IE_o(avg) = 5.46(\pm 1.52)E-4$

$$N_b = 2E12$$

$$I_b = 7.3E-10A$$

$$N_S = 1.72E11$$

4.6 Flow Rate Dependence

The simplest model for the dilution process assumes that the signal current is proportional to the concentration of sample molecules in the reaction region. Then, the decay of signal current follows the decay of the concentration, which, assuming a negligible mixing volume in the PC, is the same as the decay in the flask. From Equation 4.11, the decay constant, α, is given by

$$\alpha = \frac{\dot{F}}{V_f} \tag{4.17}$$

where $\dot{F}$ is the flow rate (at the temperature of the flask) and V_f is the volume of the flask. This assumes perfect mixing and no adsorption in the flask.

The integrated ionization efficiency is, for the ideal case,

$$IE = \frac{Q/e}{N_o} = \frac{1}{N_o e} \int_o^\infty I(o)e^{-\alpha t}dt \ , \tag{4.18}$$

where $I(o)$ is the signal current at the beginning of the dilution. Evaluating the integral,

$$IE = \frac{I(o)}{N_o \alpha e} = \frac{I(o)V_f}{N_o e} \cdot \frac{1}{\dot{F}} \ , \tag{4.19}$$

which gives the $1/\dot{F}$ dependence on flow rate, which has been included in the preceding tables.

80

Direct measurements on chlorobenzene as a function of flow rate verified this dependence. A solution was chosen at a high enough concentration to be in the linear region of ionization. Flow rates from 15 cm^3/minute to 178 cm^3/minute at room temperature were used. The results are presented in Figure 4.9.

This flow rate dependence has been derived from a model of the dilution flask, but it is more general than that. The instantaneous ionization efficiency can be obtained by balancing the flux of neutral molecules into the reaction region with the flux of ions out of the region, and the same inverse dependence emerges. As a result, the product of the ionization efficiency and the flow rate is a constant, independent of the method of introducing the sample into the PC.

It is useful to define this constant as the ionization rate for the instrument:

$$IR = IE\ (\dot{F}) \cdot \dot{F} \ . \tag{4.20}$$

The ionization rate has the practical units of (ions/sec)/(molecules/cm^3) and frees us from stating the flow rate at which the ionization efficiency was measured.

The derivation of Equation 4.19 makes two assumptions--namely, the current decays with the constant given by Equation 4.17, and the current rises instantaneously to its maximum value at time zero. Neither condition was strictly observed in practice. First, it was observed from the beginning that the signal decay constant, α_e, differed somewhat from the calculated volume decay constant, α_v, and was usually smaller. Second, for the chlorobenzene and for the proton-abstraction
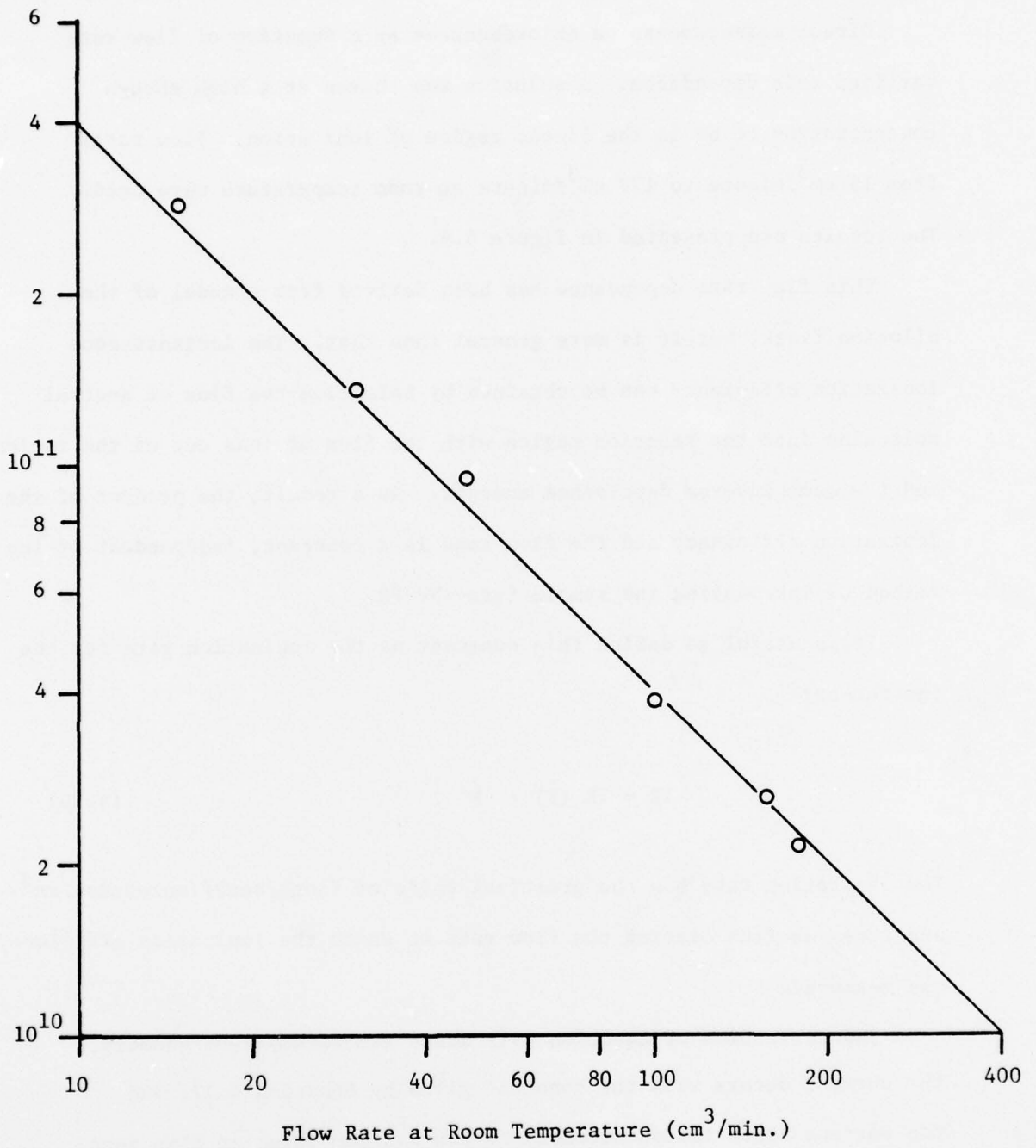
81

Figure 4.9. Flow rate dependence of ionization. Line has slope
of −1. Sample size was 10.7 µℓ.

data in the nitrotoluenes, the signal rose to maximum within about 10 seconds after injection; but after the flask was cleaned and silanized for the electron-capture data, the rise time was much longer, on the order of a minute.

The short rise time was in agreement with the calculated mixing rate in the volume of the reaction region and, in any case, was a small percentage of the duration of the dilution run. The $1/\dot{F}$ data in Figure 4.9 corroborate this.

On the other hand, attempts to measure a $1/\dot{F}$ dependence for TNT and DNT in the silanized flask were completely frustrated. The ionization efficiency was found to be relatively constant over a wide range of flow rates, increasing somewhat at high flow rates. Further, the value of α_e changed in relation to α_v, from being greater at low flow rates to being lesser at high flow rates. This failure of the integrated ionization efficiency to follow the $1/\dot{F}$ dependence seemed to contradict the results of Sedlak and Blurton (Reference 8), which indicated that the detector response would not affect the integrated efficiency.

Finally, a plot of α_e as a function of α_v for TNT, DNT, and chlorobenzene showed linear relationships with some surprising features. The slopes were not equal to 1 and there were non-zero intercepts. The implication of the non-zero positive intercept was immediately obvious: it represented a loss of sample by some mechanism.

A model to describe the data was developed. The main assumption in it was that the decay of signal current accurately described the volumetric decay of sample concentration in the flask. A secondary

83

assumption, borne out by experiment, is that the loss mechanism removed sample molecules at a rate proportional to the number in the flask. This secondary assumption leads to an overall exponential decay, which was experimentally verified for over 3 decades in each dilution run. The differential equation for the model is:

$$\frac{dN}{dt} = -\frac{\dot{F}}{V_{eff}} N - \alpha_o N \,, \tag{4.21}$$

where V_{eff} is an effective volume and α_o is the loss rate constant.

The solution is

$$N(t) = N_o \exp \left[(-\frac{\dot{F}}{V_{eff}} - \alpha_o)t \right] \,. \tag{4.22}$$

On the assumption that the signal current accurately reflects the concentration of sample in the flask, we obtain

$$\alpha_e = \alpha_o + \frac{\dot{F}}{V_{eff}} \,. \tag{4.23}$$

Plots of this relationship for chlorobenzene, TNT and DNT are shown in Figure 4.10. The chlorobenzene data are taken from the same runs as in Figure 4.9, while the TNT and DNT data are from separate runs from those in Sections 4.1 and 4.2. Both the TNT and DNT results were obtained using the electron-capture mobility peak in the cleaned-silanized flask.

The intercepts and effective volumes for the three plots were calculated by a least-squares method. The chlorobenzene intercept can be considered zero within the error of the fit. The DNT intercept is slightly positive, and the TNT intercept is significantly non-zero. The values are tabulated in Table 4.8. The effective volume, the
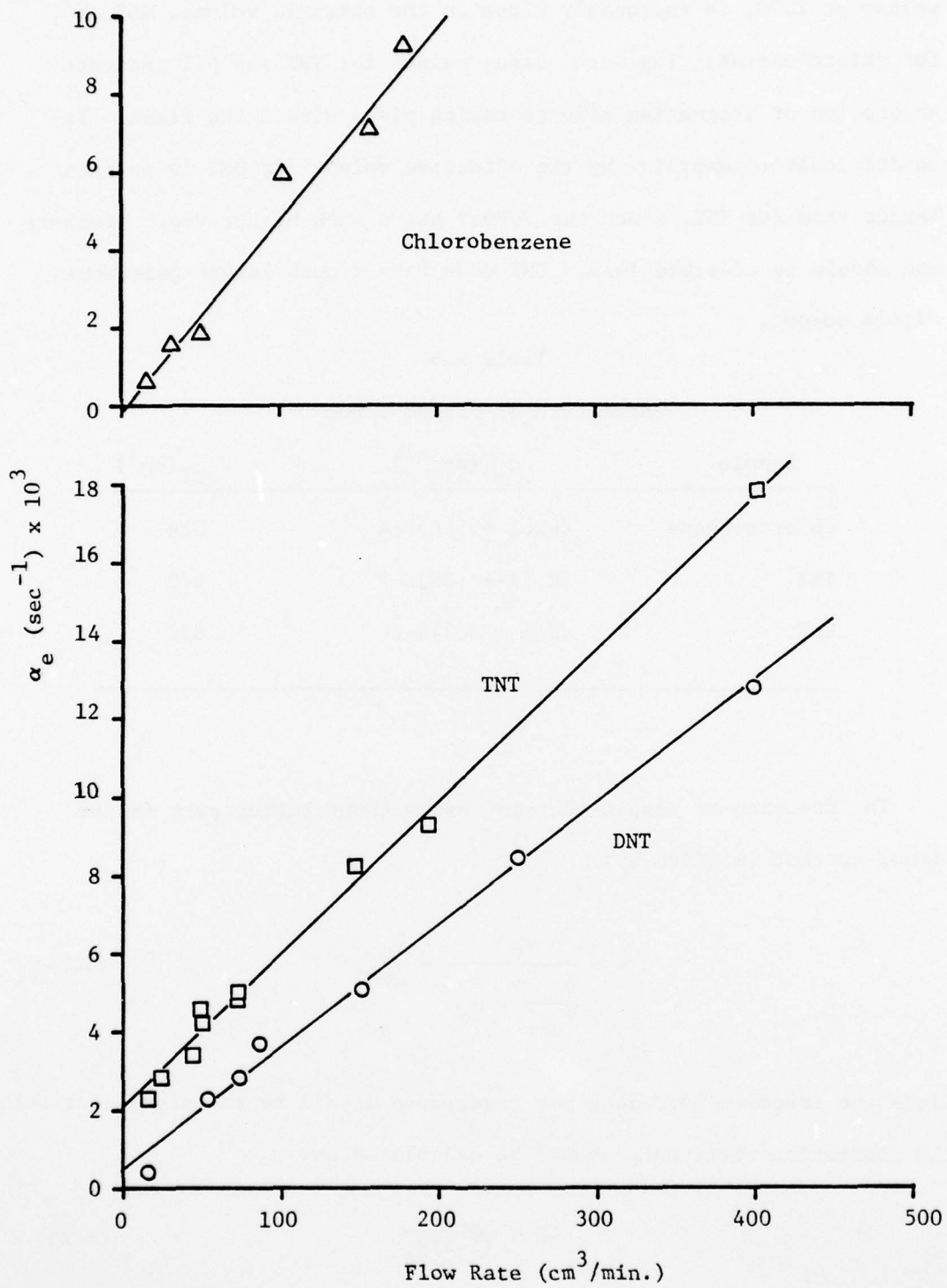
84

Figure 4.10. Current decay constant, α_e, as a function of flow rate.

volume at 20°C, is reasonably close to the physical volume, 469 cm^3, for chlorobenzene. The much larger values for TNT and DNT indicate absorption or stagnation effects taking place within the flask. It is difficult to explain why the effective volume for DNT is so much larger than for TNT, since the former has a much higher vapor pressure and should be adsorbed less. DNT does have a much larger permanent dipole moment.

Table 4.8

Parameters of Fitted Lines

Sample	α_o (sec^{-1})	V_{eff}(cm^3)
Chlorobenzene	$(-2.1 \pm 5.6)E-4$	514
TNT	$(2.14 \pm .35)E-3$	673
DNT	$(5.4 \pm 3.7)E-4$	827

The fraction of sample that is lost without taking part in the signal current is given by:

$$x = \frac{\alpha_o}{\frac{\dot{F}}{V_{eff}} + \alpha_o} = \frac{\alpha_o}{\alpha e} , \qquad (4.24)$$

Since the fraction lost does not contribute at all to the signal current, the ionization efficiency should be calculated as:

$$IE = \frac{Q/e}{(1-x)N_o} . \qquad (4.25)$$

86

This is the correction that was applied to the data in Sections 4.1 and 4.2 to account for the loss of sample, with the correction for DNT being about one-third of that for TNT.

Various possible sources of sample loss were postulated and tested. Tests for leaks outside the flask were negative. The few joints were checked and found secure; furthermore, a considerable underpressure was found necessary to pull laboratory air into the PC, indicating that the system was tight. A possible explanation for the loss is a leak internal to the PC. If the quartz tube is not adequately seated into the diffuser, some of the gas stream will pass into the space around the drift tube without going through the reaction region. It is known that the inlet tube was not well-seated for the TNT and DNT measurements, because it had been broken and shortened. Thus, a loss by this mechanism was very probable. It should have been the same for both TNT and DNT, since no changes in the physical arrangement were made between the two sets of measurements. Loss of sample by this mechanism would be very sensitive to the relative flow rates of the drift and carrier gases, since minute differences in pressure are the only forces moving the gases.

Whatever the source of loss, when the measured ionization efficiencies were corrected for the loss, a $1/\dot{F}$ dependence emerged for both the TNT and DNT data. This is reasonable, since a constant loss rate will affect the amount of material ionized most severely for low flow rates through the PC. The data were not as good as that in Figure 4.9 but were adequate to confirm the inverse flow rate dependence.

4.7 Summary of Data

Table 4.9 summarizes the limiting ionization efficiencies for the compounds measured.

87

Table 4.9

Limiting Ionization Efficiencies and Ionization Rate

Compound	Mode	IE_o(Optical)	IE_o(Ionic)	IR(Ionic) (cm^3/sec)
2,4,6-TNT	PA	4.25E-3	6.55E-3	8.81E-3
2,4-DNT	PA	1.50E-2	2.31E-2	3.11E-2
2,4,6-TNT	EC	3.65E-5	5.63E-5	7.57E-5
2,4-DNT	EC	1.46E-5	2.25E-5	3.03E-5
O-MNT	EC	4.31E-6	6.65E-6	8.94E-6
m-MNT	EC	1.20E-5	1.85E-5	2.49E-5
p-MNT	EC	2.92E-6	4.50E-6	6.05E-6
Chlorobenzene	EC	1.17E-5	1.80E-5	2.42E-5
o-Dichlorobenzene	EC	5.46E-4	8.42E-5	1.13E-4

5.0 SIGNAL PROCESSING

The Plasma Chromatograph is capable of several improvements in sensitivity in the area of signal processing. The signal-to-noise ratio (S/N) improvement of conventional signal averaging ought to be considered an essential part of plasma chromatography, but there are other means to achieve the same end or to improve upon the already good sensitivity of the instrument. These will be discussed in the following sections.

5.1 Automatic Baseline Correction

The numerical integration capabilities of the Nicolet signal averager suggested the possibility of direct recording of the dilution signal and obtaining its complete integral. There were several requirements that had to be met to make this approach useful.

First, the internal analog-to-digital converter had a maximum resolution of one part in 512, which meant that dilution runs producing S/N ratios greater than 512 would not be faithfully recorded. Furthermore, the maximum useful time constant on the Nicolet was 100 milliseconds, while the length of the dilution would require a channel time of 4 seconds typically. This would result in a mismatch between filter and averaging times, a situation in which less than maximum utilization is made of the signal.

The conversion problem was overcome by feeding the electrometer output to a voltage-to-frequency (V/F) converter, an Analog Devices 452J, whose pulse output was fed into the pulse counting input of the signal averager. The V/F converter produces pulses at a rate of 10^4 per volt input up to about 130 kHz. Since the full scale linear output of the electrometer is 7 volts, the converter is a good match for the electrometer. The maximum channel capacity of memory for the Nicolet

89

is $2.6 \cdot 10^5$, so that full output from the converter and electrometer together would just exceed the channel capacity in 4 seconds.

With the conversion problem solved, the second problem that hindered integration of the recorded signal was baseline drift. Over the period of a 4000-second dilution, any drift in the baseline would introduce an error into the integral. Measurements in the two-grid mode, made by alternately measuring the signal peak and the background level next to the peak, did indicate that the background level shifted during the course of a dilution, even when other sources of drift were small.

Therefore, an electronic circuit was built to provide an automatic shift of the second grid pulse from the signal peak to the baseline, with processing after the electrometer to measure and record the difference between the signals. The operation of this circuit is described fully in a publication (Reference 13), but an outline of its operation is included here.

A 40-Hz pulse signal is derived from the 60-Hz line (for timing accuracy) and is used to trigger the first gate repetitively. This rate is slightly less than the free-running frequency of the PC controller, which is about 41-Hz. The same 40-Hz frequency is divided further to selectable values of 1, 1/2, and 1/4 Hz, which are used for modulation frequencies. Only 1/4 Hz was used for this work. The modulation consists of using the internal delay of the controller to select the second gate pulse time for half the modulation period and then using an externally set delay to control the gate for the other half of the modulation period. This amounts to 2 seconds of signal and 2 seconds of baseline.

90

The demodulation is accomplished by a capacitor in series with the electrometer output. While the baseline is being sampled, the capacitor is grounded through an FET switch. This charges the capacitor to the value of the baseline signal and keeps the V/F converter from counting. While the signal is being sampled, the capacitor is in series with the electrometer and V/F converter, and the voltage on it is subtracted from the signal voltage. Thus, the V/F converter counts at a rate determined by the difference between the signal and the baseline. The schematics of the circuit are in Appendix 3. Figure 5.1 illustrates the timing relationships between the trigger and gate pulses.

The performance of the circuit is very good. Normally, when the instrument is turned on, or switched from the 10^{11} ohm feedback resistor and then back, severe transients occur, which result in a very long term drift. The correction circuit removes the drift nearly completely. A recording of the drift after a transient and the correction circuit output are shown in Figure 5.2.

During a dilution run, the direct output of the electrometer swings between the signal and the baseline and can be recorded, forming an envelope of the signal and baseline currents. The baseline-corrected signal stored in the signal averager can be recorded over it after the run, and the integral can then be performed and recorded. This was done for a DNT solution in Figure 5.3 and shows both the necessity of having the circuit for two-grid operation and the performance of it. Without the circuit, the signal would not have been accurately recorded, since the baseline shift was nearly equal to the signal itself. (The baseline current, due to the leakage of electrons through the grids, shifts because the supply of free electrons is used up in forming the negative ion.)
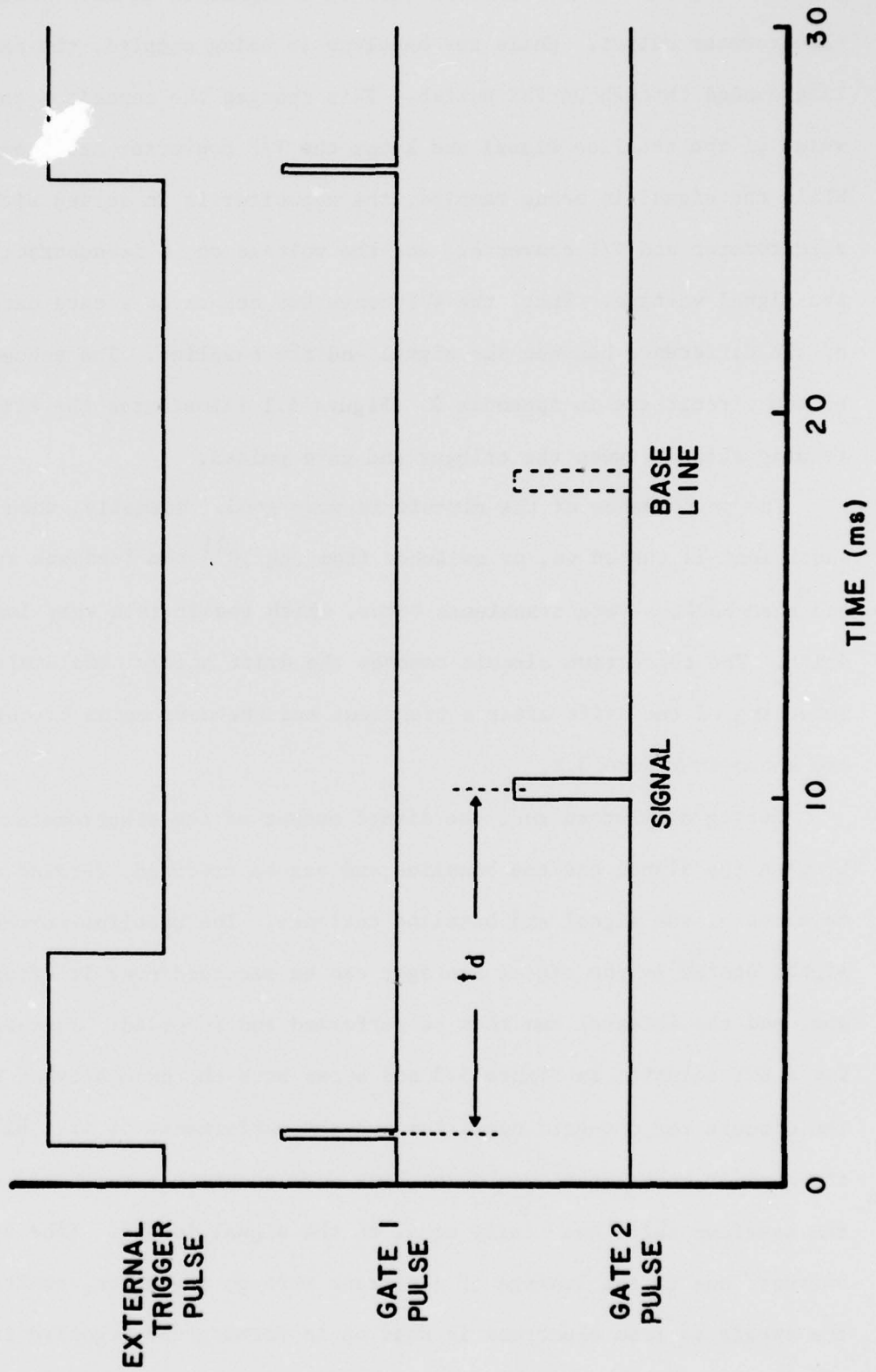
91

Figure 5.1. Timing relationships for the baseline corrector.

10^{-13} Ampere

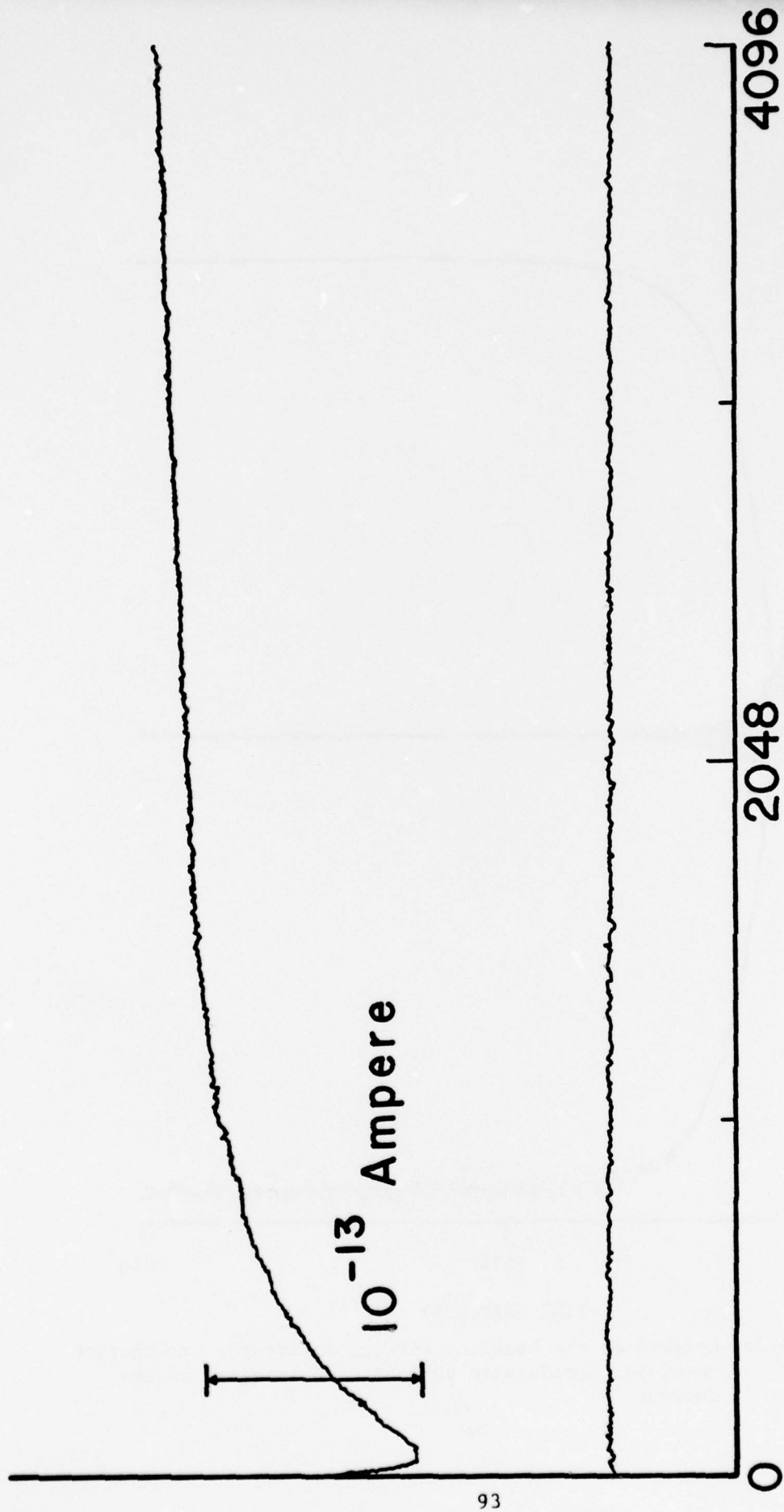TIME (SECONDS)

0   2048   4096

Figure 5.2. Corrected (lower) and uncorrected (upper) baseline drift following a transient.
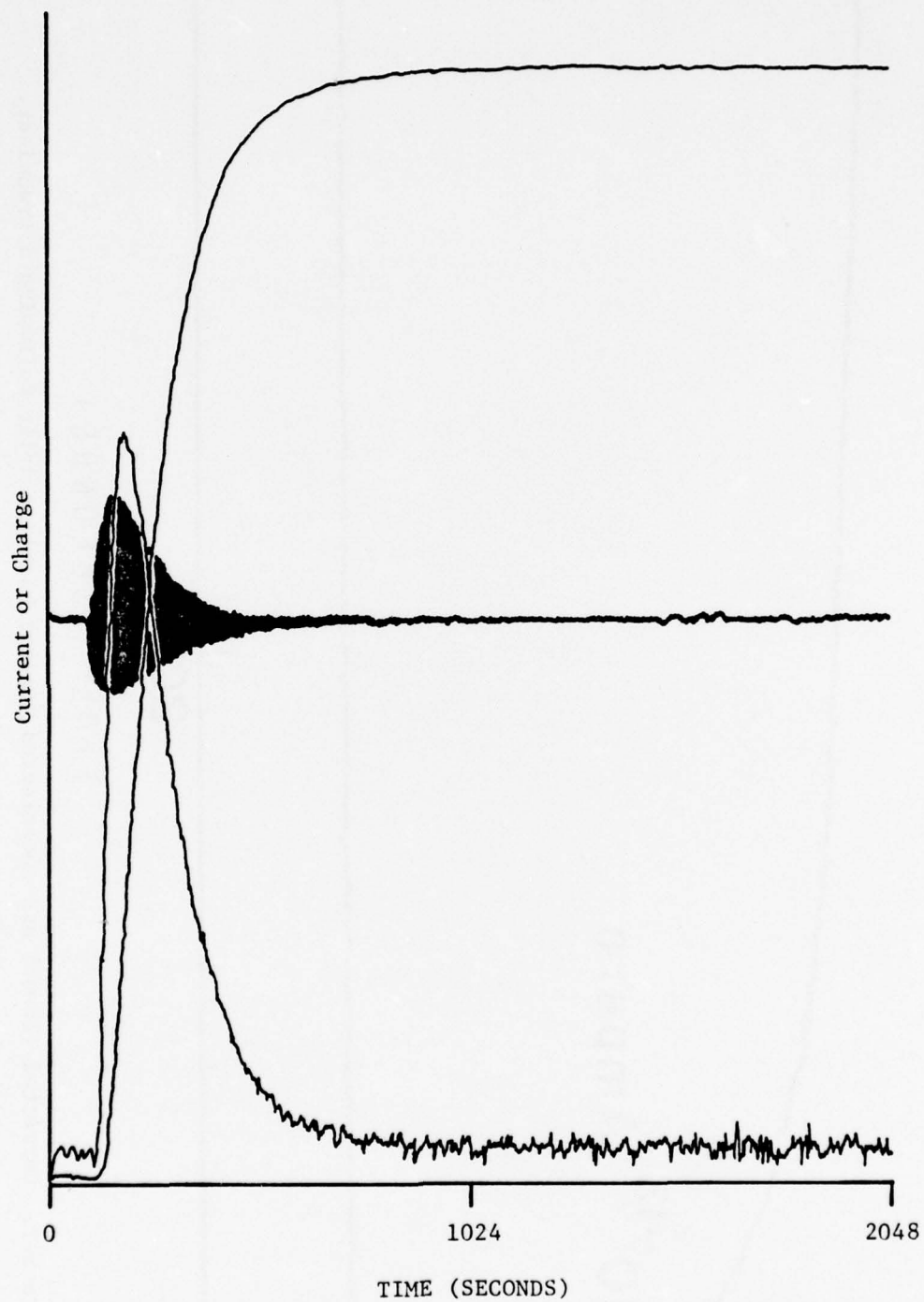
93

Figure 5.3. Outputs of the baseline corrector circuit: modulation
            envelope, demodulated current, and integral of the
            current.

94

The integral of the signal was constant at long times, indicating that the baseline of the corrected signal had very little drift.

Because of the response time of the electrometer, the signal does not come to equilibrium within the 2 seconds allotted for sampling. A direct calibration of the conversion gain of the circuit was obtained by recording the signal and baseline DC currents on one of the reactant ion peaks and then putting the circuit into operation and recording the number of counts per channel for the dynamic correction. Dividing the counts obtained in a 4 second modulation cycle by the differences in charge (current times time) actually transferred in 4 seconds, the conversion gain was determined to be $2.81 \cdot 10^{16}$ counts/coulomb. The measured noise current amplitude was $1.0 \cdot 10^{-15}$A rms, essentially the same as with two-grid operation by itself. The bandwidth of the 2 second sampling time is approximately 0.25 second, according to Equation 2.8. The approximate nature of the estimate comes from the slow response of the electrometer, which from Figure 2.4 has a single pole roll-off at about 0.68 Hz. The noise current is still limited by the aperture grid noise, as evidenced by a significant reduction when the voltage on the grid is reduced to zero.

5.2 Frequency Compensation

In an effort to reduce the noise of the preamplifier in the wide band mode, investigations into ways of using the 10^{11} ohm resistor in a wide band amplifier were made. The basic idea was to take the frequency response of Figure 2.4 for the 10^{11} ohm resistor and provide a frequency compensation network to achieve a wide band response. This technique has been used successfully in other applications (References 14 and 15), but was arrived at independently in this work.

95

Taking the frequency response for the 10^{11} ohm resistor from Figure 2.4 as a starting point, a compensation network was calculated. The form of this network is shown in Figure 5.4. The pair R_1-C_1 compensates the low frequency break in the preamplifier response. The pair R_2-C_2 reduces the compensation for the high frequency peak in the preamplifier. Resistor R_3 sets the overall attenuation factor of the compensation network. The calculated response for a set of values is shown in Figure 5.5, and the product of the compensation network and preamplifier responses is shown in Figure 5.6, along with the measured wide band response using the 10^8 ohm resistor.

The calculated response provided nominal values for the network. These were trimmed for a best peak shape using the free electron peak in nitrogen gas as an indicator. When the trimming was finished, the peak shape with the compensated preamplifier was nearly identical to the uncompensated preamplifier in the wide band mode. The compensated preamplifier had a DC conversion gain of 10^{11} volt/ampere, but the attenuation of the network at DC was about 800, so that the overall conversion gain was $1.25 \cdot 10^8$, quite close to the conversion gain of the 10^8 ohm wide band preamplifier.

There was no obvious difference in noise performance between the compensated and uncompensated amplfiers. Consideration of the wide band characteristics of the Burr-Brown 3421 operational amplifier seemed to show that this was due to its large current noise. Since its current noise was the dominant source, changing the size of the feedback resistor had little effect.
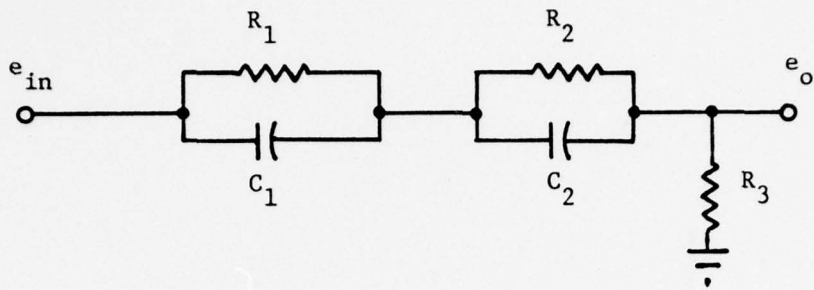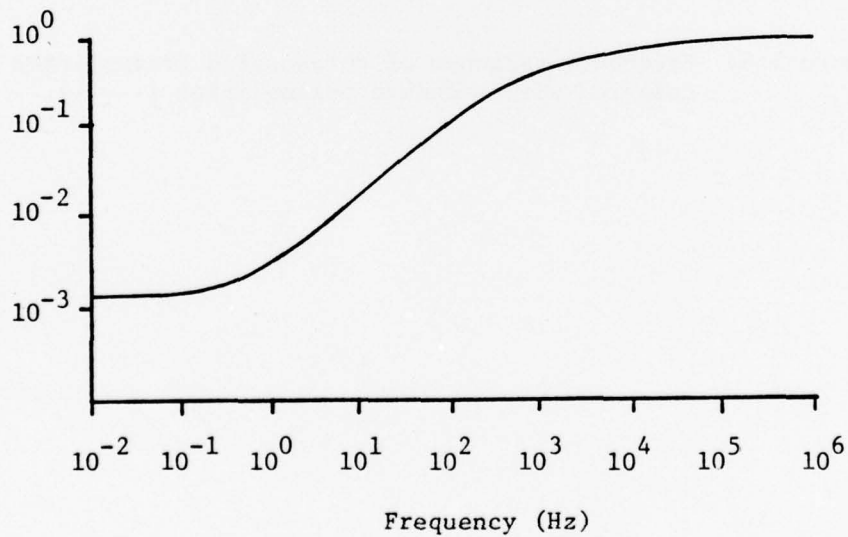
96

Figure 5.4. Compensation Network.

Frequency (Hz)

Figure 5.5. Frequency response of compensation network.
R_1 = 3.16 MΩ, R_2 = 5880 Ω, R_3 = 3920 Ω,
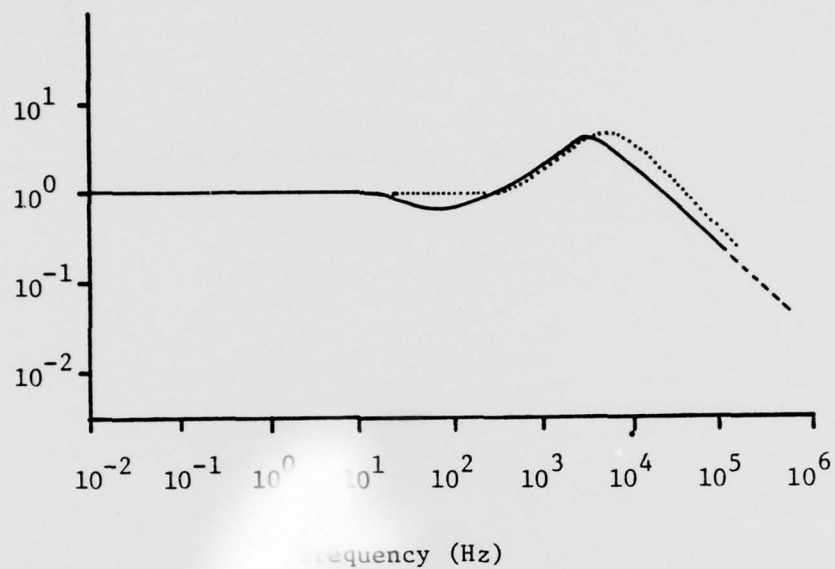C_1 = .075 mfd., C_2 = .0135 mfd.

97

Figure 5.6. Frequency response of compensated preamplifier (————), compared with standard preamplifier (·····).

98

The compensated amplifier was still very useful, even with no noise improvement. The compensation network was connected in parallel with the narrow-band filter amplifier so that both could be used simultaneously. This meant that one-gird or two-grid operation could be obtained by simply opening or closing the second grid. There were no transients generated in switching from the 10^8 ohm to the 10^{11} ohm resistor and the long term drift due to the switching transients was eliminated.

When in two-grid operation, the signal averager could monitor the signal appearing at the opening of the second grid, making possible a check of grid pulse width and position during the course of a dilution run. The only function the compensated preamplifier could not serve was to measure the open grid total current (about $7 \cdot 10^{-10}$A), since it would have required a DC output from the preamplifier of about 70 volts, far beyond its capability. As long as the average current through the electrometer stage was about $1.2 \cdot 10^{-10}$A or less (corresponding to Gate 1 open 17 percent of the time), the compensated amplifier was completely linear in its response.

To improve the observed noise performance of the compensated amplifier, a better operational amplifier was sought. The Burr-Brown 3523 had published specifications indicating improved current noise by a factor of 40 and improved voltage noise by a factor of 2; a unit was obtained and tested. For the first time, a difference in noise levels was seen between the 10^8 and 10^{11} ohm resistors. However, the noise performance improvement in the 10^{11} ohm position was only about a factor of two better than the 3421 amplifier, much less than expected.

99

The principal noise limitation of the compensated amplifier technique lies in the nature of the circuit. A simplified schematic, showing noise current and noise voltage generators, is shown in Figure 5.7. The current noise is amplified by the circuit in a frequency-dependent way, according to Figure 5.8. The feedback resistor and capacitor determine the low frequency break, and C and C_f determine the high frequency plateau. The very high frequency break is due to the response limitation of the operational amplifier itself. The voltage noise is essentially uniformly distributed in frequency at the input of the op amp, but at the output it has been multiplied by the function $A(o)/A(\omega)$ over the full frequency range, giving much greater emphasis to the high frequency components.

Now, when the output of this preamplifier stage is compensated, the compensation function is ideally $A(o)/A(\omega)$, so that the overall current gain is just

$$A_{comp}(\omega) = \frac{1}{B} A(\omega) \cdot \frac{A(o)}{A(\omega)}$$

$$= \frac{A(o)}{B} , \tag{5.1}$$

where B is the attenuation factor of the network. But the spectral characteristic of the noise is given by

$$e_n(\omega) = \hat{e}_n (A(o)/A(\omega))^2 , \tag{5.2}$$

where $\hat{e}_n$ is the noise voltage per unit bandwidth at the input of the op amp.
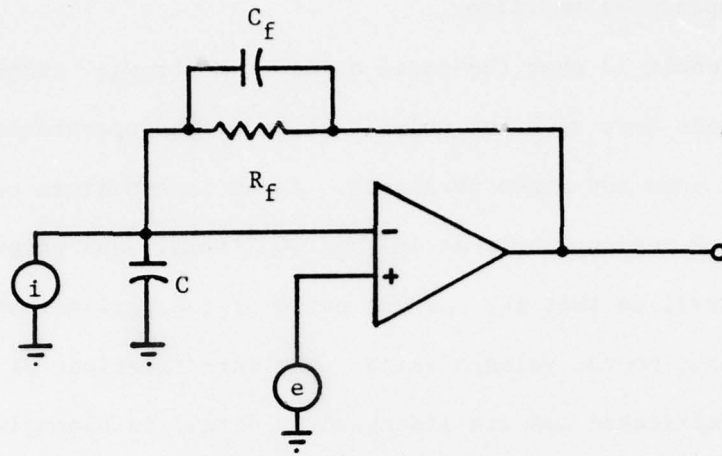
100

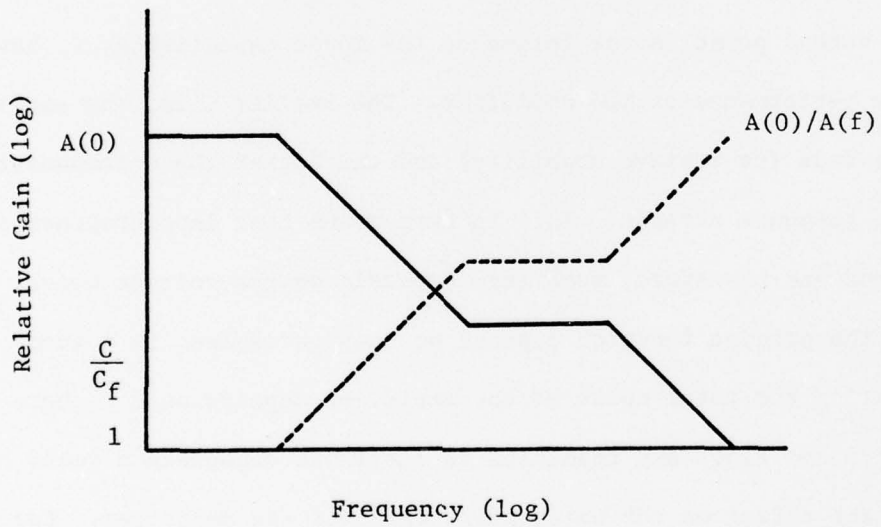Figure 5.7. Noise current and voltage inputs
to the electrometer.

Figure 5.8. Frequency response of preamplifier (———) and
compensation network (·····), idealized.

101

This represents a tremendous increase in the noise voltage at the output of the compensated amplifier.

The net result is that the total noise of a strongly compensated amplifier depends more upon the noise voltage of the operational amplifier than upon any other parameter. In an intermediate case, using a feedback resistor between 10^8 and 10^{11} ohms, less compensation would be required, so that the current noise of the resistor would become comparable to the voltage noise. The interrelations of all the factors are complicated and are discussed in detail in Appendix 1.

Two important conclusions result from this analysis. The first is that the voltage noise is so important because it is actually emphasised twice, first by the preamplifier and then by the compensation network.

The second point is the influence the input capacitance, C, has on the noise performance of the amplifier. The smaller C is, the smaller C_f can be made (to achieve stability) and the higher the uncompensated frequency response extends. This in turn means that less compensation is required and therefore, much less emphasis on the voltage noise. Although the precise function depends on many variables, to a good approximation the total noise of the amplifier depends on C^{-n} where n is between 1.5 and 2.5. Any reduction in the input capacitance would have an important effect on the noise performance of the amplifier. For example, the compensated amplifier in Reference 15 was able to achieve a bandwidth of 100 kHz with a 10^{11} ohm feedback resistor and to have an equivalent noise current of $5.3 \cdot 10^{-13}$ A primarily because the input capacitance was only 3.2 pf.

102

5.3 New Electrometer

The specifications of the 3523 operational amplifier were
similar to those of the 3421 in the region below 10 Hz, so very
little change in characteristics was expected. Measurements confirmed
this. The narrow-band noise was nearly identical to that of the
3421, being near the resistor noise value at shorter time constants and
exhibiting a 1/f dependence at the longer time constants. The narrow-
band noise is less than that associated with the aperture grid in any
case.

The measured wide-band noise using the 10^8 ohm resistor was
$5.7 \cdot 10^{-12}$ A rms. The amplifier specifications on current and voltage
noise levels would indicate that the dominant source of noise is the
resistor itself. However, for a bandwidth of 16 kHz, the noise due to
the resistor is only $1.6 \cdot 10^{-12}$ A rms. The problem is that the high
frequency peak in the response of Figure 5.6 accentuates the noise
enormously. The effective noise bandwidth for white noise (uniformly
distributed in frequency) is

$$f_e = \int_0^\infty |H(f)|^2 \, df , \qquad (5.4)$$

where $H(f)$ is the frequency transfer function. Performing a numerical
integration on the measured frequency response, the effective bandwidth
was calculated as 44-kHz, confirming the effect of the peaked response.
This does not mean that there are frequency components out to 44-kHz,
but only that the amount of noise corresponds to that of a 44-kHz

103

bandwidth amplifier. The calculated resistor noise for this wider bandwidth is $2.7 \cdot 10^{-12}$ A rms, in much better agreement with the measured value. The fact that the agreement is not better indicates another noise source, but it cannot be identified on the basis of the specified characteristics of the amplifier.

For the compensated preamplifier with the $1 \cdot 10^{11}$ ohm resistor, the measured noise was $2.4 \cdot 10^{-12}$ A rms. Because of the great sensitivity of the noise figure to the compensation network and to the total effective bandwidth, high frequency sharp-cutoff filters, which would affect the peak shape only slightly, produced significant changes in the noise level. Because these comparisons were not made for the 3421 amplifier in the compensated configuration, little more can be said about the two amplifiers except that the noise is in line with the wide band voltage noise specification for each. Detailed noise calculations for this amplifier are presented in Appendix 1.

5.4 Pseudo-random Gating

In Section 2.4, it was pointed out that the excellent noise performance of the narrow-band electrometer was in large part negated by the low duty factor of the ion pulse. The necessity for the mobility information to be extracted from the separated ion groups requires the input pulse width to be small and, together with the long drift time of the ions, required a small duty cycle. The detectability of any ion would be substantially increased if the duty cycle could be raised without losing the mobility resolution because the average signal current through the electrometer would be raised without any increase in electrometer noise.

104

Because the first grid can only be gated on and off (the second grid as well), the problem was first to provide a method of increasing the duty cycle while still preserving the mobility information. Going to longer duration gate pulses increases the signal for isolated ions until ion peaks begin to overlap. Then the mobility resolution is lost. Both DNT and TNT have mobilities well removed from other ions, so this technique could be used to some extent. Increasing the pulse repetition rate also reduces the duty factor but has the same problem with ion peak overlap.

However, if duty cycles approaching 50 percent are desired and if the ion spectrum is not well separated, then peaks will overlap. If the ions could be coded according to their mobilities, then suitable decoding would allow the increased duty cycle to be used.

After some consideration, it was found that a pseudo-random binary sequence (PRBS) was a suitable encoding sequence. The PRBS is one of a class of binary sequences, characterized by a length L and an index n. The length is related to the index by:

$$L = 2^n - 1 . \qquad (5.4)$$

The uniqueness of the PRBS is that within the length L, all possible combinations of n binary values (1 or 0) occur, except all zeroes, once and only once. Another statement of uniqueness is that all binary frequencies from 1 to n occur and only once. For a given length, L, one PRBS is identical to any other one, except for an integral shift in position (or time).

105

A signal generator can use an internal clock pulse to generate PRBS's. Then the clock pulse rate determines the minimum time between transitions and L determines the time between repeated sequences.

The last important property of PRBS's is an orthogonality property. If A is a PRBS of 0's and 1's and B is a PRBS of the same length, consisting of 1's and −1's, then the dot product A · B is zero unless A and B are coincident (no shift between sequences). It is this property which allows the separate ion peaks to be decoded.

If the first grid of the PC is triggered in a PRBS, which requires a slight modification of the controller, then as each ion species traverses the drift region, it will retain the PRBS coding. The different ions will drift at different rates, however, so that at the collector plate each ion sequence will have a different delay. If the output of the electrometer is multiplied and summed (forming the dot product) with a replica of the original PRBS suitably delayed, only the ions with that delay will add together; all other delays will cancel. Then any given ion can be selected at the collector by choosing a properly delayed sequence for decoding.

There are some problems. First, as described here, the electrometer must have a wide band response. Assume that the minimum drift time resolution is 100 microseconds (clock period = $1 \cdot 10^{-4}$ sec) and that a sequence length L = 255 is chosen. These match the customary PC operating conditions well. Then the electrometer needs the wide-band response in order to respond to the signals linearly, and its noise will therefore be higher. Its decoded output will be integrated for precisely 25.5 milliseconds, giving it a post-demodulation bandwidth of 19.6 Hz.

106

This bandwidth can be narrowed further for reduced noise, but calculations show that the intrinsic noise of the slow response electrometer is considerably lower for a comparable bandwidth.

Second, only one delay time or one ion can be measured at once with one demodulator. The full spectrum can be covered by slowly varying the delay between sequences, or it can be obtained by using 255 demodulators in parallel, each delayed by one clock period from the preceding one. This is not unreasonable in light of the complexity required in a signal averager. Moreover, the heart of such a decoder is commercially available (Binary-Analog Correlator, Reticon Corporation, Sunnyvale, California). It has 32 stages integrated into a single device, so that 4 or 8 devices would not require a major investment.

Third, a major noise source is inevitably introduced. This is due to the superposition of all the ions at once at the collector. Each ion current has its own statistical fluctuations, which do not totally cancel at the demodulator. They do average to zero, but contribute a noise term according to:

$$I_{ns} = (2eI\Delta f)^{1/2} , \qquad (5.5)$$

where e is the electron charge. The current, I, that should be used is the full open grid current, even through the average current though the electrometer will be half that value. The calculated noise will then be $1.3 \cdot 10^{-14}$ A/Hz$^{1/2}$, which for a 0.25-Hz bandwidth gives a noise current of $6.3 \cdot 10^{-15}$A. The noise expected from the wide-band electrometer, when filtered to this final bandwidth, would be comparable or somewhat less,

107

so that the overall noise performance would be expected to be about $1 \cdot 10^{-14}$ A rms. This is ten times higher than the noise expected in the normal two-grid mode, but now the effective duty cycle is 1/2, instead of $8 \cdot 10^{-3}$. Thus the equivalent noise referred to the reaction region is $2 \cdot 10^{-14}$ A rms, as compared to $1.25 \cdot 10^{-13}$ A rms for the smaller duty factor.

If the noise were unchanged, then it can be seen that the improvement ratio is proportional to the square root of the duty cycle improvement because of the shot noise from Equation 5.5. The extra noise generated in the wide-band amplifier is responsible for reducing the improvement, but it is still substantial.

The fourth potential problem is due to ion diffusion. The PRBS decoding orthogonality depends upon the ion bunches retaining their encoding through the drift region. However, it is known that diffusion and, to some extent, space charge effects broaden the ion peaks. The contribution that these effects will have is difficult to estimate. In the limit that all the encoding is lost, so that only a steady current with amplitude half that of the open grid current flows, the decoding process will average it to zero except for the shot noise. If subject ions of interest lose part of their encoding, then that much of the signal will not be decoded and will be lost. The main concern though is that strong ion peaks will create false responses by diffusing into the desired sequence. This is best evaluated experimentally.

A Hewlett-Packard 3722A noise generator was used to provide the pseudo-random sequence for gating the first grid. This generator also provides a variably-delayed sequence output, selected manually. A simple demodulator was constructed for the first test. Since the output of the

108

electrometer is unipolar, it was converted to a bipolar signal by passing it through a capacitor. An FET switch, keyed by the delayed sequence functioned as the multiplying stage, and a low-pass filter with time constant much longer than 25 milliseconds was used as an integrator. The schematic of the circuit is in Figure 5.9. When the circuit was tested with the generator sequence by itself, it provided the proper demodulation of the signal, giving a large DC signal when the sequences were coincident and near zero when they were not coincident.

Clock periods of 100 and 333 microseconds and an L = 255 were used in two separate measurements. In this way the same delay times could be accomplished with different delay settings. The generator is not capable of producing all delays for the sequence, so there are some discrete gaps in the data. The output of the demodulator circuit was measured with an oscilloscope of 1 megohm input impedance, giving a time constant for the integrating circuit of 6.4 seconds. The output of the oscilloscope preamplifier was measured with a digital voltmeter. The results of the measurement are shown in Figure 5.10, together with a conventional signal-averaged recording. The spectrum was that of free electrons in nitrogen with a trace of air background.

The results show the presence of the electron peak and the overshoot associated with it (evidence of imperfect compensation of the electrometer). The air ion peaks are much less well defined over the spectrum with the 100-microsecond clock showing some spurious peaks. These defects can be attributed to the simplicity of the demodular circuit, particularly using the input capacitor to obtain a bipolar signal. It is functioning as a differentiator as well, emphasizing the high-frequency components of the signal.
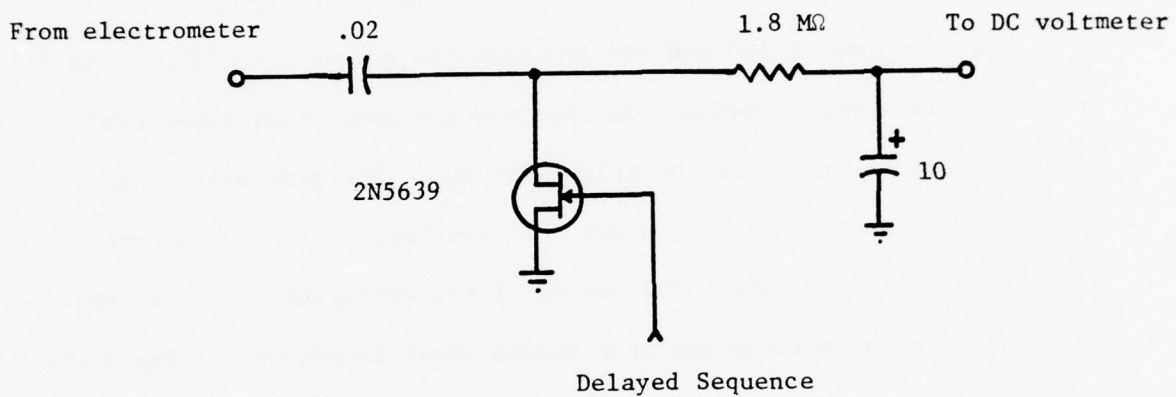
109

From electrometer   .02   1.8 MΩ To DC voltmeter

2N5639

10

Delayed Sequence

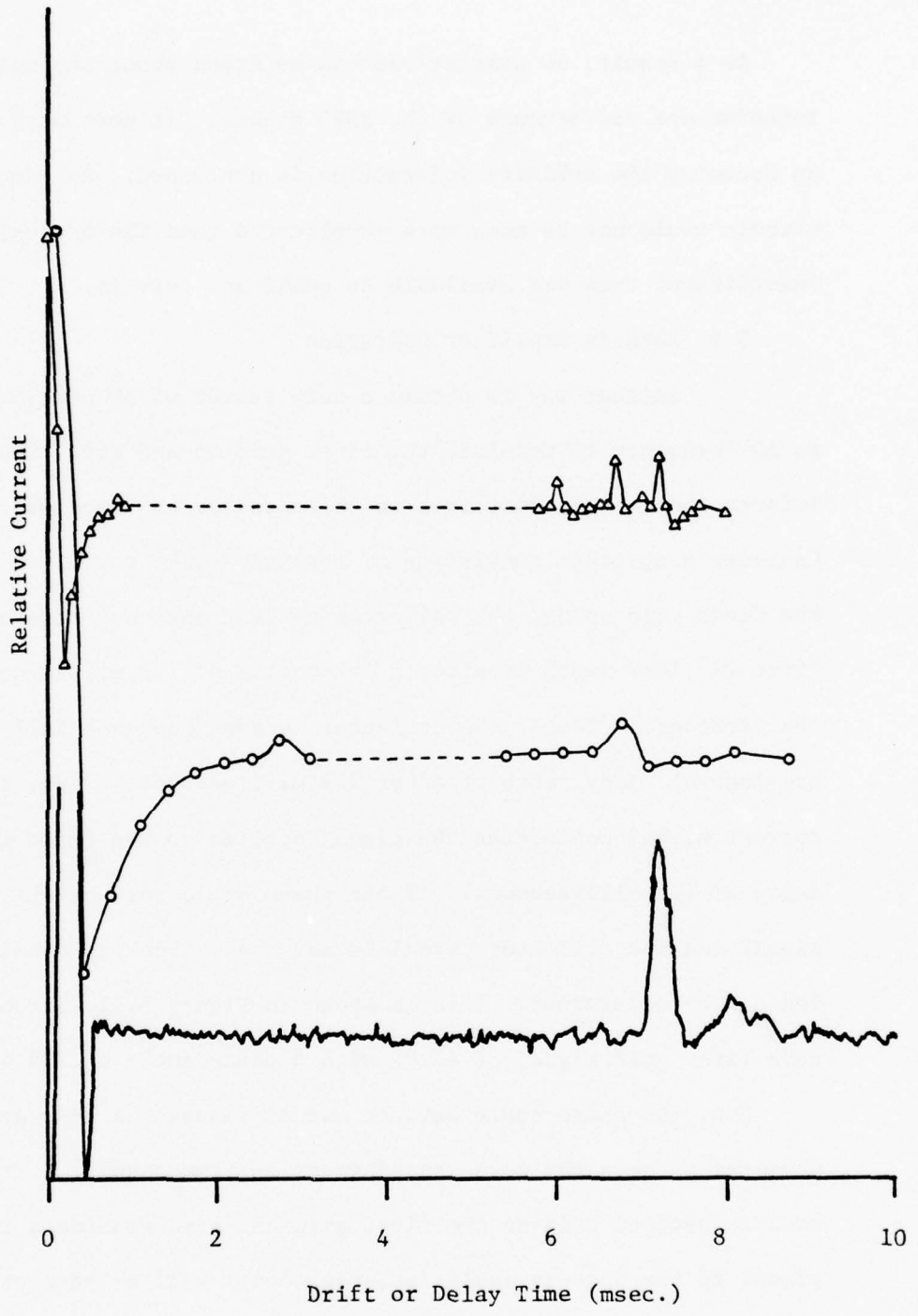Figure 5.9.   Simple pseudo-random decorder.

Figure 5.10.   Decoded Pseudo-random signals. Triangles: clock
period = 100 μsec; circles: clock period = 333
μsec. . Lowest trace: standard mobility spectrum.

111

As a result, no conclusions can be drawn about the noise and interference performance of the PRBS scheme. It does work as far as decoding the mobility information is concerned. An adequate decoding circuit would not be much more complicated than the one used, but insufficient time was available to build and test it.

5.5 Lock-in Amplifier Operation

Another way to obtain a duty factor of 50 percent is to use an AC frequency to modulate the first grid on and off. The mobility information is then contained in the phase of the received signal. Consider a spectrum consisting of a single peak, say Cl^-. Then, when the first grid opens, the collector current does not rise until the first Cl^- ions reach it after a drift time of 7.3 milliseconds. When the first grid closes, the collector current does not fall to zero until the last Cl^- ions reach it after 7.3 milliseconds. Thus, the collector current signal replicates the signal applied to the first grid, with a delay of 7.3 milliseconds. If the phase angle between the first grid signal and the collector signal is measured, then the mobility of the ion can be determined. This is shown in Figure 5.11, assuming a square wave first grid signal of 40 Hz with a phase angle of 105 degrees

Now, the phase angle between two AC signals is most accurately measured between the zero crossings of the two signals. If a square wave is used to trigger the first grid and also provide a reference signal to the lock-in amplifier, the signal will be zero when the phase of the lock-in is at 90 degrees to the electrometer signal, or at 195 degrees to the reference signal for Cl^-. The high gain of commercial lock-in amplifiers makes the measurement of zero signal quite easy to observe.
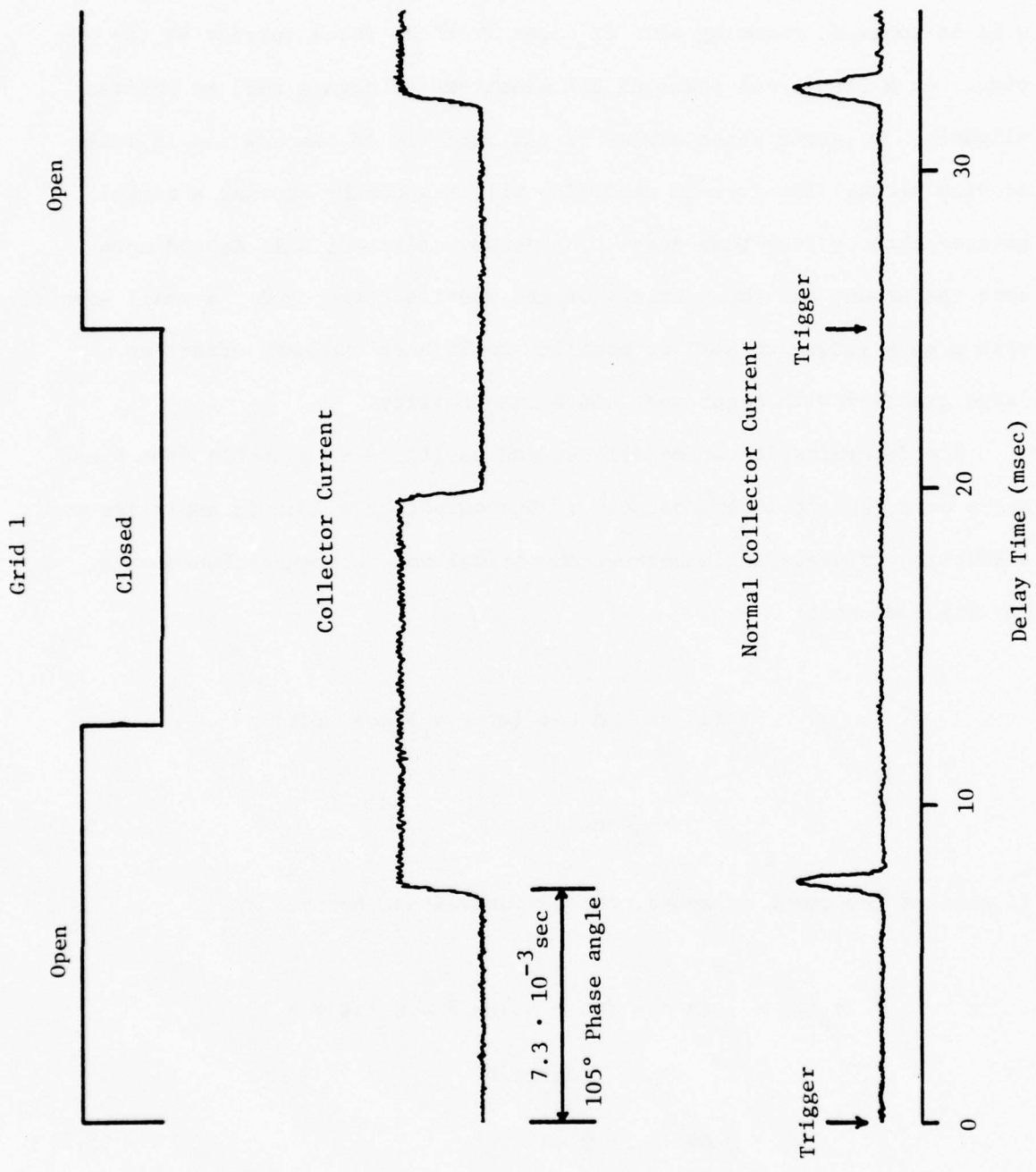
112

Figure 5.11. Relationship between drift time and phase angle for lockin amplifier operation.

113

If the phase of the lock-in is set so as to zero the electrometer signal, and then if another species is introduced into the plasma chromatograph, it will be ionized, removing some $C\ell^-$ ions from the total current at the same time. As a result the phase of the electrometer signal will be shifted slightly, to larger phase angles if the mobility of the new ion is lower or vice versa. The lock-in amplifier will respond by showing a signal greater than or less than zero. The amount of signal will depend upon both the amount and the mobility of the species introduced: a small quantity with a much larger or smaller mobility could have the same effect as a large quantity with a not very different mobility.

The determination of mobilities and amplitude is possible from phase angle data, but it is unproductive. The output of a lock-in amplifier as a function of phase angle between the signal and reference channels is, for one component:

$$e_o(1) = \int_0^\infty A \cos (\omega t + \phi_1) \cos \omega t \, dt$$

$$= \frac{A}{2} \cos \phi_1 \ . \tag{5.6}$$

If another component is added, the output voltage becomes

$$e_o(2) = \int_0^\infty [A \cos (\omega t + \phi_1) + B \cos (\omega t + \phi_2)] \cos \omega t \, dt$$

$$= \frac{A}{2} \cos \phi_1 + \frac{B}{2} \cos \phi_2 \ . \tag{5.7}$$

An n component spectrum would have n coefficients and n phase angles as unknowns. If the output of the lock-in were measured at 2n different

114

phase angles, all the unknowns could be determined, but the job would be enormous.

However, this method of detection is quite sensitive to detecting changes in the spectrum. The unbalance in the lock-in output voltage is proportional, approximately, to the signal current of an introduced ion: the difference between output signals for Equations 5.6 and 5.7 is $B(\cos \phi_1 + \cos \phi_2)/2$. It is to be expected that the noise current will again be dominated by the shot noise of the total ion current, since all the ions will be impinging on the collector. Wide-band response for the electrometer is not necessary, only response to about 40 Hz. Therefore, the noise introduced by the compensation is not severe.

In the sample measurement undertaken, the one-component spectrum was the free electron spectrum in nitrogen gas obtained by flushing the reaction region with drift gas. The two-component spectrum was the same as in Figure 5.10, a slight chloride ion and air. The chloride ion current was measured directly in the two-grid mode and gave a current, corrected for duty factor, of $2.7 \cdot 10^{-11}$ A. This current, with the duty factor of 1/2, was then used to calibrate the lock-in amplifier response, including the $\cos \phi_2$ term, which was near 1. The measured noise was about $1 \cdot 10^{-13}$ A rms, while the calculated shot noise was about $1 \cdot 10^{-14}$ A rms, for the same bandwidth. This discrepancy is not very significant, and probably represents a phase noise term not taken into account. Because the phase of the one component spectrum is set at 90 degrees, so that $\cos \phi_1 = 0$, small differences in phase can contribute relatively large output variations. It is not known what the source of the phase variations is, but a possible source is oscillator frequency instability. Whatever the source, the shot noise imposes a lower limit on the sensitivity of the technique.

115

It can be seen from this discussion that lock-in amplifier detection leaves much to be desired in terms of ion specificity. It offers, ideally, the same S/N improvement as pseudo-random encoding, namely as the square root of the duty cycle improvement. By proper choice of operating frequency, a third interfering component of the spectrum can be eliminated by allowing $\cos \emptyset_3$ and $\cos \emptyset_1$ to be zero at the detection setting.

The disadvantages of lock-in detection outweigh the increase in sensitivity available.

5.6 Signal Integration

A relatively simple processing technique that leads to significant noise improvement is integration. Integration is essentially a filtration scheme in which the noise bandwidth of the signal is reduced without affecting the signal itself. Of course, the integral of the signal is not of the same utility as the signal itself for determining mobility, but that is a tradeoff for improved sensitivity.

The peak shape of a single ion pulse is a Gaussian for gate widths less than the diffusion width (Reference 4). If the coordinate t_o represents the time axis of the pulse, and $f(t)$ its aplitude, then

$$f(t) = \frac{1}{\sigma\sqrt{2\pi}} \exp \left((t-t_o)^2/2\sigma\right)^2 \tag{5.8}$$

where σ is the standard deviation. The maximum amplitude of the peak is $(\sigma\sqrt{2\pi})^{-1}$. Ninety-nine percent of the signal occurs between the limits $-2.57 \leq t-t_o \leq 2.57$. The integral of Equation 5.9 is given by

$$\int_{-\infty}^{\infty} f(t)dt = 1 , \tag{5.9}$$

because of the normalizing factor $(\sigma\sqrt{2\pi})^{-1}$. In doing the integration with the signal averager, finite integration limits need to be set; and

116

since 99 percent of the integral is a good estimate of the area, limits of $t_o - 2.57$ and $t_o + 2.57$ are chosen. The parameter σ can be determined by the width of the peak at 1/2 maximum. It varies according to ion chosen, because the slower ions spread more by diffusion. For the electron-capture peak of TNT σ is about 127 microseconds, corresponding to a full width at half maximum of about 330 microseconds. Therefore, the integral is performed over a time interval of 653 microseconds, corresponding to a noise bandwidth of 766 Hz.

Now assume that the peak-to-peak noise (five times the RMS noise) is equal to the height of the peak, with an effective noise bandwidth of 44 kHz as for the wide-band electrometer. The signal-to-noise ratio is one. After integration, the integrated signal has the value of 0.99, and the noise has been reduced to 0.13 of its former value because of the reduced bandwidth. The signal-to-noise ratio of the integrated signal is 7.6.

This degree of improvement is substantial for detecting a minimal signal. The limits of integration do not determine the signal-to-noise ratio, although the bandwidth depends on the limits chosen. The signal is spread out, in a predictable way, over the interval 653 microseconds long, and it is only meaningful to compare the noise amplitude over the same interval. The improvement does depend upon σ, but from Reference 4, σ varies approximately as the square root of the drift time, and thus is relatively constant for ions other than free electrons. It also depends upon the noise bandwidth of the signal before integration, since a relatively narrow signal bandwidth will not be improved as much.

The integration of a noisy baseline provides a very sensitive indication of whether or not that baseline is zero, because the bandwidth is then determined by the duration of the baseline measurement, which can be thousands of seconds. This is, in fact, the method of choosing

117

the baseline for an exponential decay; it is adjusted so that the integral of the decay is constant at very long times beyond the decay.

5.7 Filters

Filters may be used to improve the signal-to-noise ratio when the actual noise bandwidth exceeds the signal information bandwidth; in other words, when the frequency response of the system can be restricted without loss of signal information. This situation applies to the PC electrometer generally, and, if the loss of some signal is allowed or can be accounted for, the improvement by filtering can be large. This is primarily due to the high frequency peak in the electrometer response. It enhances the noise much more than it does the signal, because the principal frequency components in the signal are below roughly $(4\sigma)^{-1}$, or 2 kHz.

In order to properly select a filter, the frequency content of the signal must be known. Assuming the signal has the Gaussian form, Equation 5.9, with a σ of 127 microseconds, the frequency content can be determined from its Laplace transform, which is

$$f(S) = \exp{(2\sigma^2 S^2)}[1 - \text{erf}{(\sigma S\sqrt{2})}] , \qquad (5.10)$$

where S is the complex frequency. A plot of the magnitude of this function is shown in Figure 5.12. For the given σ, the half-power frequency is 280 Hz. The energy distribution is in the form of harmonics of the basic 40 Hz repetition frequency, but the amplitudes of the harmonics are distributed according to Equation 5.10 and become nearly continuous at the higher frequencies.
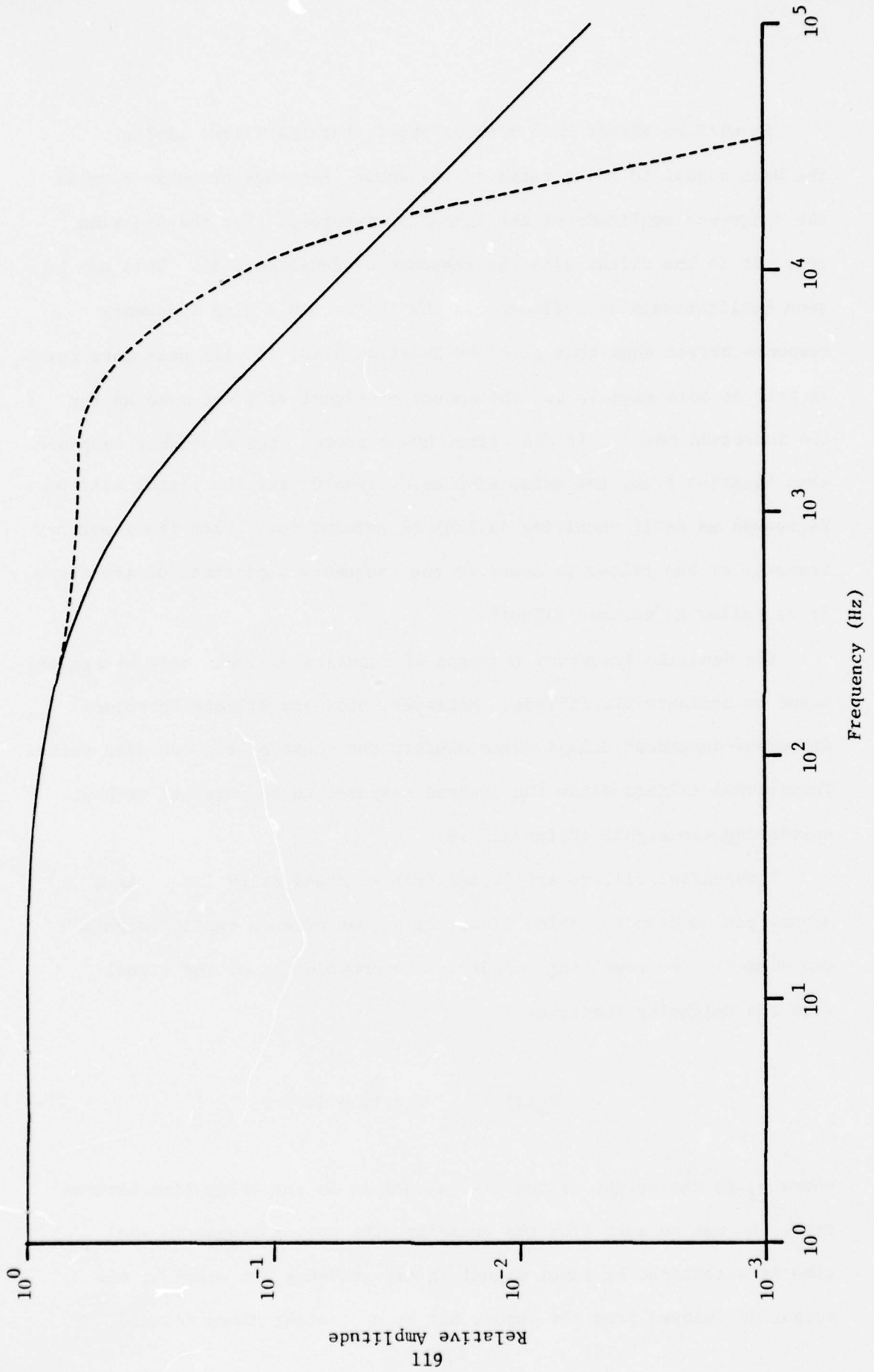
118

Figure 5.12. Frequency amplitudes of a Gaussian pulse (———) and as modified by the preamplifier response (----).

It will be stated here without proof that the filter giving the best signal to noise ratio is one whose frequency response matches the frequency amplitude of the signal of interest. For the Gaussian peak, it is the filter with the response of Equation 5.11. This may be seen qualitatively as follows: if the filter has a high frequency response better than that given by Equation 5.10, it will pass more noise as well as more signal, but the amount of signal will not make up for the increased noise. If the filter has a poorer high frequency response than Equation 5.10, the noise will be decreased; but the signal will be decreased as well, resulting in loss of information. When the frequency response of the filter is equal to the frequency amplitudes of the signal, it is called a "matched filter".

The Gaussian frequency response of Equation 5.10 can only be approximated by ordinary LRC filters. Moreover, ordinary filters introduce frequency-dependent delays which distort the shape of the Gaussian pulse. Transversal filters allow the desired response to be obtained without distorting the signal (Reference 16).

Transversal filters are formed from a tapped delay line. As a signal passes down the delay line, the output of each tap is weighted and summed. The resulting output is the convolution of the signal with the weighting function:

$$e_o(t) = \sum_{i=1}^{N} w_i e_s(t - i\Delta t) , \qquad (5.11)$$

where w_i is the weight of the ith tap and Δt is the delay time between taps. As can be seen from the equation, the output signal in real time is determined by input signal in the previous $N\Delta t$ seconds; the output is delayed from the input, but by a constant known amount.

120

The response of the filter in the frequency domain is the Laplace transform of its impulse response in the time domain. Therefore, for the signal of the filter to match the frequency distribution in the signal, the impulse response must be the same shape as the signal itself. For transversal filters, the impulse response is determined solely by the tap weights. If an impulse is introduced at time zero, then at each successive output, only that tap will be summed, so that the output signal consists of the response of each tap weight in succession. The impulse response can be matched to any signal by simply adjusting the tap weight for that corresponding part of the signal. (For the impulse response to match the signal, the taps must actually be matched to the time-reversed image of the signal, which is unimportant for symmetrical signals.) Then the frequency response of the filter is matched to the signal.

The transversal filter was made practical for this work by a semi-conductor analog delay line, the TAD-32 (Reticon Corporation). Use of the device as a filter is described in References 17 and 18. The unit is effectively an analog delay line with 32 taps. The delay is controlled by an external clock, with the signal sampled once every clock period. The sampled signal is transferred down the delay line one step with each clock cycle. It appears at each tap for one full clock cycle before being trans-ferred along. The output of each tap is connected through a variable weighting resistor to a summing or a differencing point, and further amplified for the output. The differencing operation allows for negative weights.

The taps were assigned near Gaussian weights, as shown in Figure 5.13. The 1st and 32nd taps were assigned values lower than required for the Gaussian shape to provide a smooth transition into and out of the filter.
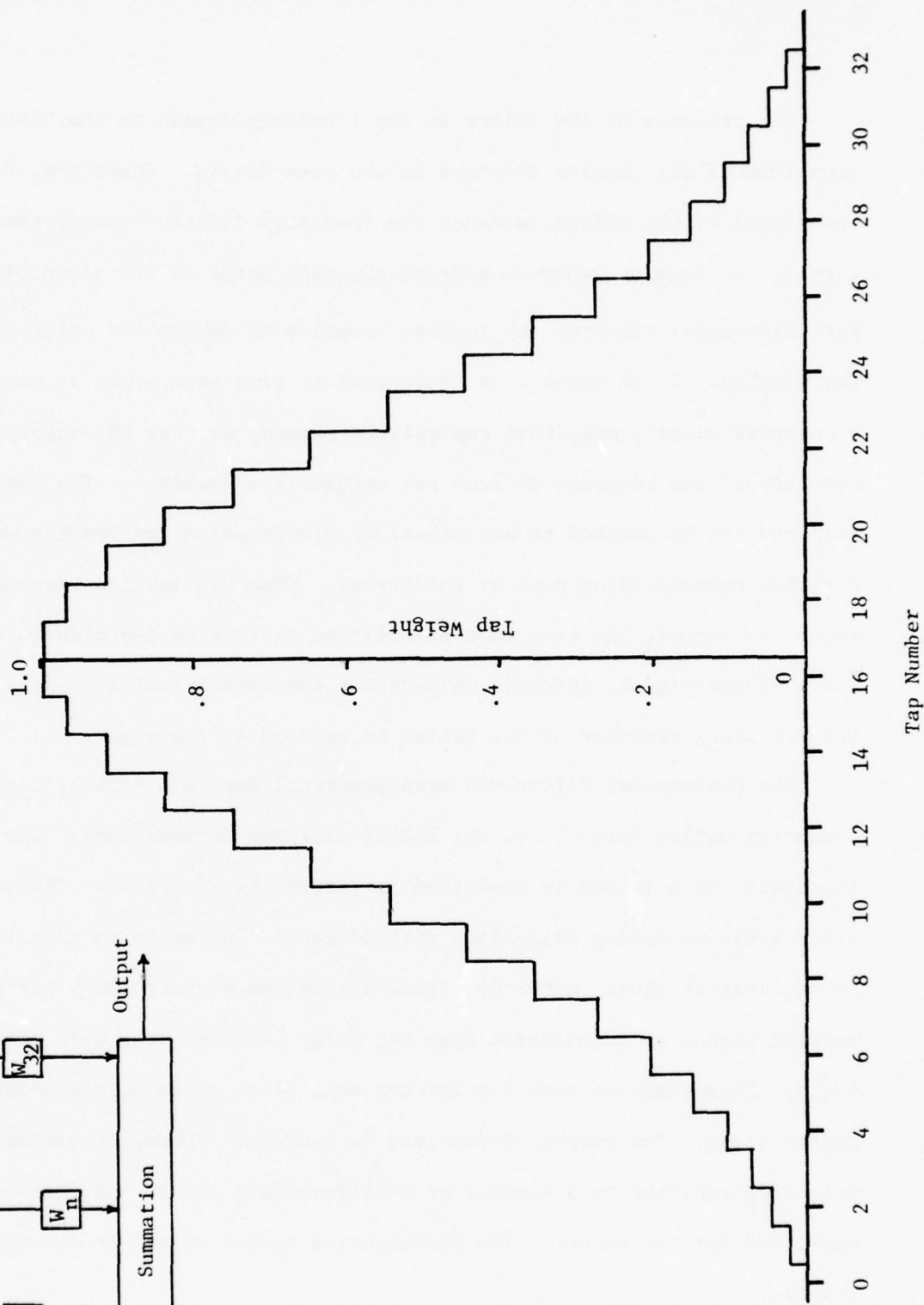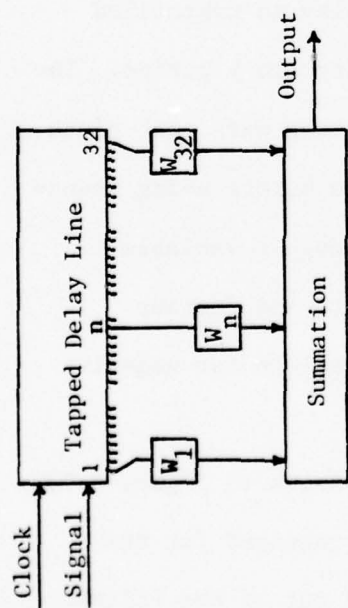
121

Figure 5.13. Tap weights for the transversal filter.

The σ for this filter is 5.96 taps, independent of the clock frequency. Any desired standard deviation in time, σ_T could be generated in order to match the peaks with differing widths throughout the spectrum.

To obtain a σ_T of 127 microseconds, the required clock frequency is 43.7 kHz. With this clock frequency, the impulse response of the filter is indeed Gaussian shaped, but the frequency response is radically different from the desired shape. The reason for the difference lies in the sampled nature of the filter. Because of the sampling theorem, frequencies above half the clock frequency will be lost at the input stage. Moreover, because the filter tap weighting is even, there are discrete frequencies where phase cancellation will occur; the lowest of these is at $f_c/17.5$. (The taps at 0 and 33 are counted, even though they are zero, and each tap has an effect half a clock period on each side of its center value.) Finally, the discrete nature of the tap weighting causes the most serious perturbations in the high frequencies, because the high frequencies are most seriously affected by the step changes in the impulse response.

The frequency response of the Gaussian filter at clock frequencies of 45.7 kHz and 65.4 kHz was measured and is shown in Figure 5.14. The responses do indeed go to zero at $f_c/17.5$, with a very sharp cutoff. Not shown on the figure are some slight responses at frequencies higher than the lowest null response frequency. It can be seen that the noise frequencies above 2 kHz are extremely attenuated so that the signal-to-noise ratio can be considerably improved if the signal remains acceptable.
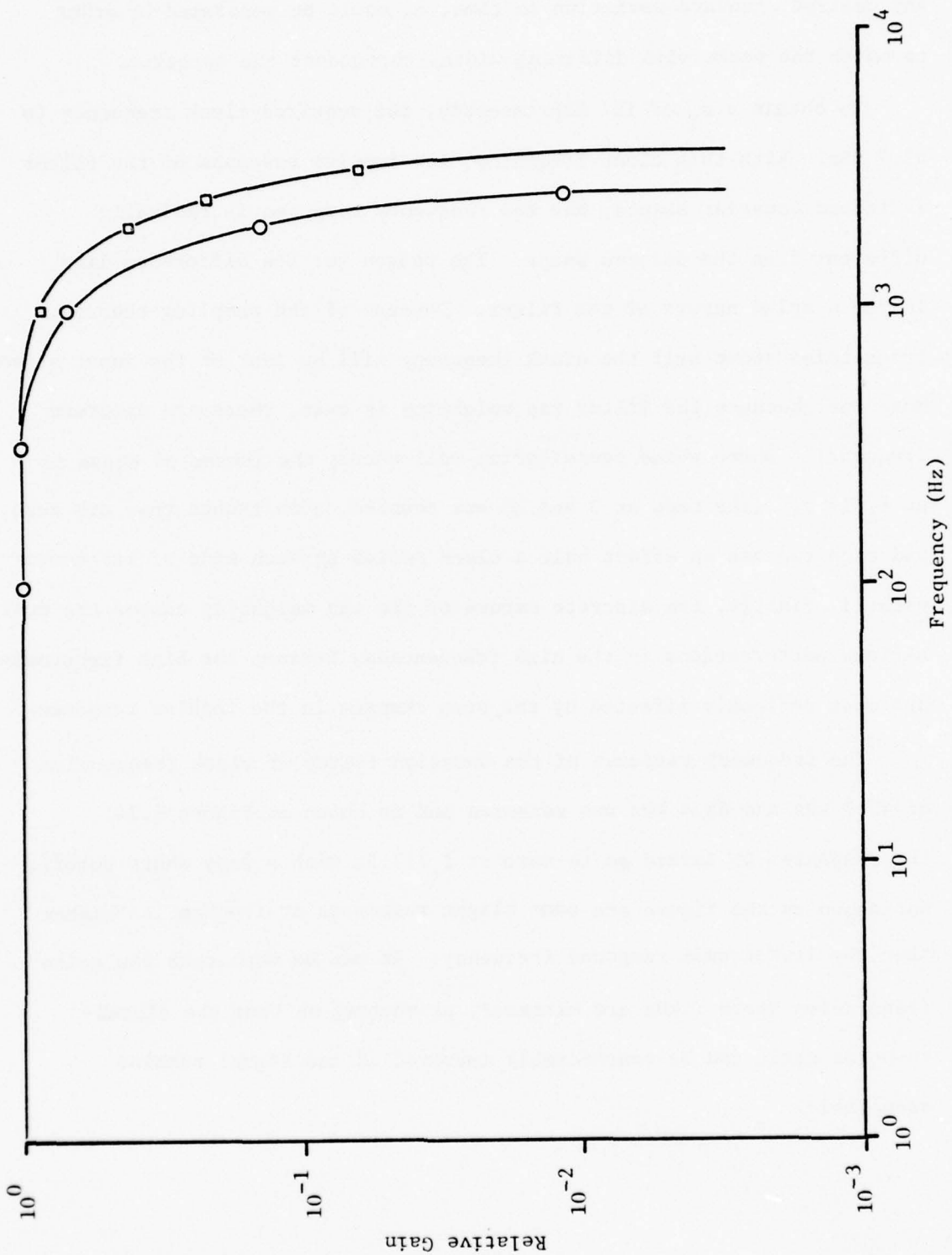
123

Figure 5.14. Frequency response of the Transversal Filter. Circles, clock frequency = 45.7 kHz; squares, clock frequency = 65.4 kHz.

124

Now, if a Gaussian with σ_1 is convolved with another Gaussian of σ_2, the convoluted function is also a Gaussian, with standard deviation given by:

$$\sigma^2 = \sigma_1^2 + \sigma_2^2 . \tag{5.12}$$

Thus, if $\sigma_1 = \sigma_2$, the width of the Gaussian is multiplied by the square root of 2 and the amplitude is divided by the square root of 2.

When the Gaussian signal is passed through the Gaussian filter, the peak of the output signal is delayed from the peak of the input signal by half the number of effective channels times the clock period. First, the peak arrival time of a reactant ion peak was measured with the filter out. Then, measurements of the peak arrival time for various clock frequencies were made. The relationship was determined to be:

$$\Delta t = 16.5T + 77 \cdot 10^{-6} ,$$

where Δt is the delay time and T the clock period, in seconds. The effective channel number is 16.5 here instead of 17.5 because the 0th channel does not affect the signal arrival time. The constant delay is a function of the whole filter test circuit and is unimportant once it is measured.

Equation 5.12 was also checked by measuring the width of the peaks (FWHM) as a function of frequency. The effective width of the filter was calculated as 17 channels rather than 14 channels from Figure 5.13. The difference may be due to departure of the filter from the ideal Gaussian shape.

The delay and spreading of the filtered pulse shape are shown in Figure 5.15 for various clock periods. The noise reduction is evident to some extent in the figure.

125

Figure 5.15.   Pulse delay and spreading after transversal filtering.   Clock
frequency for: A = 46 kHz; B = 65 kHz; C = 189 kHz; and D =
543 kHz.   E is unfiltered.   Gain settings for A-D are the same.

126

The noise performance was measured on an oscilloscope using a tangential method. This kind of noise measurement is prone to considerable error, but is simple and easy to do. Reducing the tangential noise to RMS noise requires an assumption about the random nature of the noise, but comparative measurements are usually in good agreement.

The calculated RMS noise currents are plotted as a function of filter clock period in Figure 5.16. Once the bandwidth of the filter begins to limit the noise, the noise current falls approximately as T^{-2}. Thus, small changes in clock period can reduce noise very rapidly. The amount of noise reduction available depends on how much distortion of the signal is acceptable. For a clock frequency of 50 kHz, the ion peak is broadened about 85 percent and its amplitude is reduced about 40 percent; there is some delay introduced, but the noise current has been reduced from the no-filter value by a factor of 33.

This transversal filter is a very powerful device and has barely been investigated in its applications to plasma chromatography. The most powerful aspect of its filter capability is the ability to change the cut-off frequency to suit the operating conditions. The transversal filter can be used in conjunction with other noise reduction methods to obtain an overall increase in performance that is the product of all improvements. Signal averaging can follow the filter, since it introduces no coherent noise of its own. Integration of the signal can follow the averaging. The convolution process in the filter does not change the total energy in the signal peak, but merely redistributes
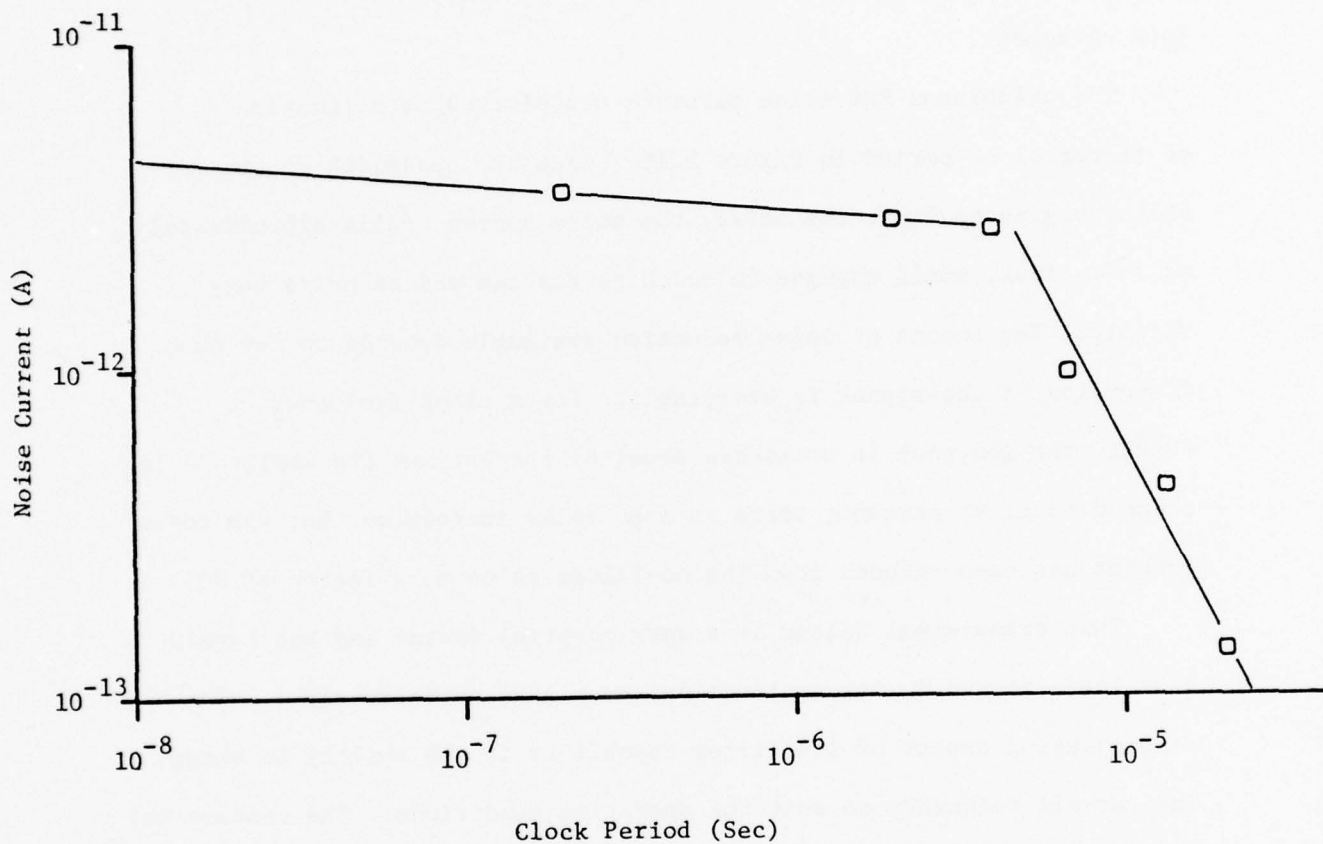
127

Figure 5.16. Noise current as a function of transversal filter clock period.

it in time. As the signal spreads, its amplitude falls so that the total ion charge per pulse remains the same.

The evaluation circuit used with the TAD-32 is not completely satisfactory because the signal is capacitively coupled through the filter. Not only does this result in loss of DC information, but it also introduces an undesirable tilt to the baseline which makes large expansions of scale and integration difficult. For regular use, a DC coupled circuit would need to be built.

5.8 Charge Summation

In this section, we want to present a conceptual approach to signal enhancement and the initial work done to implement it. The concept was not fully demonstrated because of a lack of time, but is worth further consideration.

In all the signal averaging techniques considered, both the signal current and the electrometer noise current are summed together. The S/N improvement is in proportion to the square root of the number of ion pulses summed. In charge summation, the charge in the same number of ion pulses is summed before being converted to a current in the electrometer. In this way, the noise current of the electrometer remains the same, while the signal current grows in proportion to the number of pulses summed. For large numbers, the advantage is decided.

The charge would be summed on the collector plate. Ion specificity would be ensured by operating in the two-grid mode. Leakage of the grids and any other leakage currents would be corrected for by using a slightly modified baseline correction circuit. The operation of the

129

circuits controlling the second gate timing would remain the same, but
an additional circuit would connect the collector plate to the electrometer
in time for all the charge to be removed and would then disconnect it
for the remainder of the cycle.

The critical element in this operation is the switch. It must have
rather demanding properties: very low leakage, rapid opening and closing
times (10-15 msec), and noiseless operation. Since it would be connected
between the collector plate and the input terminal of the electrometer, as
shown in Figure 5.17, any spurious charges associated with its operation
will degrade the noise advantage of the technique.

Magnetic reed switches were considered promising candidates for use
in this application because they are hermetically sealed in glass and
can be operated at frequencies of a few hundred hertz, indicative of
fast response. The reed switch is activated by an electromagntic field,
and the voltages developed when that field changes were a major cause for
concern.

Accordingly, a test rig was built to measure the effects. A reed
switch was mounted in a small chassis box, with each end connected to
a Teflon-insulated chassis-mount BNC connector. The actuating coil was
wound on an aluminum spool and was enclosed in a thin steel cylinder
to confine the magnetic field. The coil leads were twisted tightly
together and passed out of the box to a power supply. This test
apparatus is shown in Figure 5.18.

During the testing, one terminal was connected to the input of
a Keithley 610B electrometer The other was either left open or
grounded, with care taken to keep it shielded in either case. The
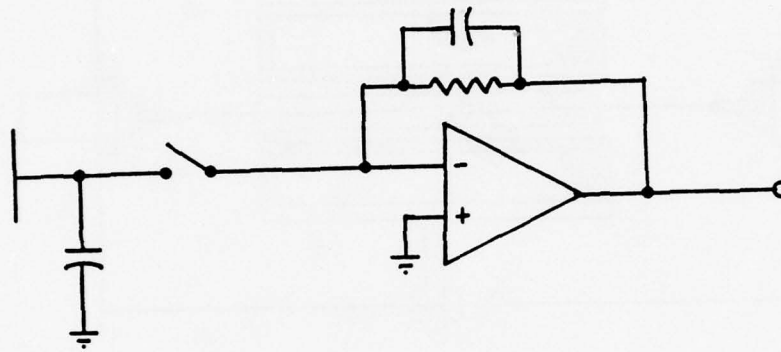current through the coil was the sum of a bias current, which was

130

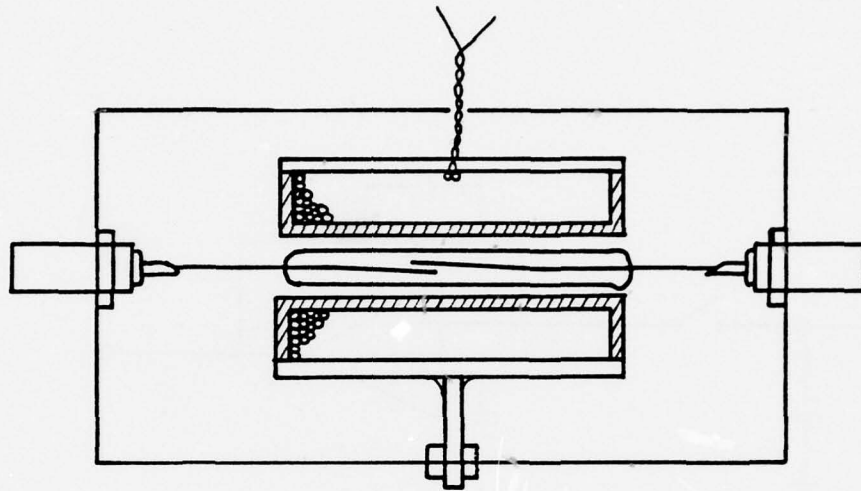Figure 5.17.   Preamplifier concept for charge summation.

Figure 5.18. Shielded test fixture for magnetic reed switches.

132

variable, and a switching current. The switching current was a low frequency, variable amplitude current having square, triangular, or sinusoidal waveshape.

The actuating coil had 350 turns of wire on it, and one reed switch out of an assortment was found which could be actuated with 15 milliamperes, giving an ampere-turns value of 5.25. Other reeds required three or four times as much current.

The electrometer was used as a coulometer, measuring the voltage across an internal capacitor. The intrinsic leakage of the instrument produced a slow but obvious drift, which was periodically reset. Induced charges showed up as steps or changes in the drift rate when the switch was operated.

The results of the tests were quite promising. If a switching current was applied to the coil with not quite high enough amplitude to actuate the reed, there was no visible pickup of the current on the coulometer (10^{-13}C full scale). If the end of the reed not connected to the electrometer was connected to ground, the cycling of the switch would produce a triangular shaped wave in which the electrometer drifted with the switch open and was zero when it was closed. If the other end of the reed were left open, the switch could be heard operating, but no visible changes in the drift rate occurred. It is estimated from these measurements that the leakage due to the switch was less than that of the electrometer (10^{-16} ampere) and that the amount of charge transferred by the switch closing or opening was less than 10^{-15} coulomb.

133

This performance makes the charge summation a real possiblility. An average current at the electrometer of $1 \cdot 10^{-15}$ A in the two-grid mode, just equal to the noise current, represents a total charge accumulation after 2 seconds of $2 \cdot 10^{-15}$ C. The switch perturbation would be less than this, hopefully much less, and if constant in time, would cancel out in the baseline correction circuit.

The attainment of this level of performance in the reed switch was not without problems. The Teflon insulators in the connectors appeared to have surface leakage currents, trapped charges, or even piezoelectricity. The least motion, even the vibration of the switch closing, would transfer charge to the electrometer. Usually, the effect could be reduced by washing the insulators with acetone or methanol and baking at 100°C overnight. No definite solution was found, and the problems of insulation and support would present the next major obstacle to be overcome.

The ultimate outcome of this line of investigation is unknown. Enough has been done to indicate the feasibility, and the hoped-for improvement in signal to noise ratio should provide the incentive.

5.9 Deconvolution

During the course of the research, it was occasionally desirable to be able to resolve two peaks more completely--for instance, when measuring the electron capture peak of DNT in the presence of its proton-abstraction peak. Such resolution was not available, even with narrow gate widths, since diffusion spreads each peak.

A deconvolution process could remove the effects of diffusional spreading and restore each peak to its original rectangular shape.

134

This would lead not only to better mobility resolution but also to better signal-to-noise ratio because all the signal energy would be concentrated into a narrower peak.

For use in a detection instrument, the deconvolution process must take place in real time. Until now, the process has involved considerable digital computation, requiring both time and investment to implement. However, a real time deconvolution method has been recently proposed and evaluated (Reference 19). The basic results form the basis for a conceptual approach to deconvolution in plasma chromatography.

If the recorded signal is $T(y)$, then its relation to the original signal, $t(x)$, is

$$T(y) = \int_{-\infty}^{\infty} t(x)B(y-x)dx , \qquad (5.14)$$

where B is the broadening function. After Fourier transformations and power series expansions, the relation can be inverted to give

$$t(x) = T(x) - \sum_{n=1}^{\infty} a_n T^n(x) , \qquad (5.15)$$

where T^n is the nth derivative of T and the coefficients a_n are related to the broadening function. Specifically, another set of coefficients, α_n, are defined by

$$\alpha_n = \frac{1}{n!} \int_{-\infty}^{\infty} B(x)x^n dx , \qquad (5.16)$$

135

and are related to the a_n thus:

$$a_1 = -\alpha_1 \, ,$$

$$a_2 = \alpha_2 - \alpha_1^{\,2} \, ,$$

$$a_3 = -\alpha_3 + 2\alpha_1\alpha_2 - \alpha_1^{\,3} \, ,$$

(5.17)

$$a_4 = \alpha_4 - \alpha_2^{\,2} + 2\alpha_1\alpha_3 - 3\alpha_1^{\,2}\alpha_2 + \alpha_1^{\,4} \, , \text{ etc.}$$

For even functions, the moments α_n are zero for odd integers. This applies to the Gaussian or rectangular pulse shapes. The usefulness of this approach to deconvolution is that good results can be obtained by a truncation at the fourth derivative.

The actual computation of the signal and derivatives is performed by a numerical procedure based upon equally spaced data points (References 20 and 21). A set of weights for an equal-spaced convolution is derived which is equivalent to a least squares polynomial fit of the data. In addition, all the derivatives of the fitting function are available, and as far as the function fits the data, the derivatives of the function will represent the derivatives of the data.

If an odd number of points is used (5 through 25), the value of the function and all the derivatives at the central point are available by summing the weighted data. This is precisely the computation provided by the tapped analog delay line.

The modified form of Equation 5.16 for fourth derivatives would be

$$t(x) = T(x) - a_2 T^{(2)}(x) - a_4 T^{(4)}(x) \, ,$$

(5.18)

where x now refers to the center tap of the computing interval. For instance,

136

25 taps could be used to compute the function and derivatives. The remaining taps on the TAD-32 would be unused. Assuming the same degree polynomial fit for the function and its derivatives, we obtain the following equations.

$$T(x_o) = \sum_{i=-12}^{+12} w_i^{(0)} T(x_i) \tag{5.19a}$$

$$T^{(2)}(x_o) = \sum_{i=-12}^{+12} w_i^{(2)} T(x_i) \tag{5.19b}$$

$$T^{(4)}(x_o) = \sum_{i=-12}^{+12} w_i^{(4)} T(x_i) , \tag{5.19c}$$

where $w_i^{(j)}$ is the weighting coefficient appropriate to the jth derivative for the ith point. Then

$$t(x_o) = \sum_{i=-12}^{12} w_i^{(0)} T(x_i) - a_2 \sum_{i=-12}^{12} w_i^{(2)} T(x_i)$$

$$- a_4 \sum_{i=-12}^{12} w_i^{(4)} T(x_i) ; \tag{5.20}$$

or

$$t(x_o) = \sum_{i=-12}^{12} (w_i^{(0)} - a_2 w_i^{(2)} - a_4 w_i^{(4)}) T(x_i) . \tag{5.21}$$

Thus, each tap has a weight that is a linear combination of the weights for the function and its derivatives. This analog computation operates in

137

real time, providing a deconvoluted signal after a brief delay (13 clock periods in this instance).

The choice of clock period is not critical. Ideally, the fitting function will not have to encompass more than one inflection point on the signal. This would set a minimum clock rate, depending upon the number of points used in the fits. Once a clock rate is determined, it sets a scale for calculating the broadening function moments (Equation 5.16). Varying the clock rate has the effect of varying the broadening function being deconvolved.

The promise of this deconvolution technique comes from the ease of implementing it. The value of deconvolution depends upon the requirements for increased resolution and, possibly, signal to noise improvement. There is an excellent opportunity to use transversal filtering to provide a much lower noise level, and then to deconvolve the filter function to remove the spreading of the pulse introduced by the filter.

5.10 Utilization of Displacement Current

All of the preceeding methods can be applied without modifying the SIFAD tube, which is difficult to do because of the presence of the radioactive source and the need for extreme cleanliness. During the course of the project, a calculation of the displacement current due to the ions moving down the axis of the tube was made. This is presented in detail in Appendix 5. The displacement current is a real current due to the changing electric flux at the collector plate from the moving ions. By removing the aperture grid or moving it close to the second grid, the

138

displacement current can be utilized to improve the effective duty factor of the two-grid mode of operation.

With the aperture grid removed, operation would be limited to the two-grid mode because only the second grid could provide the selectivity needed to separate the ionic bunches. The trade-off would be an effective sensitivity directly enhanced by the improved duty cycle.

It should be understood that the concept of duty cycle becomes slightly confused at this point.

Up to now, the duty cycle has been defined as the ratio of the opening time of the first grid to the time between openings. This admits a certain small fraction of the available ionic current to the drift region and the collector. In the two-grid mode, the second grid removes all but the desired ions; its opening time and duration of opening are carefully chosen to avoid cutting off any of the desired ions. This brief pulse is then averaged over the entire time between repetitions.

When the aperture grid is removed, the duty factor of the first and second grids remains unchanged, but now the displacement current in the collector as the ions cross the gap between the second grid and the collector raises the average current flowing in the time between repetitions. According to the calculations in Appendix 5, the average current is raised by a factor of 14. This can be translated into an equivalent improvement in duty factor so that we can continue to compare sensitivities as we have before even though no change in the conventionally defined duty factor has occurred. The collector has current flowing in it for a larger percentage of the time, and so its "duty factor" has been raised.

139

This concept of current utilization cannot be tested on the Beta/VII plasma chromatograph without modification of the SIFAD tube. Therefore, no tests of it were run. It is our understanding that an earlier model, the Beta/VI plasma chromatograph, was built without an aperture grid and could therefore be used to test the concept. The calculations suggest that improvement in the effective duty cycle could be far in excess of the 14 times arrived at, and that would rank this method of signal processing among the most sensitive of all the methods devised or proposed.

6.0 VAPOR CALIBRATION SOURCE

During the course of the project, it was found that the exponential dilution flask had some limitations that made it inconvenient. For instance, in determining the effect of a solvent, it is difficult to determine what effects are due to the solvent itself and what are due to the changing level of sample. This is one case where a steady source of sample at a known concentration would be desirable.

The National Bureau of Standards has constructed a source of explosive vapors to do just that (Reference 22), and it was decided to construct a similar unit to provide the same capability.

The concept of the vapor source is simple. A column of porous material (a typical gas chromatographic column) is coated with a substantial quantity of the explosive material desired. The support material has a very large surface area, and the column length is long. If a stream of gas is passed through the column, it will carry the explosive vapor with it. The column parameters are chosen so that the vapor stream is saturated for a wide range of gas flow rates. Thus, the concentration of vapor is dependent only on the temperature of the column.

In practice, the column is kept in a constant temperature bath, which is adjustable over a wide range but has a slow response time. Rapid changes in concentration are achieved by diluting the saturated vapor stream with a flow of pure carrier gas. This allows dilutions by a factor of 100 to 1 with relative ease.

In this souce, the supply gas is breathing air. It is passed over a catalyst (0.5 percent palladium on 1/8 inch alumina spheres) maintained at 250°C in order to oxidize all hydrocarbons in the air.

141

The catalytic burner is followed by a permanganate oxidizing agent (Purafil) to further oxidize NO to NO_2 and finally by a molecular sieve (Linde 13x) to remove the water vapor.

The gas stream is split and fed through two flow meters and flow controllers, one for the diluting air and one for the vapor source. The diluting stream is fed directly to the mixing volume, and the sample stream is fed to the column.

The column is a glass capillary, 2 mm i.d., and 6 feet long, coiled into a 4-inch diameter helix. Two columns were prepared, one for TNT and one for DNT. The glass was silanized with a commercial silanizing agent, dimethyldichlorosilane (Sylon CT from Supelco). The column packing and method of preparation were the same as in Reference 22.

The column was completely immersed in the constant temperature bath. The bath is normally maintained at or below room temperature by a mechanical cooler (Neslab CC-60 II). The high vapor pressure of DNT requires fairly low temperatures for very small concentrations, and the refrigerator is capable of regulated operation down to -60°C, well below what is normally required. The bath is vigorously stirred by a motor and paddle, since the degree of temperature regulation depends strongly on the stirring.

The temperature probe for the cooler was originally enclosed in a sealed stainless steel tube. This isolation from the bath fluid introduced an undesirable hysteresis into the cooling cycle and made the temperature regulation poor. Therefore, several narrow slits were cut into the tube to allow circulation of the fluid. Since the temperature sensor was two sealed diodes, and since pure ethanol was used as the bath fluid,

142

no deterioration of the sensor was expected. The slits do improve the temperature regulation considerably.

The mixing, or dilution, volume is a glass cylinder of about 100 cm^3. The two gas streams are fed in through fine glass jets which are aimed at each other to create maximum turbulence. The outlet tube is a 12-mm glass tube, chosen to allow the quartz inlet tube of the PC to be inserted well into it without touching the walls. The connecting lines to the mixing volume are made of glass, and both lines and volume were silanized. The mixing volume is enclosed in a small insulated box, and a heating mat inside allows the temperature to be maintained at about 100°C.

All of the components of the vapor source are shown in Figure 6.1. The connections from the gas supply to the glass tubing were all stainless steel. The stainless tubing was isolated from the rigid glassware by a flexible stainless steel bellows with the same outside diameter as the glass. The junction of each bellows with the glass tubing was sealed with heat-shrinkable Teflon tubing. Several joints in the glass part of the system were also butted together and sealed with the shrinkable Teflon in order to make the changing of columns somewhat easier.

In Reference 22, the experimental concentrations were fitted to an equation of the form

$$\ln c = -\frac{a_1}{T} + a_0 , \qquad (6.1)$$

where c is the measured concentration (mole fraction), a_1 and a_0 are the adjustable constants, and T is the absolute temperature of the column. The fitted values are in the following table.

143
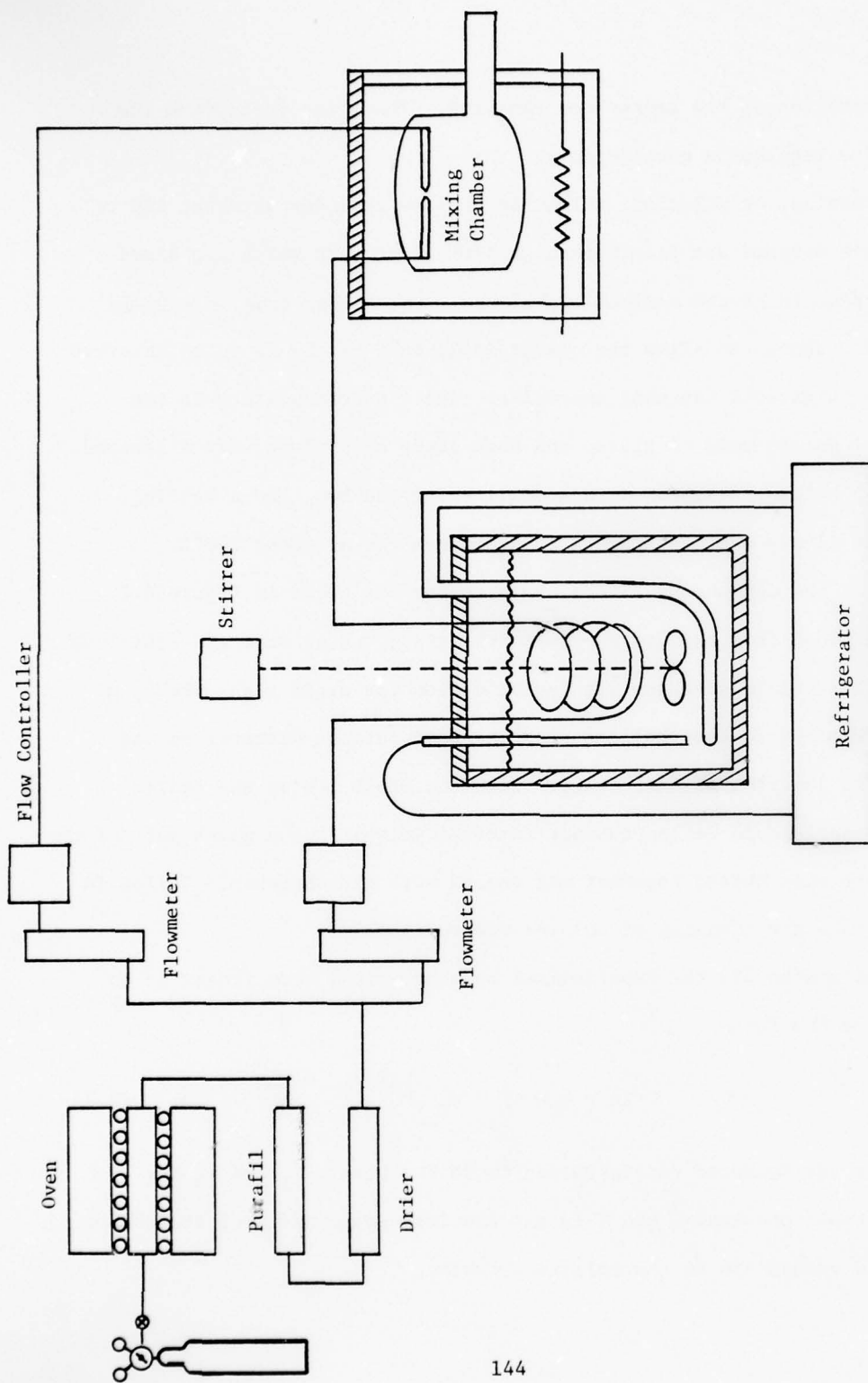
6.1. Vapor Calibration Source.

Table 6.1

Fitting Constants for Vapor Pressure

Sample	a_o	a_1
TNT	$21.71 \pm .77$	11916 ± 242
2,4 DNT	$23.49 \pm .44$	11495 ± 137

The results of calculations of concentration must be corrected to the total molecule density at the temperature and pressure of operation of the PC in order to compare them--that is, Equation 6.1 gives the mole fraction of TNT in air and must be multiplied by the number of molecules per cubic centimeter to obtain the number density of molecules.

The number of molecules per cubic centimeter is given (according to the ideal gas law) by

$$L(P,T) = 2.69 \cdot 10^{19} \cdot \frac{273}{T} \cdot \frac{P}{760} \tag{6.2}$$

with T in Kelvins and P in millimeters of mercury. The concentration of neutral TNT molecules would be given by

$$[N] = cL(P,T) . \tag{6.3}$$

Assuming the volume flow of carrier gas is sufficient to replace the molecules lost through ionization, the number of ions produced per second is given by

$$I/e = IE \cdot \dot{F} \cdot [N] \tag{6.4}$$

where the current is the ion current before grid losses, and $IE \cdot \dot{F}$ is a constant.

145

The vapor source was run at four temperatures high enough to give a substantial signal and the currents were measured. Assuming the value of 50 cm^3/min at 20°C for $\dot{F}$, the average effective IE was calculated to be 7.98 $\pm$ 1.60 E-3.

This is in reasonable agreement with the expected value. The measured currents as a function of vapor source temperature and the calculated current using this value of ionization efficiency are shown in Figure 6.2.

These results indicate that the vapor source is operating well. Another series of measurements were made with varying gas flow rates through the source column. The inlet flow rate was held constant at about 30 cm^3 per minute but could not be measured well. The drift gas and exit flow meters were not calibrated well enough and lacked sufficient resolution to determine the inlet rate. Nonetheless, as the vapor source flow was increased, the measured current increased as well, until more vapor-lader air was emitted than the PC would taken in. At that point, the signal current became independent of vapor flow rate, indicating that the PC was measuring a constant concentration of vapor in the air.

The measurement was repeated at a lower source temperature, and the results were essentially the same. There was a slight decrease in measured signal at a very high vapor flow rate. This may have been due to a changing reactant ion distribution due to changes in the amount of laboratory air in the PC. These results are shown in Figure 6.3.

The diluting capability of the vapor source allowed changes in concentration of about 10 to 1 to be made in a matter of moments. This was tested by monitoring the TNT signal with no diluting gas and then turning it on. With the PC operating at a temperature of either 160°C
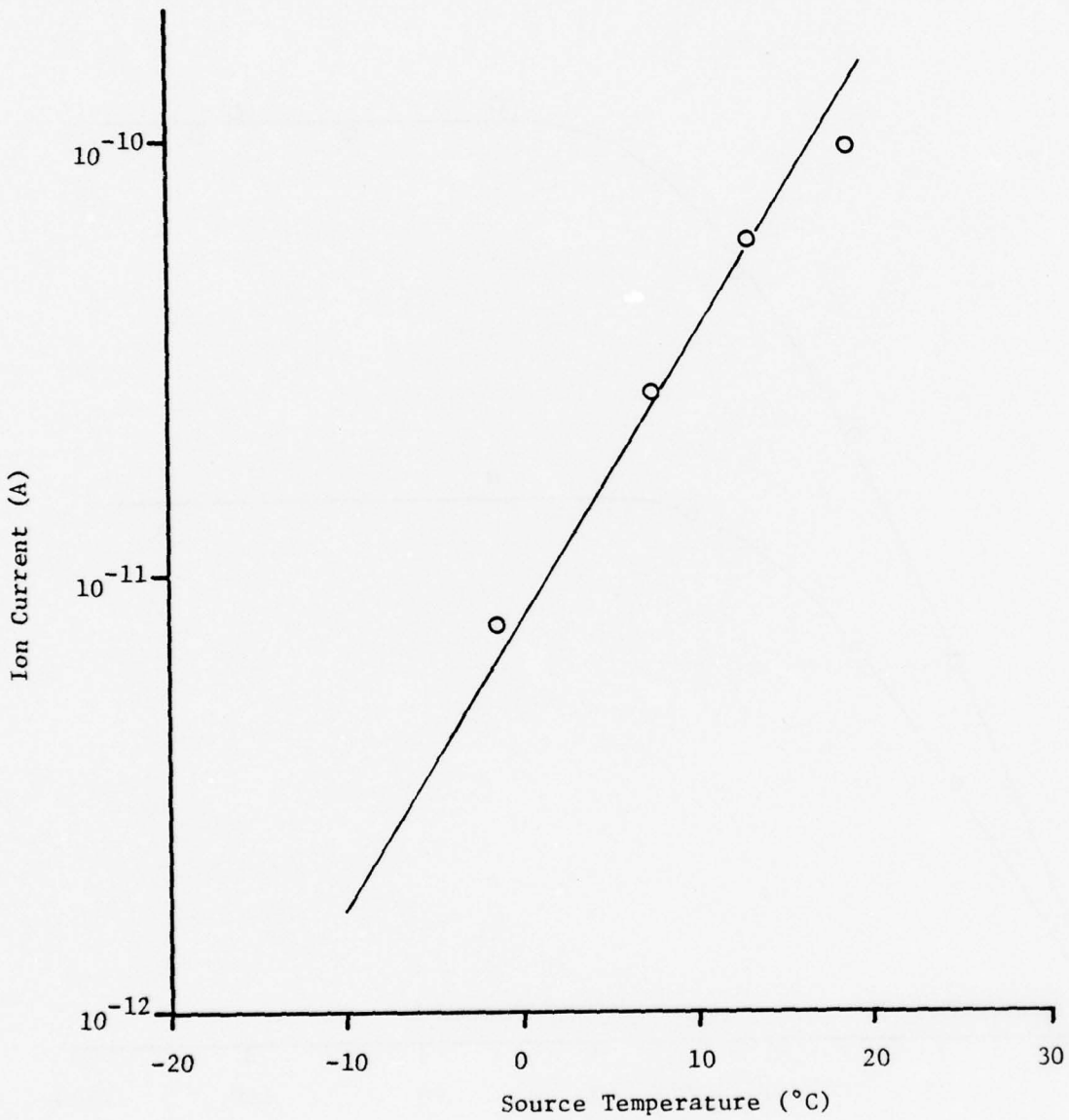
146

Figure 6.2. Ion current as a function of TNT
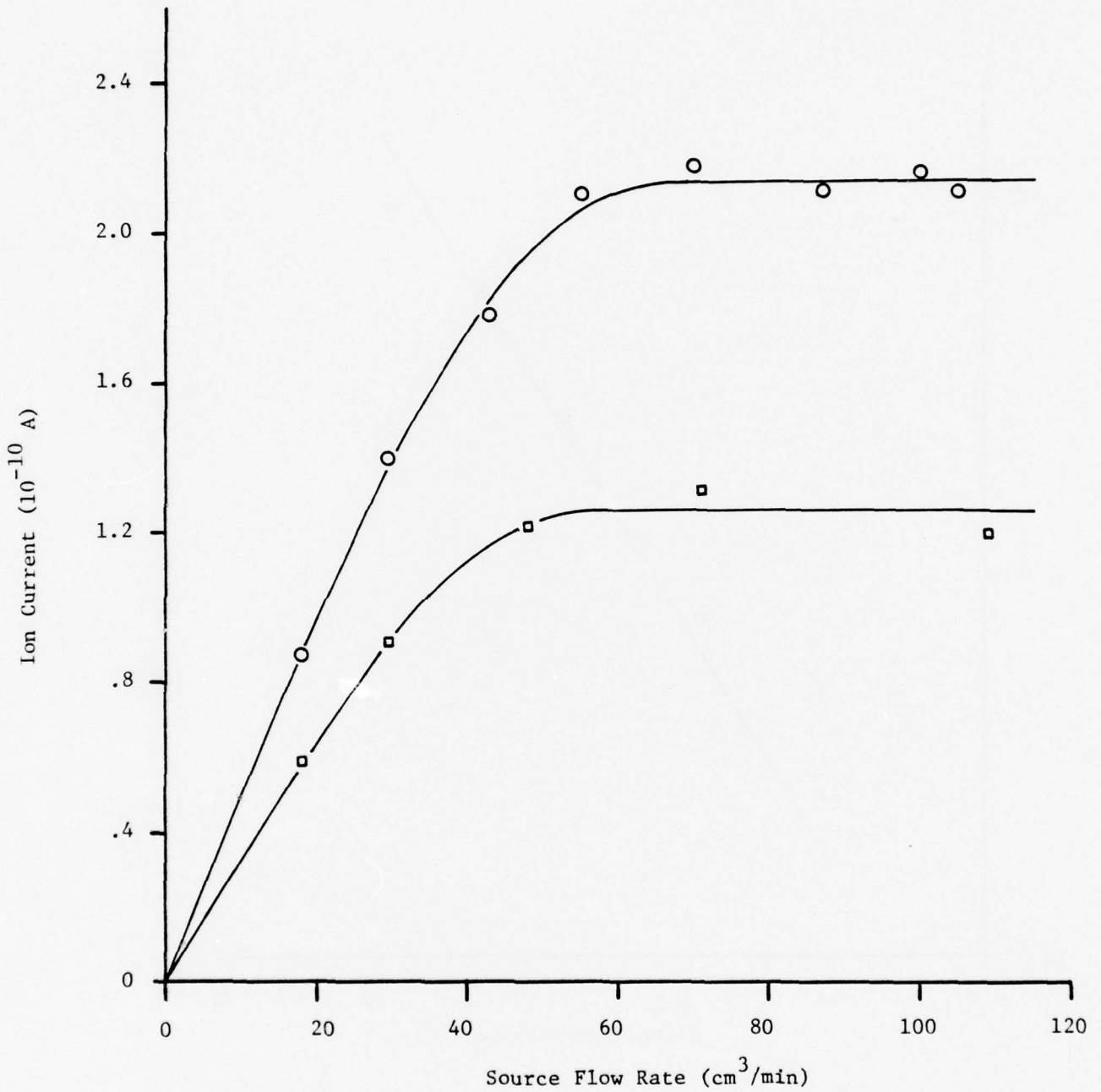source temperature.

147

Figure 6.3. Ion current as a function of source flow rate for a fixed sampling flow rate. Circles, source temperature = 20°C; squares, source temperature = 10°C.

148

or 200°C, the diluted vapor stream came to equilibrium in about 4 minutes, indicating that the walls of the mixing flask equilibrated rapidly with the air stream. The response was equally rapid in returning to the higher initial concentration when the diluting air was reduced to zero.

This responsiveness was used to test the temperature characteristics of the PC. The PC was operated at 140° and 120°C, and the diluting air was cycled on and off in each case. The equilibrium currents were the same as for operation at the higher temperatures, but the time required to reach equilibrium increased rapidly as the operating temperature was lowered. At 140° the equilibrium time was about a half hour, and at 120°C it was much longer than an hour. Based on this, the minimum operating temperature of the PC should be in the range of 150-160°C if real time response is desired.

The vapor source appears to be operating well as designed. Insufficient time was available to check the DNT column, but based on the experience with the TNT column, no difficulties with its use are expected. The usefulness of the vapor source has already suggested itself in some of the measurements already performed. An independent calibration of the vapor saturation would be desirable from the point of determining the effective reaction volume of the PC.

149

7.0 SUMMARY AND RECOMMENDATIONS

In this section we summarize the overall sensitivity of the PC, both measured and projected, and include recommendations for further development of the instrument.

7.1 Summary

The sensitivity of the plasma chromatograph for a given explosive is the product of its ionization efficiency of the molecules, the transmission losses of the grids, and the detectability of the ion. The detectability is a term related to the noise performance of the amplifier, the length of time to be spent in averaging the signal, and the effects of interfering ions.

The ionization efficiencies for TNT and DNT were measured in both air and nitrogen, while the use of the PC as an explosives detector will normally restrict it to air as a carrier gas. The ionization efficiencies for proton abstraction are higher in air, but mainly because the reactant ion concentrations are higher in air than in nitrogen. TNT has an ionization efficiency (ionic) of $6.55 \cdot 10^{-3}$ ions/molecule, or one ion for every 152 molecules present in the reaction region, as long as the number is held constant. DNT has an ionization efficiency of $2.31 \cdot 10^{-2}$ ions per molecule, one ion for every 43 molecules. These are high efficiencies for dry air, and there is a possibility that they could be higher still for air with substantially more water vapor. In any case, the detectability of the ions will set a minimum current for detection; that current will constitute the removal of I/e ions per second from the reaction region, which will have to be replaced by neutral molecules.

150

At equilibrium, the number of ions removed per second will be in proportion to the number of molecules introduced per second, with the constant of proportionality being equal to the ionization efficiency for the flow rate chosen:

$$Is/e = IE(\dot{F})[N]\dot{F} , \tag{7.1}$$

where $[N]$ is the number density of neutral molecules, $\dot{F}$ is the volume flow rate, and the product $IE(\dot{F}) \cdot \dot{F}$ is the ionization rate for the molecules of interest.

The transmission losses of the grids have been taken to be just the calculated ionic transmission losses. This calculation represents the minimum loss that could be expected, and the actual losses could be higher. However, because the ionization efficiency measurements naturally include the transmission losses, any excess loss appears as a reduced ionization efficiency. This means that the sensitivity of the Beta/VII PC has been measured for a specific configuration, and, as long as no changes in the grid configurations are made, the measurements will be valid for other Beta/VII-type instruments.

The detectability of an ion will be discussed in terms of the noise and response time of the signal processing equipment. We will give no consideration to interfering species, although such interferences are an important factor in detection, especially when the detection limits are pushed to extremes.

The noise current and response time of the instrument are inter-related and dependent upon the type of signal processing employed. In the standard configurations, one-grid mode with signal averaging or

151

two-grid mode, the noise currents have been measured. The response time is calculated as the time it would take for a signal change to reach 90 percent of its final value. The minimum response time has been taken arbitrarily as the time to complete one sweep of the mobility spectrum, 25 milliseconds. Although the fast electrometer can respond to much shorter signals, some ions cannot reach the collector in any shorter time. A series of curves representing the effective noise currents as a function of response time for the standard instrument are shown in Figure 7.1. The effective noise currents for the two-grid electrometer and aperture grid noise are for a duty cycle of $8 \cdot 10^{-3}$. The effective noise for these two sources decreases inversely as the duty factor, but no more than a factor of 2.5 could reasonably be expected in standard operation. The aperture grid noise is assumed to be proportional to the square root of the bandwidth, since that was implicit in its derivation; it has only been measured at one bandwidth, though. Averaging, together with signal integration in the one-grid mode, gives an equivalent noise current lower than the two-grid mode of operation at a comparable response time.

Now, we would like to project the noise performance that could be obtained under optimum conditions--for example, an optimum feedback resistor as described in Appendix 1, transversal filtering at the matched condition, integration of the filtered signal, pseudo-random coding with no interferences, charge averaging, and displacement current utilization. The first three of these are quite attainable, while the last three require development and should be considered speculative. Charge averaging shows the most rapid increase as the response time is lengthened, but it suffers the same duty factor limitation as normal two-grid operation. These projections are shown in Figure 7.2.
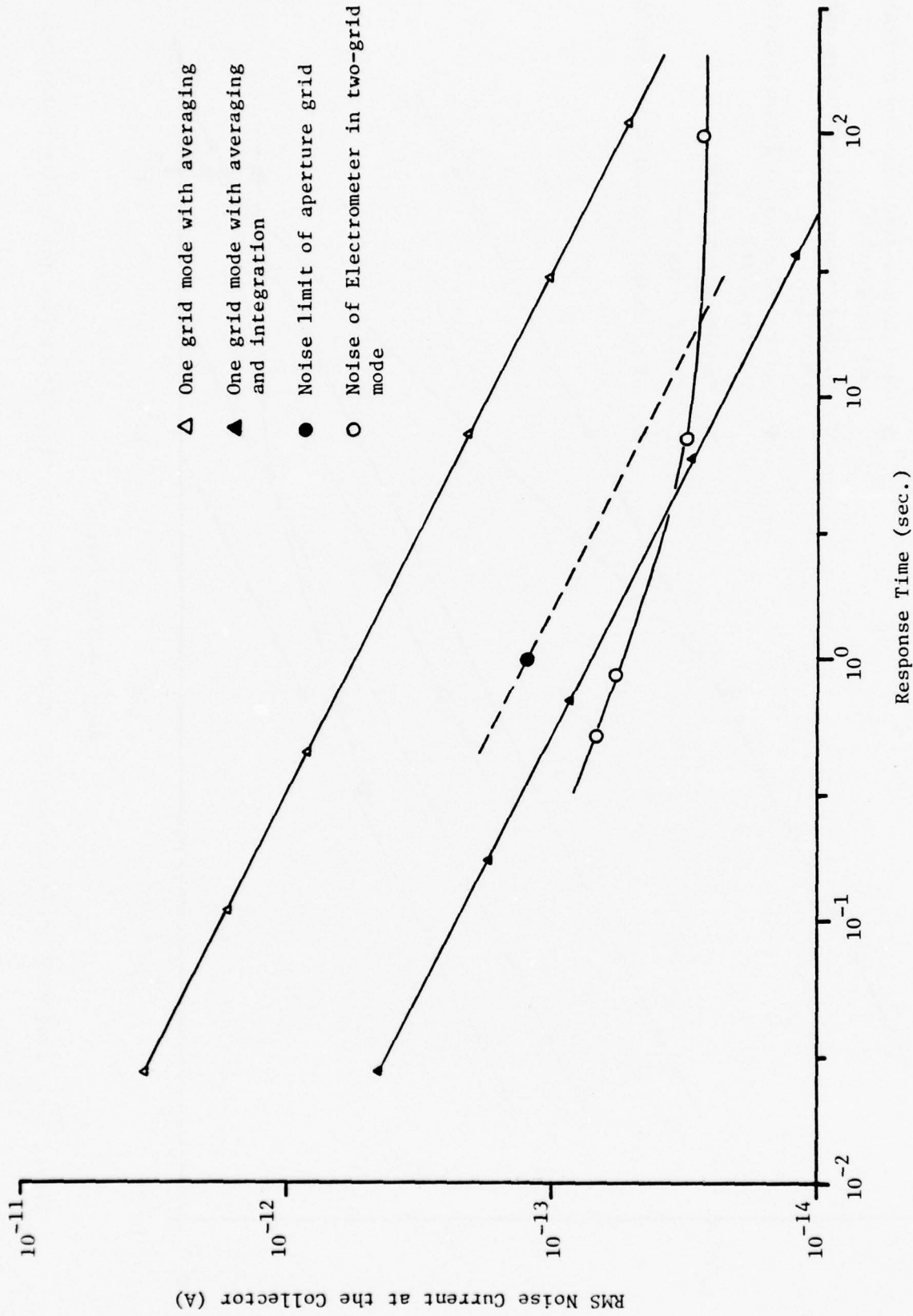
152

Figure 7.1. Effective noise current as a function of response time for the standard electrometer.
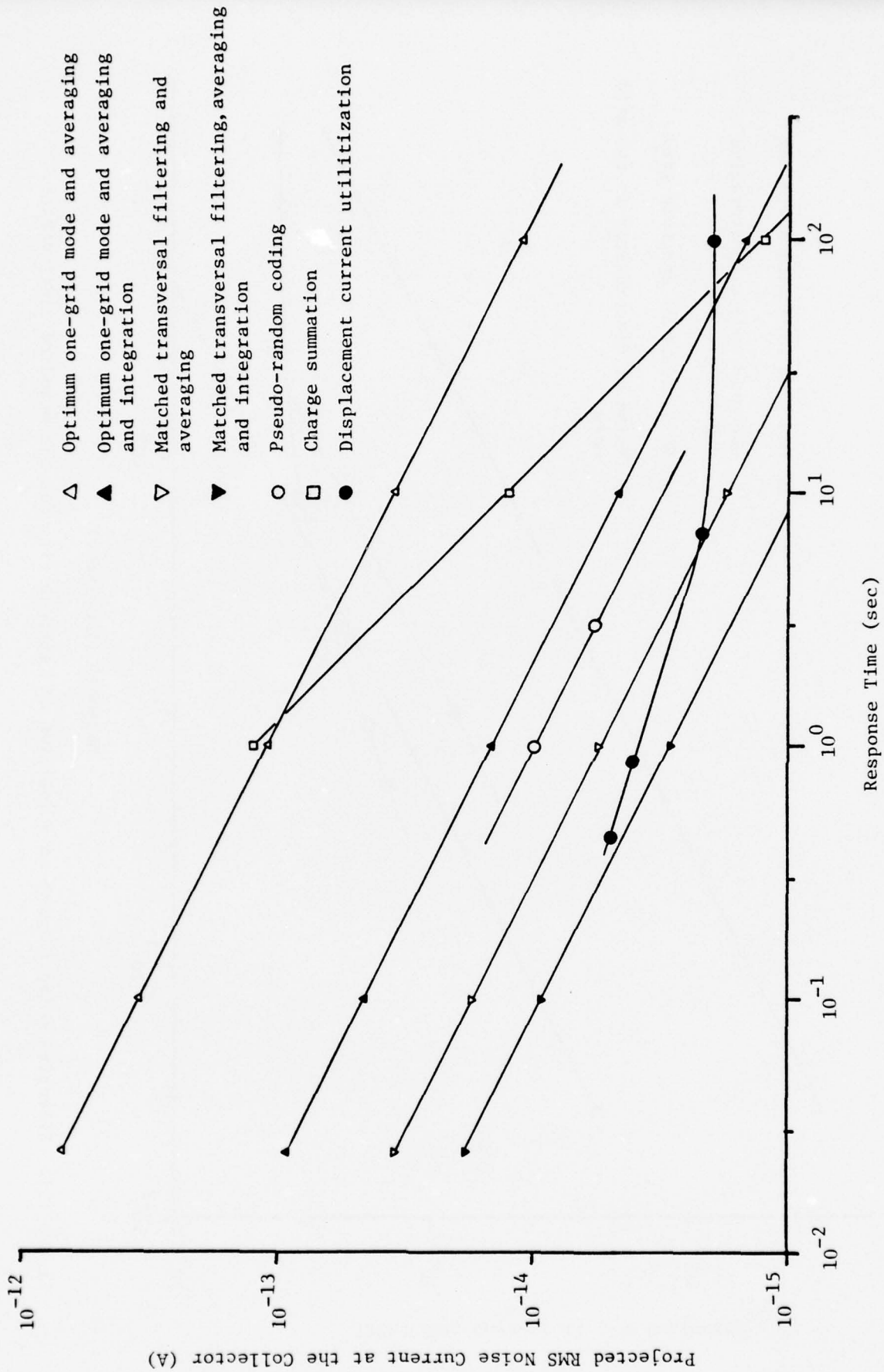
△ One grid mode with averaging

▲ One grid mode with averaging and integration

● Noise limit of aperture grid

○ Noise of Electrometer in two-grid mode

Response Time (sec.)

RMS Noise Current at the Collector (A)

153

Figure 7.2. Projected noise currents as functions of response time for various processing techniques.

Legend:

△ Optimum one-grid mode and averaging
▲ Optimum one-grid mode and averaging and integration
▽ Matched transversal filtering and averaging
▼ Matched transversal filtering, averaging and integration
○ Pseudo-random coding
□ Charge summation
● Displacement current utilitization

Response Time (sec)

Projected RMS Noise Current at the Collector (A)

154

Most of these projected methods are capable of effective noise currents of 10^{-15} A with response times of less than 100 seconds, representing improvements over the best standard instrument response of factors of 30 to 50. Although in some cases a combination of processing methods is used to achieve this performance, the projections are not unrealistic. Improvements in detection sensitivity of factors of 2 may not seem important, but each factor of 2 reduction in noise can be applied to reduce averaging time by a factor of 4, a goal that may be more important than other considerations.

What is the criterion for a minimum signal that can be detected? Chromatographers often use the criterion that the signal amplitude must equal the peak-to-peak noise amplitude. This is a reasonable limit, but may be somewhat high, depending on the method of display. The mobilities of the explosives of interest are known, and so detection depends upon detecting a non-zero response of a particular shape at a particular time. The human eye and brain seem to be quite adept at picking patterns out of random lines so that a less critical criterion might apply.

7.2 Recommendations

The results of this research suggest that the sensitivity of the plasma chromatograph can be pushed to considerably lower limits than were previously available. The techniques for doing so are relatively easily achieved and could be put into practice. However, it is not certain that all the sensitivity of the instrument would be usable, because other weakly-ionized species might contribute substantial interference at these levels.

Measurements of the components of ambient air at mobilities near that of TNT and DNT should be undertaken before attempts are made to push the sensitivity of the PC to its limit. This would insure against running into a detection limit determined external to the PC.

If it proves desirable to try to increase the sensitivity of the PC, or to trade useful sensitivity for decreased response time, then a redesign of the basic plasma chromatograph would be the best approach. It should be aimed at increasing the production rate of ions; for example, higher reactant ion currents could be obtained with a higher activity source and a larger reaction volume; some gases could possibly be added to enhance the proton-abstraction reaction; and the electric field in the reaction region could be optimized. The grid transmission losses should be measured and, if possible, reduced. If one-grid operation is seen to be the most desirable operating mode, the second-grid should be removed. If two-grid operation is seen to be more desirable, the aperature grid should be removed or at least moved away from the collector.

The sensitivity or response of the detection electronics would be immensely aided by a decrease in collector capacitance. This could be obtained by increasing the spacing between the aperture grid and the collector and by reducing the area of the collector. The loss of signal due to a smaller collector area could be compensated by focusing ions on the collector with conical field rings instead of cylindrical rings.

Each of these steps might be expected to double or triple the sensitivity of the PC. Taken together, they could add up to a further

156

substantial increase in sensitivity, or could result in an even more substantial reduction in response time.

The choice of course to follow now depends more on the requirements of the detection problem than it does on the capabilities of the plasma chromatograph itself.

157

APPENDIX 1

Electrometer Noise Analysis

The total noise current referred to the input of an electrometer amplifier is given by

$$i^2 = \hat{i}^2 \, \Delta f_i + \frac{\hat{e}^2}{R^2} \, \Delta f_e \qquad\qquad (A.1.1)$$

where $\hat{i}$ is the total current noise per unit bandwidth, $\hat{e}$ is the total voltage noise per unit bandwidth, and Δf_i and Δf_e are the respective effective bandwidths. For the purpose of this analysis, $\hat{i}$ and $\hat{e}$ are assumed to be independent of frequency. This is an assumption known to be untrue, but in the absence of detailed measurements, average published values will be used. If the detailed dependencies were known, inclusion in the following integrals would be straightforward.

The noise current is the sum of noise sources in the feedback resistor and input bias current.

$$\hat{i}^2 = \hat{i}_R^2 + \hat{i}_B^2 \qquad\qquad (A.1.2)$$

$$\hat{i}_R^2 = \frac{4kT}{R} \qquad\qquad (A.1.3)$$

$$\hat{i}_B^2 = 2e \, i_B \; . \qquad\qquad (A.1.4)$$

The term $\hat{i}_B$ can be calculated from published specifications. For the Burr-Brown 3421K, $\hat{i}_B = 4 \cdot 10^{-14} \; A/\sqrt{H_z}$; for the Burr-Brown 3523L, $\hat{i}_B = 1 \cdot 10^{-16} \; A/\sqrt{H_z}$.

158

The resistor noise term is $1.29 \cdot 10^{-14}$ A/$\sqrt{H_z}$ for a 10^8 ohm resistor, $1.29 \cdot 10^{-15}$ A/$\sqrt{H_z}$ for a 10^{10} ohm resistor, and $4.07 \cdot 10^{-16}$ A/$\sqrt{H_z}$ for a 10^{11} ohm resistor at 300K. From this, it can be seen that amplifier noise for the 3421 dominates the resistor noise for all values of feedback resistance, and that amplifier current noise for the 3523 is dominated by resistor noise for all values of feedback resistance used.

The noise voltage term, $\hat{e}$, is $4 \cdot 10^{-8}$ V/$\sqrt{H_z}$ for the 3421 K and $2 \cdot 10^{-8}$ V/$\sqrt{H_z}$ for the 3523 L.

The bandwidths Δf_i and Δf_e are calculated according to

$$\Delta f = \int_0^\infty |H(f)|^2 \, df \, , \qquad (A.1.5)$$

where $H(f)$ is the transfer function appropriate to the current or voltage noise source. The current noise appears at the inverting terminal of the electrometer amplifier in the same way that the signal current does. The transfer function is therefore the same as the signal current transfer function. This was measured and presented in Figure 5.6 for the wideband circuit with the 10^8 ohm resistor and the compensated circuit with the 10^{11} ohm resistor. The noise bandwidth was calculated numerically to be approximately 44kH$_z$ for either circuit. (Note that $H(f)$ is usually normalized to unity at zero frequency; attenuation by the compensation network does not change the noise referred to the amplifier input.)

Thus,

$$\Delta f_i = 4.4 \cdot 10^4 \, H_z \, .$$

The transfer function for the noise voltage is calculated from the current gain and the compensation network gain:

$$H_e(f) = \frac{A(o)}{A(f)} \cdot C(f) \qquad (A.1.6)$$

159

where $A(f)$ is the current transfer function and $C(f)$ is the compensation function.

If no compensation is used, as for a 10^8 feedback resistor, then $H_e(f)$ is the same as the current transfer function, and Δf_e is $4.4 \cdot 10^4$ H_z.

For the 3421 amplifier,

$$i_T^2 = \left[(4 \cdot 10^{-14})^2 + (1.29 \cdot 10^{-14})^2 + \frac{(4 \cdot 10^{-8})^2}{(10^{-8})^2} \right] 4.4 \cdot 10^4$$

$$= 7.77 \cdot 10^{-23} \text{ A}^2$$

$$i_T = 8.8 \cdot 10^{-12} \text{ A rms}.$$

For the 3523 amplifier,

$$i_T^2 = \left[(1 \cdot 10^{-16})^2 + (1.29 \cdot 10^{-14})^2 + \frac{(2 \cdot 10^{-8})^2}{(10^8)^2} \right] 4.4 \cdot 10^4$$

$$= 7.32 \cdot 10^{-24} \text{ A}^2$$

$$i_T = 2.71 \cdot 10^{-12} \text{ A rms}.$$

The calculated noise is slightly higher than the measured noise for the 3421, and almost a factor of two lower than the measured noise for the 3523. As expected, the bias current noise dominates for the 3421, and resistor noise for the 3523.

For the compensated amplifier, $H_e(f)$ is given by, approximately,

$$H_e(f) = 1 + \left(\frac{f}{f_1} \right)^{1.1} , \tag{A.1.7}$$

where f_1 is equal to $(R_f C_f)^{-1}$ and is approximately 0.32 H_z with the 10^{11} ohm resistor. This transfer function cuts off at some high frequency, but

160

the details of the cut-off affect the noise bandwidth so much that the
upper frequency limit will be chosen to approximate the measured results.
The exponent, 1.1, is a power law approximation to the actual transfer
function.

$$\Delta f_e = \int_o^{1.9 \cdot 10^4} \left[1 + \left(\frac{f}{f_1} \right)^{1.1} \right]^2 df \qquad (A.1.8)$$

$$= 6.25 \cdot 10^{14} \; H_z \; .$$

The magnitude of Δf_e emphasizes the importance of having a high
frequency limit on the noise calculation and on the system itself.

$$i_T^2 = \left[(4 \cdot 10^{-14})^2 + (4.07 \cdot 10^{-16})^2 \right] 4.4 \cdot 10^4 + \left[\frac{(4 \cdot 10^{-8})^2}{(1 \cdot 10^{11})^2} \right] 6.25 \cdot 10^{14}$$

$$= 1.07 \cdot 10^{-22} \; A^2$$

$$i_T = 1.04 \cdot 10^{-11} \; A \; rms$$

and, for the 3523,

$$i_T^2 = \left[(1 \cdot 10^{-16})^2 + (4.07 \cdot 10^{-16})^2 \right] 4.4 \cdot 10^4 + \left[\left(\frac{2 \cdot 10^{-8}}{10^{11}} \right)^2 \right] 6.25 \cdot 10^{14}$$

$$= 2.50 \cdot 10^{-23} \; A^2$$

$$i_T = 5.0 \cdot 10^{-12} \; A \; rms \; .$$

Now, the upper frequency limit of the integral was chosen to give
this last value of noise current. The point of the calculation is to show

161

that the voltage noise dominates the current noise sources because of the compensation given. The calculation also indicates that there is not much difference for either amplifier for compensated or uncompensated operation. However, the compensated amplifier responds to filtering much more favorably than the uncompensated amplifier, because filters remove the worst noise frequencies at the least sacrifice of signal.

These calculations indicate that an intermediate value feedback resistor would perform better than either of the two values used. Choosing a back resistor of 10^{10} ohms, the compensation integral (A.1.8) would need to be modified. The modification is in the value of f_1, which will be increased to 3.2 Hz. Recall that $f_1 = (R_f C_f)^{-1}$. It can be argued that C_f will not depend on the value of feedback resistor since it serves only to stabilize the amplifier against the input capacitance. Therefore, f_1 is proportional to R_f.

Then,

$$\Delta f_e = 3.94 \cdot 10^{11} \text{ Hz}$$

and

$$i_T{}^2 = \left[(1 \cdot 10^{-16})^2 + (1.29 \cdot 10^{-15})^2 \right] 4.4 \cdot 10^4$$

$$+ \left[\left(\frac{2 \cdot 10^{-8}}{10^{10}} \right)^2 \right] 3.94 \cdot 10^{11}$$

$$= 1.65 \cdot 10^{-24} \text{ A}^2$$

$$i_T = 1.28 \cdot 10^{-12} \text{ A rms}.$$

162

This figure is still not optimum, but represents a factor of four improvement. The optimum value would come when the noise voltage contribution equalled the resistor noise contribution.

We again note the importance of the input capacitance. It determines the size of C_f, which determines f_1 for a given value of resistor. If the input capacitance were reduced, then C_f would be reduced, and f_1 would be increased. The overall noise figure would be significantly improved.

163

APPENDIX 2

Operation of Vapor Calibration Source

The operation of the vapor calibration source is divided into the general areas of temperature control and flow control.

Temperature control is concerned with the catalytic burner furnace, the column temperature and the mixing chamber temperature.

The catalytic burner should run at a temperature of 200–250°C. This is obtained by setting the furnace control at its minimum on position. There is a detent for positive setting of this position.

The mixing chamber box and connecting tubing are heated by silicone-rubber heating elements and are controlled together by an SCR power controller. The connecting glassware runs at a temperature somewhat lower than the box, but this ordinarily causes no problems. The controller is not calibrated in either power or temperature, but at a dial reading of 45, the box temperature reaches about 145°C. Based on response time measurements with the PC, this is close to the lowest recommended temperature of 150°C. If no changes of concentration will be needed, so that equilibrium times are not important, lower box temperatures can be used. The maximum temperature for silicone rubber seems to be 200–250°C for prolonged service life. These temperatures would be exceeded if maximum power is applied by the controller.

The column temperature is controlled by a Neslab CC-60II refrigerator. It cycles on and off to maintain the bath temperature at the set point. With the stirrer agitating the bath, operation up to 20°C set point has

164

been obtained; and with the refrigerator on continuously, a temperature below -60°C is obtained.

Denatured ethanol is used as the bath fluid. It remains liquid over the entire operating range, but becomes quite viscous below -50°C. The temperature regulation of the bath depends on the amount of fluid and how vigorously it is stirred. Over most of the temperature range, the regulation obtained was $\pm$0.5°C around the set point at equilibrium, with a fluid level 2 inches above the column. The controller dial is marked with nominal temperatures. A calibration, by means of an iron-constantan thermocouple, is presented in Figure A.2.1. The sensing element is a constant-current-biased diode, and so a linear relationship between the dial potentiometer and the actual temperature has been assumed.

The flow meters have been placed between the cylinder pressure regulator and the flow controller. The flow controllers were chosen to operate with a constant upstream pressure so that changes in the column packing would not affect the flow rate. The flow meters and controllers were calibrated with a bubble flow meter at ambient outlet pressure and 30 PSIG at the pressure regulator. Operation at any other pressure will change the density of gas flowing through the flow meter and will therefore not follow the calibration. The flow meter calibration curves are in Figures A.2.2 and A.2.3.
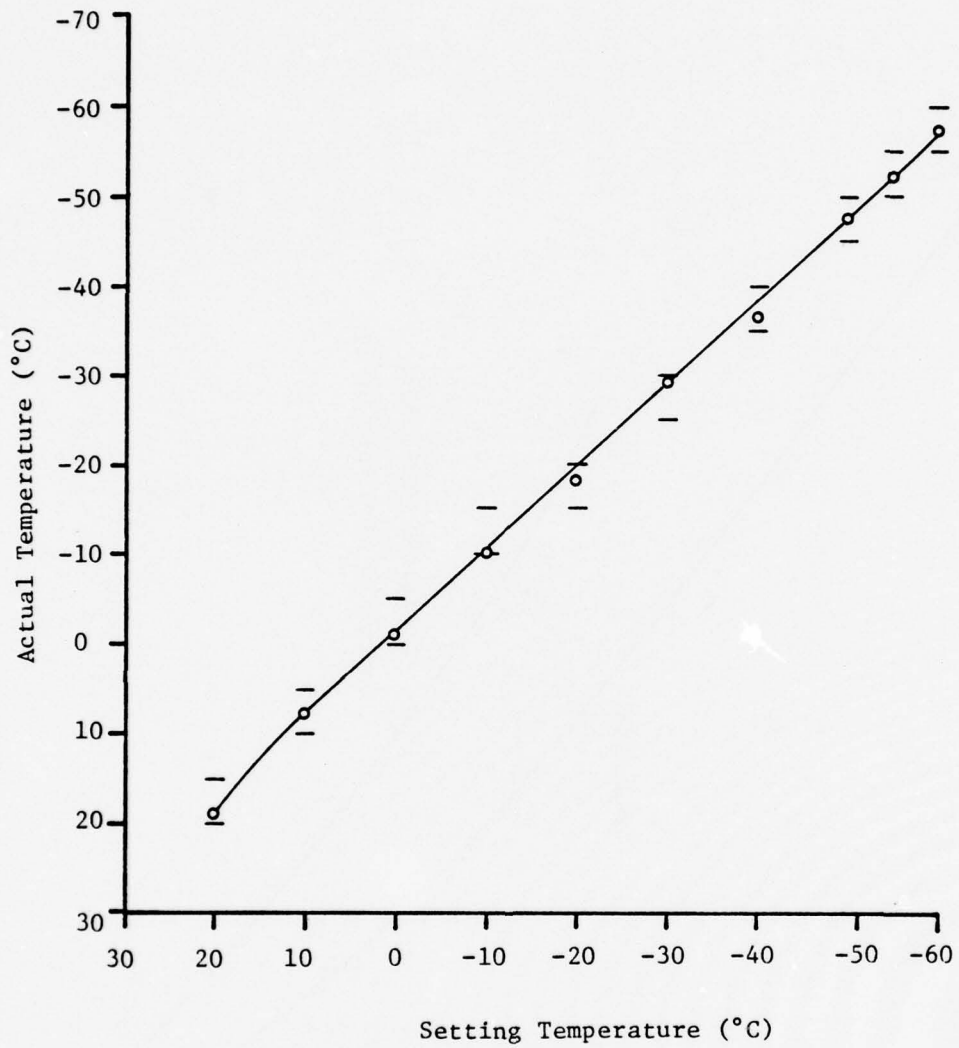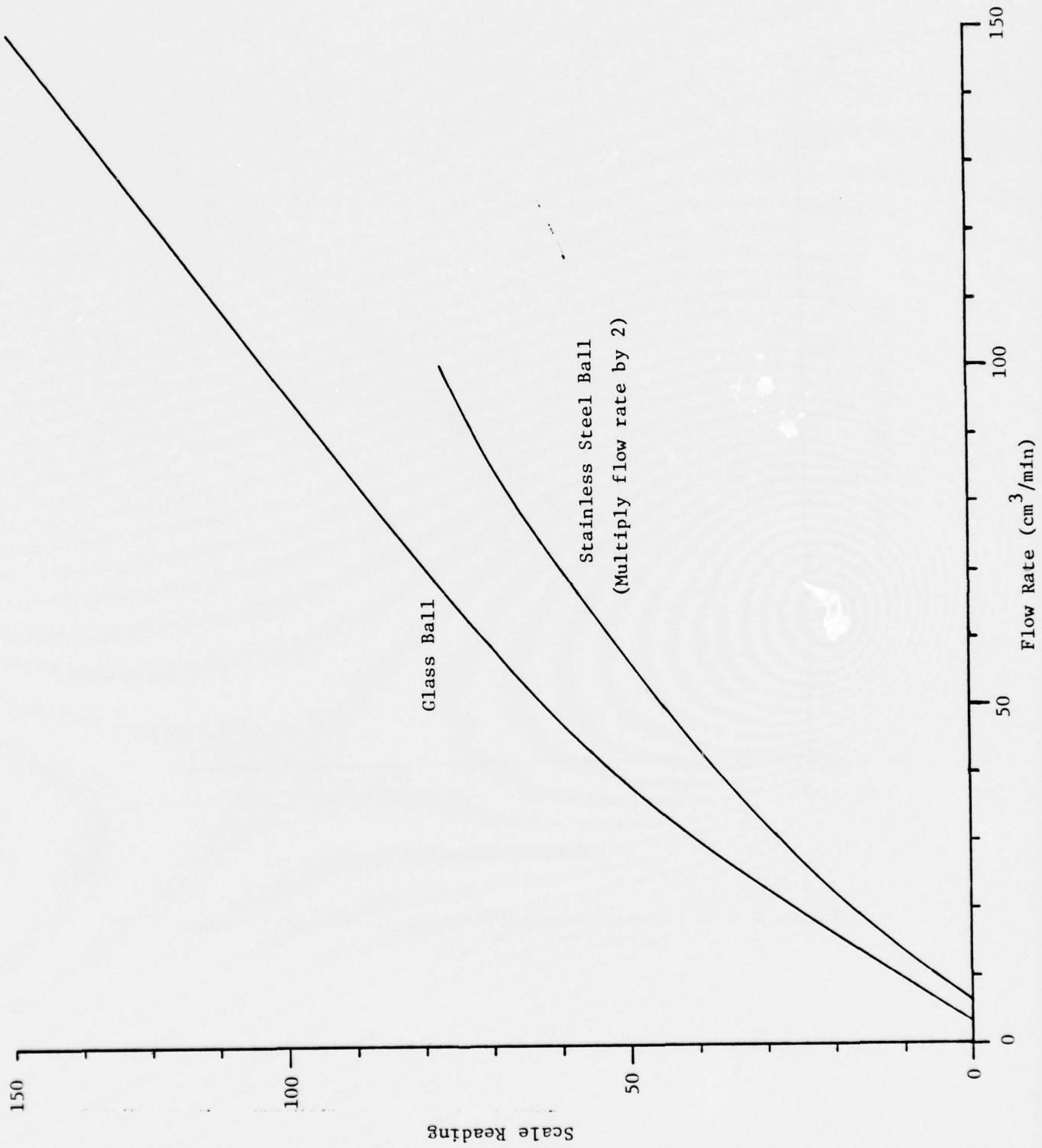
Figure A.2.1.   Temperature calibration of the refrigerator control.

Glass Ball

Stainless Steel Ball
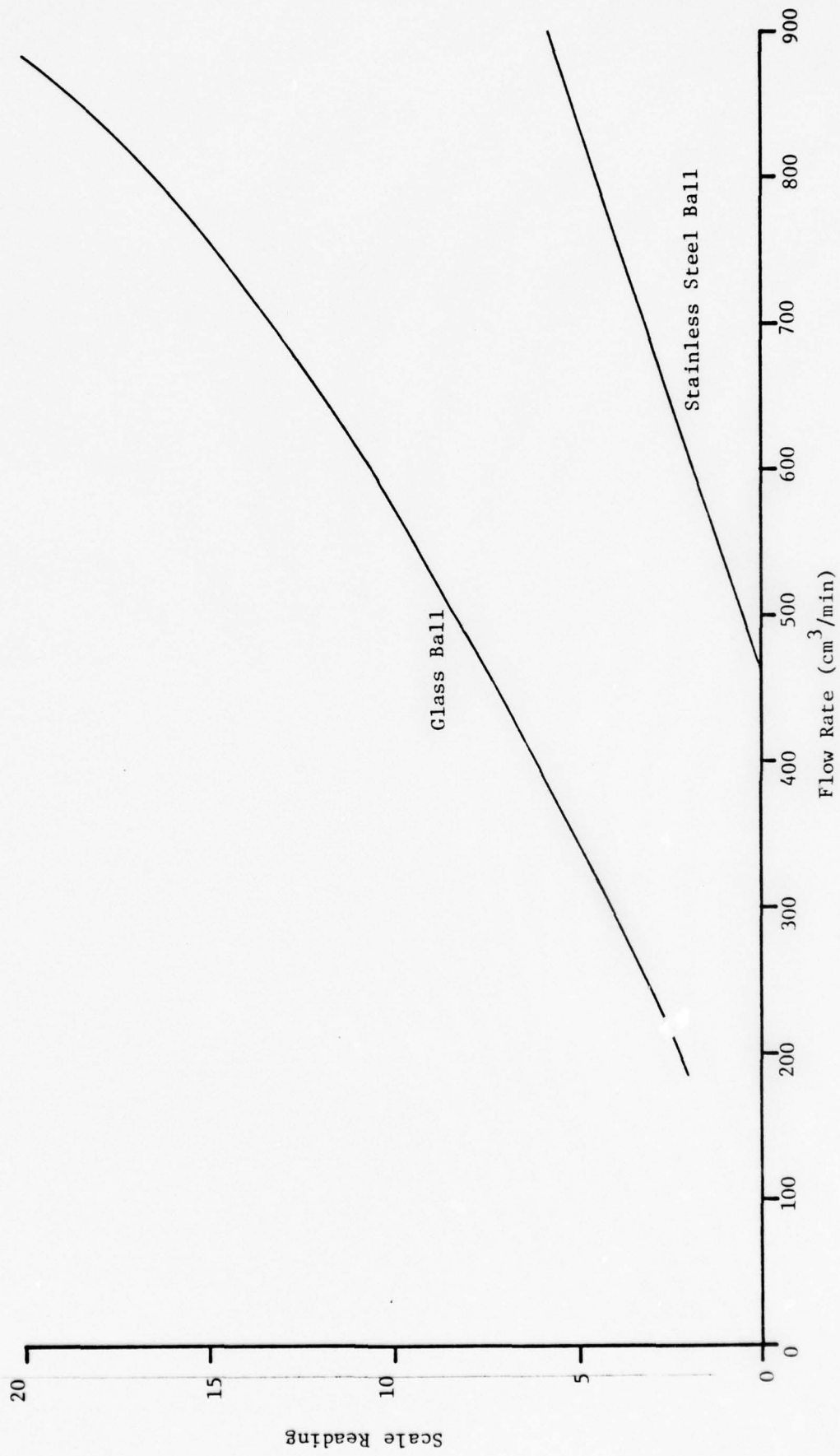(Multiply flow rate by 2)

Flow Rate (cm³/min)

Scale Reading

167

Figure A.2.3. Dilution Flowmeter Calibration.

168

APPENDIX 3

Circuit Schematics

This appendix contains the circuit schematics for the automatic baseline correction circuit and for modifications that were made in various sections of the PC.

Original schematic diagrams of the Beta/VII plasma chromatograph are taken from the operating and maintenance manual and have been reproduced without written permission.
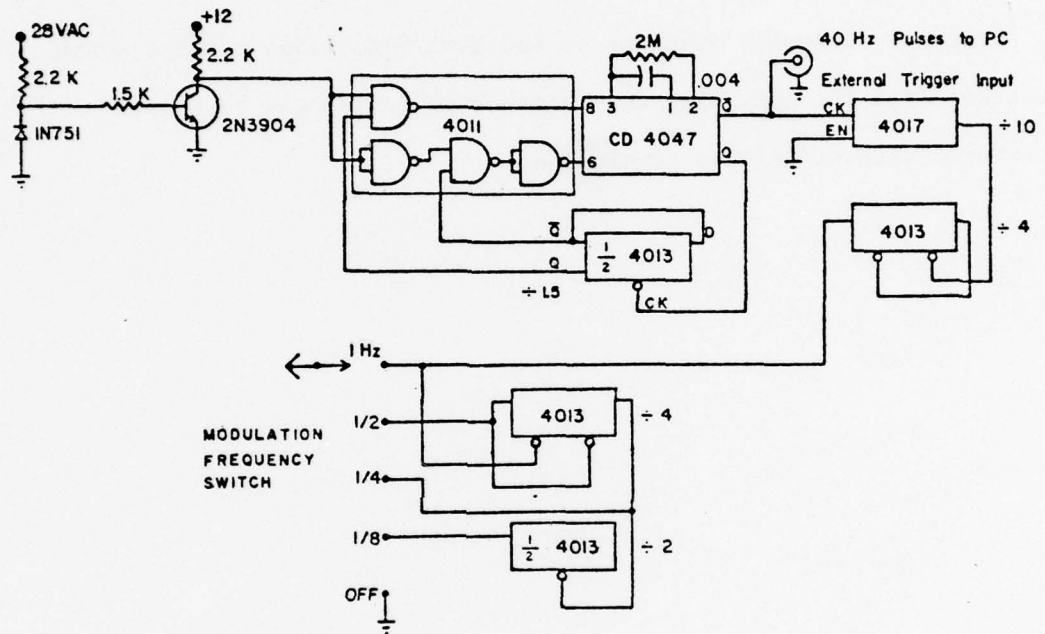
Figure A.3.1. Automatic Baseline Correction Circuit: Clock and Timing.

170
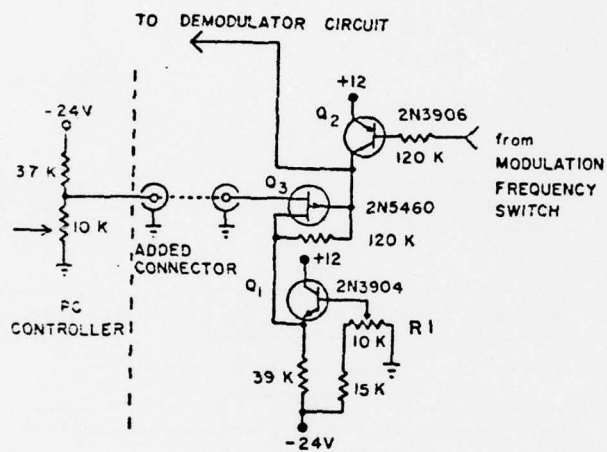
Figure A.3.2. Automatic Baseline Correction Circuit: Modulation.
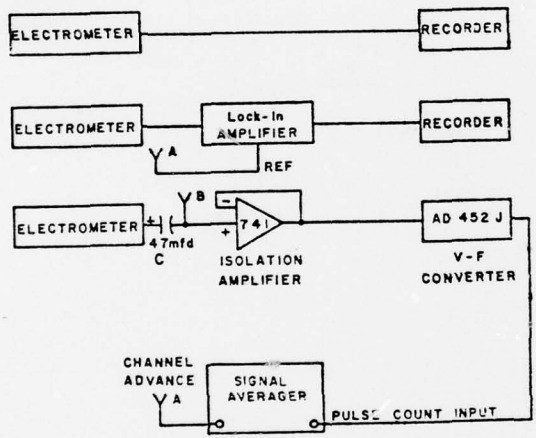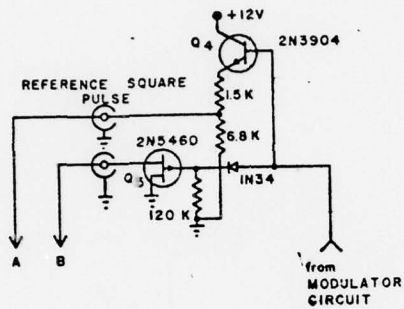
Figure A.3.3. Automatic Baseline Correction Circuit: Demodulation.

172

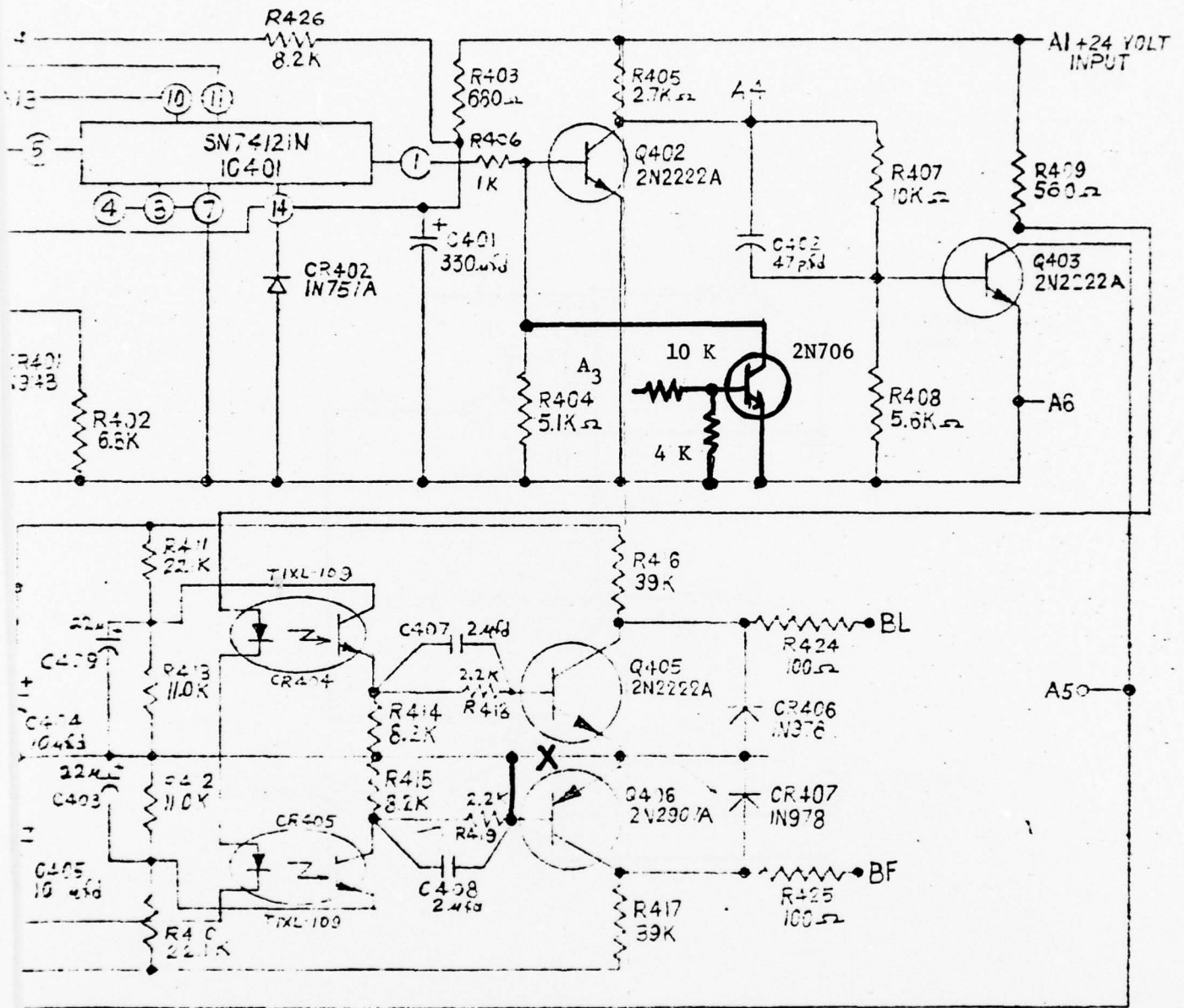Figure A.3.4. Wiring Modifications to PC Controller.

Figure A.3.5. Wiring Modifications to PC Controller.

174

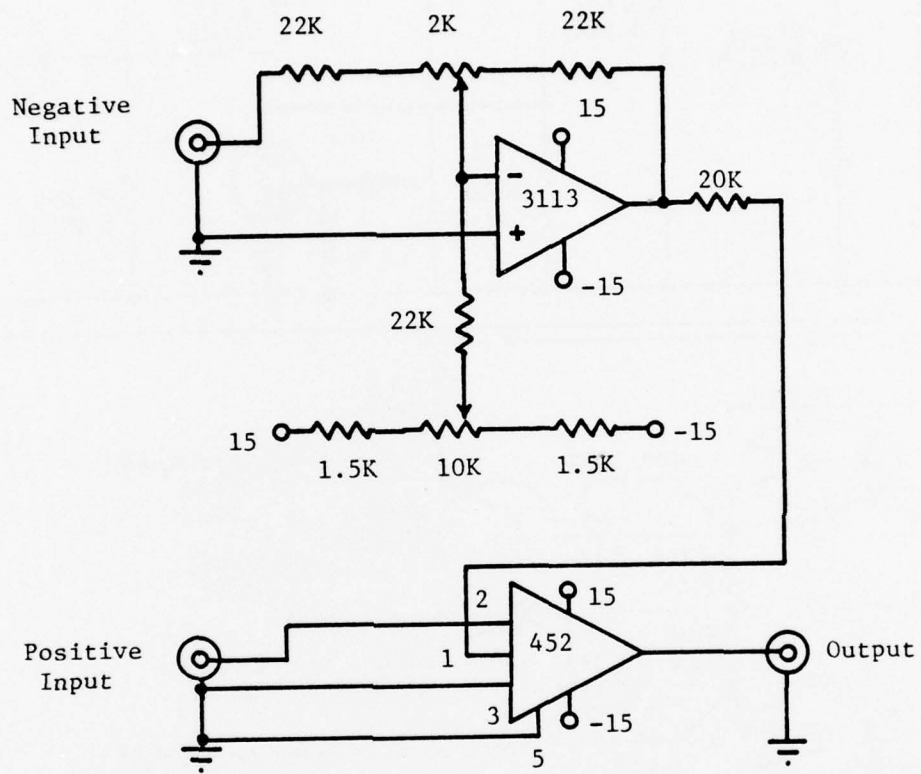Figure A.3.6. Added components for control of Grid One, and wiring modification after failure of CR405.

Figure A.3.7. Voltage-to-frequency Converter.

APPENDIX 4

Calculation of Ionic Transmissivity

The optical transmissivity of a grid of fine wires is equal to the projected area of the wires divided by the total area of the grid. For wires of radius R and spacing L (center to center), the transmissivity is:

$$T_o = 1 - \frac{2R}{L} . \tag{A.4.1}$$

The ionic transmissivity differs from the optical transmissivity because ions follow electric field lines, not light rays, and the wire distorts a previously uniform electric field. This is a classical problem in electrostatics.

The potential of a region around a grounded wire in a previously uniform electric field is given by

$$V(r,\phi) = E_\infty (1 - (\frac{R}{r})^2)r \cos \phi \tag{A.4.2}$$

where E_∞ is the value of the electric field far from the disturbing wire and r and ϕ are the radial coordinates of a point shown in Figure A.4.1.

The gradient of the potential gives the electric field at any point. The gradient operator for this two dimensional geometry is

$$\vec{\nabla} = \hat{r}[\frac{\sin 2\phi}{r} \frac{\partial}{\partial \phi} + \frac{\partial}{\partial r}] + \hat{\phi}[- \frac{\cos \partial \phi}{r} \frac{\partial}{\partial \phi}] \tag{A.4.3}$$
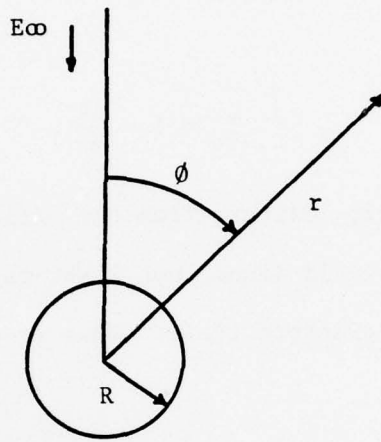
177

Figure A.4.1. Coordinates for wire transmission.

Application of this operator to the potential gives

$$E_r = E_\infty [(1 + \frac{R^2}{r^2}) \cos \phi - (1 - \frac{R^2}{r^2}) \sin \phi \sin 2\phi] \qquad (A.4.4)$$

and

$$E_\phi = E_\infty [(1 - \frac{R^2}{r^2}) \sin \phi \cos 2\phi]. \qquad (A.4.5)$$

The ϕ-component vanishes at the surface of the wire $(r = R)$ as it should.

Now, we calculate the flux on the surface of the wire, and assume that the flux of ions onto the wire is in proportion to the electric flux. We are interested in only the upper hemisphere, since all the ions come from that direction; and since there is only a normal electric field component at the surface, the flux integral is simple:

$$Flux = \int_{-\pi}^{\pi} 2E_\infty \cos \phi \, Rd\phi$$

$$= 4RE_\infty \qquad (A.4.6)$$

This flux is for a unit length of wire in three dimensions. The equivalent flux, evaluated far from the disturbing wire, is just a line integral along a path normal to the electric field:

$$Flux = 4RE_\infty = \int_{-x}^{x} E_\infty dx$$

$$= 2xE_\infty . \qquad (A.4.7)$$

179

Or,

$$x = 2R \; , \qquad\qquad\qquad (A.4.8)$$

which implies that, as far as the ions are concerned, the wire has an
effective diameter equal to twice its physical diameter. Therefore,
the ionic transmissivity of a wire grid is given by

$$T_i = 1 - \frac{4R}{L} \; . \qquad\qquad\qquad (A.4.9)$$

The PC gating grids have a value of $\frac{2R}{L} = 8 \times 10^{-2}$, so the ionic
transmissivity is 0.84 for each grid. The aperture grid consists of a
foil with square holes etched in it. An optical transmission of 0.80
implies that $\frac{2R}{L} = 0.106$. Then the ionic transmissivity would be 0.622,
assuming that the "wires" have circular cross-section and that corner
effects are negligible. Both of these assumptions are probably wrong,
but would tend to cancel each other. That is, a deviation from circular
cross-section would increase the ionic transmissivity and corner effects
would decrease the transmissivity.

The total transmissivity is the product of the factors for each
grid. Thus, the total optical transmissivity is

$$T_o = (.92)(.92)(.80) = .677 \; ,$$

and the total ionic transmissivity is

$$T_i = (.84)(.84)(.622) = .439 \; .$$

180

APPENDIX 5

Calculation of Displacement Current

The aperture grid in front of the collector plate serves the
function of shielding the collector from the switching transients of
the second grid and from the displacement current of the ions. The
displacement current is the current due to the motion of the ions toward
the collector before they actually reach it. A theoretical calculation
shows that this displacement current can be used to increase the effective
duty cycle of the two-grid mode without a loss of resolution, thus
lowering the effective noise in the ratio of the duty cycle increase.

The displacement current is given by

$$i_d = \varepsilon_o \frac{\partial \phi}{\partial t} , \qquad (A.5.1)$$

where ϕ is the electric flux and ε_o is the permittivity of vacuum. Now
consider an ion bunch admitted to the collector region by the second
grid, having a total charge q and a drift velocity v. We will consider
it as a point charge for the calculation and locate it on the symmetry
axis of the drift tube. The aperture grid will be assumed to be absent.
The coordinates to be used in the calculation are shown in Figure A.5.1.
The spacing from the collector to the second grid is 2 cm, and the
radius, R, of the collector will be taken as 2 cm also. An image charge
will be used to maintain the potential of the collector at zero.

The electrix flux through any area element $d\bar{A}$ is equal to $\bar{E} \cdot d\bar{A}$.
Specifically, the flux through the annular ring in Figure A.5.1 is

$$\phi(x,r) = \frac{2q}{4\pi\varepsilon_o(x^2 + r^2)} 2\pi r dv \cos \theta , \qquad (A.5.2)$$

and
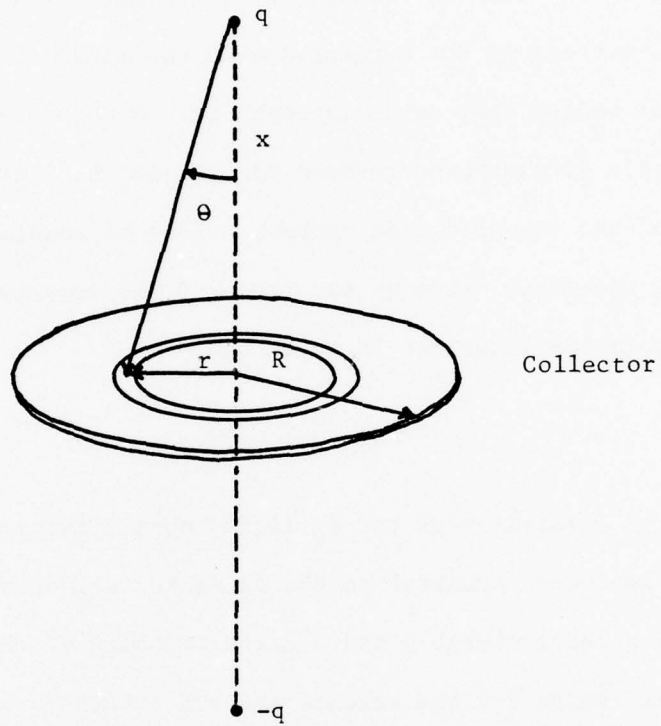$$\cos \theta = \frac{x}{(x^2 + r^2)^{1/2}} . \qquad (A.5.3)$$

181

Figure A.5.1. Coordinates for displacement current calculation.

The total flux is given by

$$\phi(x) = \int_0^R \frac{2q}{4\pi\varepsilon_o} \frac{2\pi r x dr}{(x^2 + r^2)^{1/2}} \qquad (A.5.4)$$

which has the solution

$$\phi(x) = \frac{q}{\varepsilon_o} [1 - \frac{x}{(x^2 + R^2)^{1/2}}] . \qquad (A.5.5)$$

Then

$$i_d = \varepsilon_o \frac{\partial\phi}{\partial t} = - q \frac{\partial}{\partial t} (\frac{x}{(x^2 + R^2)^{1/2}}) . \qquad (A.5.6)$$

$$i_d = -q [\frac{\dot{x}}{(x^2 + R^2)^{1/2}} - \frac{\dot{x}\, x^2}{(x^2 + R^2)^{3/2}}]$$

$$= -q [\frac{\dot{x}}{(x^2 + R^2)^{1/2}} [1 - \frac{x^2}{x^2 + R^2}] \qquad (A.5.7)$$

where

$$\dot{x} = \frac{\partial x}{\partial t} = v ,$$

which is constant.

The fact that the displacement current is just equal to the real current when $x = 0$ gives us the identification

$$i_c = i_d(0) = \frac{q\dot{x}}{R} , \qquad (A.5.8)$$

where i_c is the current normally measured by the electrometer. And so,

$$i_d = i_c \frac{R}{(R^2 + x^2)^{1/2}} [1 - \frac{x^2}{x^2 + R^2}] . \qquad (A.5.9)$$

183

As x varies from 0 to R, i_d varies from i_c to 0.35 i_c, independent of the size of R. The length of time the collector "sees" the displacement current is

$$T = R/v . \qquad (A.5.10)$$

The total "charge" collected over that length of time is

$$q_d = \int_0^T i_d(t)dt$$

$$= \int_0^R i_d(x)dx . \qquad (A.5.11)$$

This integration gives

$$q_d = \frac{i_c R}{\sqrt{2}} . \qquad (A.5.12)$$

The average displacement current over the interval T is

$$i_d = \frac{v}{R} \cdot \frac{i_c R}{\sqrt{2}}$$

$$= \frac{i_c}{\sqrt{2}} . \qquad (A.5.13)$$

The average displacement current over the repetition period of the controller is given by

$$\bar{i} = \overline{id} \cdot \frac{T}{T_{rep}}$$

$$= \frac{i_c}{\sqrt{2}} \frac{R/v}{T_{rep}} . \qquad (A.5.14)$$

184

This translates into an effective duty cycle of

$$DF_d = \frac{R}{\sqrt{2} \, vT_{rep}}$$ (A.5.15)

which compares with the standard duty factor, related to the first grid, of

$$DF = \frac{T_1}{T_{rep}} \, .$$ (A.5.16)

Assuming that $R = 2$ cm, $v = 500$ cm/sec, and $T_1 = 200$ microseconds, the improvement due to using the displacement current is 14 times. The improvement would be greater for a slower moving ion and less for a faster moving one. This factor translates directly into improved sensitivity in the two-grid mode of operation. The displacement current duty factor (from Equation A.5.15) is 0.11. This could be raised further by increasing the radius of the collector and the distance from the second grid to the collector.

A speculation is that, with the aperture grid removed, the electrometer would be limited only by its intrinsic noise current, and so there would be a further increase in sensitivity.

Further speculation says that by using a reduced electric field between the second grid and the collector, the drift velocity in equation A.5.15 could be made much smaller, leading to still further improvement in the duty factor.

185

References

1. D. I. Carroll, I. Dzidic, R. N. Stillwell, and E. C. Horning, Analytical Chemistry $\underline{47}$, 1956 (1975).

2. Glenn E. Spangler and Charles I. Collins, Analytical Chemistry $\underline{47}$, 393 (1975).

3. N. E. Bradbury and R. A. Nielsen, Physical Review $\underline{49}$, 388 (1936).

4. Glenn E. Spangler and Charles I. Collins, Analytical Chemistry $\underline{47}$, 403 (1975).

5. J. W. Lovelock, "Gas Chromatograph," R.P.W. Scott, ed., Buttersworth, Inc. (Washington, D.C., 1960).

6. A. Fontijn, A. J. Sabadell, and R. Ronco, Analytical Chemistry $\underline{42}$, 575 (1970).

7. J. J. Ritter and N. K. Adams, Analytical Chemistry $\underline{48}$, 612 (1976).

8. J. M. Sedlak ad K. F. Blurton, Analytical Chemistry $\underline{48}$, 2020 (1976).

9. E. W. McDaniel, "Collision Phenomena in Ionized Gases," John Wiley and Sons, Inc. (New York, 1964).

10. W. E. Wentworth, E. Chen, and J. E. Lovelock, J. Phys. Chemistry $\underline{70}$, 445 (1966).

11. R. N. Compton, L. G. Christophorou, and R. H. Huebner, Physics Letters $\underline{23}$, 656 (1966).

12. L. G. Christophorou, R. N. Compton, G. S. Hurst, and P. W. Reinhardt, Journal of Chemical Physics $\underline{45}$, 536 (1966).

13. P. A. Lawless and G. E. Spangler, Review of Scientific Instruments $\underline{48}$, 240 (1977).

14. P. G. Cath and A. M. Peabody, Analytical Chemistry $\underline{43}$, 91A (1971).

15. R. S. Neiswauder and Gordon S. Plews, Applied Optics $\underline{14}$, 2720 (1975).

16. W. D. Squire, H. J. Whitehouse, and J. M. Alsup, IEEE Transactions on Microwave Theory and Techniques, $\underline{MTT-17}$, No. 11, 1020 (1969).

17. Reticon Application Notes: 105, Reticon Corporation, 910 Benicia Avenue, Sunnyvale, CA.

18. Reticon Application Notes: 111, Reticon Corporation, 910 Benicia Avenue, Sunnyvale, CA.

19. A. denHarder and L. deGalan, Analytical Chemistry $\underline{46}$, 1464 (1974).

20. A. Savitsky and M. J. E. Golay, Analytical Chemistry $\underline{36}$, 1627 (1964).

21. J. Steiner, Y. Termonia, and J. Deltour, Analytical Chemistry $\underline{44}$, 1906 (1972).

22. Peter A. Pella, Analytical Chemistry $\underline{48}$, 1632 (1976).

23. Philip M. Morse, "Thermal Physics," pp. 222-228, (Benjamin, New York, 1964).